

Investigation of Biopolymer - Mineral Interactions in the Natural Composite Material Nacre

Vom Fachbereich für Physik und Elektrotechnik
der Universität Bremen

zur Erlangung des akademischen Grades eines
Doktor der Naturwissenschaften (Dr. rer. nat.)
genehmigte Dissertation

von Dipl. Phys. Fabian David Heinemann
aus Lohfelden / Kassel

1. Gutachterin: Prof. Dr. Monika Fritz
2. Gutachter: Prof. Dr. Dr. h.c. Horst A. Diehl

Eingereicht am: 24.11.2008

Tag des Promotionskolloquiums: 19.12.2008

Contents

1. Summary	5
2. Introduction	7
2.1. Motivation	7
2.2. Abalone Nacre	8
2.2.1. Shell Growth	12
2.2.2. Nacre Growth	13
2.3. Targets of the Thesis	18
2.3.1. Crystallization Templated by the Interlamellar Matrix	18
2.3.2. Determining the Surface Free Energy of the Interlamellar Matrix	18
2.3.3. Influence of the Soluble Matrix on Precipitation Rates	18
2.3.4. Amino Acid Analysis	19
3. Material and Methods	21
3.1. Organic Material Extraction from Nacre	22
3.1.1. Nacre Preparation from Abalone Shells	22
3.1.2. Preparation of the Interlamellar Organic Matrix	22
3.1.3. Deproteination of the Interlamellar Organic Matrix	22
3.1.4. Preparation of the Water Soluble Organic Matrix	23
3.2. Chemical Methods	24
3.2.1. Protein Concentration Determination (Bradford Assay)	24
3.2.2. Creation of Polymer Foils	25
3.3. Characterization Methods for Crystallization Products	26
3.3.1. X-Ray Diffraction	26
3.3.2. Scanning Electron Microscopy	27
3.3.3. Aragonite Sensitive Staining (Feigl Test)	28
3.4. Double-Diffusion Crystallization Experiments	29
3.4.1. Introduction	29
3.4.2. Experimental Procedure	29
3.5. Contact Angle Measurements	31
3.5.1. Introduction	31
3.5.2. Theoretical Background	31

3.5.3. Experimental Procedure	35
3.6. CaCO ₃ Precipitation Assay	37
3.6.1. Introduction	37
3.6.2. Experimental Procedure	37
3.7. Amino Acid Analysis	39
3.7.1. Introduction	39
3.7.2. Theoretical and Methodical Background	39
3.7.3. Experimental Procedures	43
4. Results and Discussion	47
4.1. Double-Diffusion Crystallization under Constant Conditions	48
4.1.1. Introduction	48
4.1.2. Ammonium-Carbonate Method	48
4.1.3. Conventional Double-Diffusion	49
4.1.4. Development of a Crystallization Device for Controlled Crystallization on a Polymeric Surface	50
4.1.5. Results and Discussion	52
4.2. Surface Free Energy Determination	60
4.2.1. Introduction	60
4.2.2. Results and Discussion	60
4.2.3. Hypothesis of Flat Crystal Growth in Nacre due to Surface Free En- ergy Properties	63
4.3. CaCO ₃ Precipitation Assay	65
4.3.1. Introduction	65
4.3.2. Development of a Calculation Method for CaCO ₃ Precipitation Rates	65
4.3.3. Results	67
4.3.4. Discussion	70
4.4. Amino Acid Analysis	74
4.4.1. Introduction	74
4.4.2. Establishment and Calibration of the Method	74
4.4.3. Validation of the Procedure Using Known Proteins	76
4.4.4. Soluble Organic Matrix of Nacre	78
5. Conclusion and Perspectives	84
Bibliography	87
A. Appendix	96
A.1. Determination of the Organic Fraction	97
A.2. Work for Heterogeneous and Homogeneous Nucleation	99
A.3. Double-Diffusion Box	101

A.4. Self-Made Turbidity Sensor	106
A.5. Bradford Assay Calibration	107
A.6. Abbreviations	108
A.7. List of Manufacturers	109
A.7.1. Equipment	109
A.7.2. Chemicals and Consumables	109
A.8. Own publications	110
A.9. Acknowledgements / Danksagungen	111

1

Summary

The iridescent and highly fracture resistant natural composite material nacre consists of platelets of aragonite (a CaCO_3 polymorph), arranged in a highly regular manner. An organic matrix of less than 5% in weight is intercalated between the mineral platelets, which is necessary for the self-organized growth and the mechanical properties of nacre. In this thesis, aspects of the self-organized growth as well as properties of the organic matrix obtained from nacre of the marine gastropod *Haliotis laevigata* (greenlip abalone) were investigated.

The influence of the interlamellar matrix (the water insoluble matrix component) on CaCO_3 crystal nucleation and growth was investigated. A double diffusion device with constant renewal of the solutions was developed, suitable for the crystallization under constant conditions. By crystallization on the interlamellar matrix and investigation with scanning electron microscopy and X-ray diffraction, it was possible to show that the interlamellar matrix of nacre nucleates flat aragonite crystals with a morphology strongly resembling the aragonite crystals in nacre. In control experiments on several polymer foils, only the usual crystal morphologies and no selectivity for the polymorph aragonite was observed.

For a more detailed characterization of the interlamellar matrix, the surface free energy was determined using contact angle measurements with the sessile drop method. The semi-empirical evaluation method of Owens and Wendt was used, allowing the determination of surface free energy components arising from dispersive and polar interactions. The surface free energy of the interlamellar matrix is mainly of non-polar origin. It could be shown by protein digestion that proteins on the surface of the interlamellar matrix are responsible for this behavior. In addition, a hypothesis was developed, that the unusual crystallization of

flat aragonite crystals is a result of suitable surface free energy properties of the interlamellar matrix, favoring nucleation and wetting by aragonite.

Since also the soluble matrix is required for nacre growth, the influence of soluble matrix proteins on CaCO_3 precipitation rates was determined. A simple precipitation assay was used as a basis and extended. The pH-value course and initial conditions were used to calculate the rate of CaCO_3 crystallization. The soluble proteins from nacre showed a high influence on CaCO_3 precipitation rates compared to the proteins bovine serum albumin and lysozyme. At concentrations of more than $1.0 \mu\text{g}/\text{ml}$, the soluble matrix proteins were strong crystal growth inhibitors, whereas at low concentrations around $0.04 \mu\text{g}/\text{ml}$, crystallization enhancement of a factor of 1.5 was observed.

The soluble matrix was further characterized by performing an amino acid analysis of the soluble matrix proteins. After demineralization and $0.22 \mu\text{m}$ filtration, the matrix was analyzed either as-is or purified by cation-exchange purification, C18 - ZipTip binding or ultracentrifugation. Amino acid analysis was performed by high performance liquid chromatographic separation of phenylthiocarbamyl amino acids of the hydrolyzed samples. Without purification, the amount of non-protein matter was too high for amino acid analysis. The amino acid composition was strongly dependent on the method of matrix protein purification. In general, proline, glycine, leucine and alanine were the most dominant amino acids. A pronounced content of aspartic acid was found only after C18 - ZipTip purification. Indicators for a collagen-like component were found: high proline and glycine contents, as well as the possible detection of hydroxyproline.

2

Introduction

2.1. Motivation

In the living world, a wide variety of organisms is capable of utilizing the deposition of minerals. This ability developed very early in the history of life and subsequently evolved, beginning with the simple *biologically induced biomineralization*, the precipitation of minerals, indistinguishable from geological precipitates [Lowenstam, 1981], to the *biologically controlled biomineralization* [Mann, 1983], the formation of complex and highly specialized composite materials like bone, enamel or nacre.

Probably the oldest fossil records of life - dating back more than 3.5 billion years [Allwood et al., 2007] - are stromatolites, chalkstone structures in the sea, covered by microorganisms. The formation of these structures is induced by the microorganisms, which initiate calcium carbonate precipitation from the seawater.

However, the much more complex materials created by biologically controlled biomineralization require a very high degree of control over crystal nucleation and growth. So far, the formation processes of all complex biominerals are only poorly understood.

Several properties of nacre make it an especially valuable object of research in the field of biomineralization. Since it has a highly ordered and comparatively simple structure with only two hierarchical levels, it may serve as a model system for biomineralization. Principles that explain the processes of nacre formation may turn out to be general principles of biomineralization. A deeper knowledge of calcium carbonate biomineralization is also important in the context of the increasing CO₂ content of the atmosphere. Higher CO₂

levels lower the pH-value of the oceans, possibly affecting the ability of calcifying organisms to form calcium carbonate, which is an important contribution to the global carbon cycle [van Cappellen, 2003].

Nacre is also very interesting from an engineer's point of view. It has an extraordinarily high fracture resistance, consists of environmentally friendly components and has a very beautiful appearance. But even more important is its self-organized manner of growth, which seems to require only a specialized organic matrix soaked with a slightly supersaturated solution, a feat far beyond anything possible with today's technology. An understanding of how nacre forms could provide inspiration for the creation of new types of engineering materials, formed at ambient conditions.

In this work, the nacre obtained from shells of the marine snail *Haliotis laevis* (greenlip abalone) was used, since these shells are quite large with a well developed nacreous layer, as shown in figure 2.1.



Figure 2.1.: Nacreous inner (left) and outer (right) side of a shell of the marine snail *Haliotis laevis* (greenlip abalone). The diameter of a greenlip abalone shell is approximately 15 cm.

2.2. Abalone Nacre

In the greenlip abalone, *Haliotis laevis*, the thickness of the nacreous layer on the inside of the shells grows to the depth of a few millimeters. When a vertical fracture surface is imaged, e.g., by scanning electron microscopy (SEM), the fascinating structure of nacre can be observed, as shown in figure 2.2. Similar to a brick-wall, roughly polygonal mineral platelets approximately 500 nm in height and 7-12 μm in diameter are piled up in an extremely regular manner. The beautiful iridescent appearance of nacre is a result of this microscopic structure, as it causes the interference of light, which is reflected at different interfaces. The mineral platelets consist of the calcium carbonate (CaCO_3) polymorph aragonite. Isolated aragonite platelets are single crystals [Metzler et al., 2007] and have a

well defined crystallographic *c*-axis, which is perpendicular to the surface of the platelets [Zaremba et al., 1996]. The aragonite platelets are surrounded by organic material referred to as *organic matrix*, which is divided in the water insoluble *interlamellar matrix* and the *water soluble matrix*.

The brick-wall structure with an organic “mortar”, is responsible for the extraordinary mechanical stability of nacre. This exceptional stability is the main evolutionary purpose of the material, since the slow and soft molluscs need protection against predators. The properties of a hard but brittle mineral combined with a soft and elastic organic material greatly increase nacre's resistance to fracture. For the pure mineral, the initiation of a crack is more energy extensive, than crack propagation. In nacre, a vertically propagating crack can either initiate a crack in the next platelet or bypass the organically connected platelets. Hence, crack propagation in nacre requires more energy than in the pure mineral. Rough surface features of the aragonite platelets are also important for the mechanical properties, since they increase the frictional resistance to vertical platelet sliding [Barthelat et al., 2007], [Meyers et al., 2008].

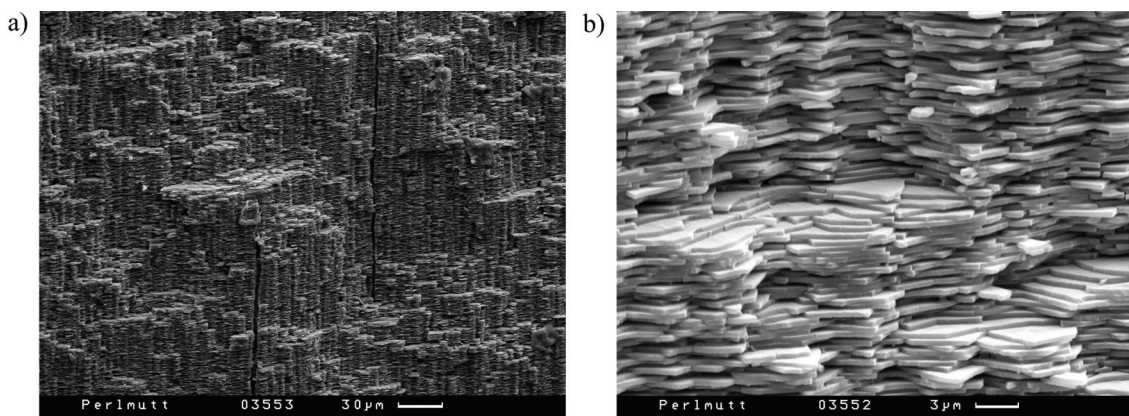


Figure 2.2.: SEM images of a vertical cross section of abalone nacre. Overview (a) and a close up view (b). The characteristic brick-wall like structure is visible, resulting in the mechanical strength and the iridescent appearance.

Interlamellar Matrix The interlamellar matrix, which surrounds the nacre platelets, can be obtained after demineralization of nacre. Demineralization can be performed with a weak acid (e.g., diluted acetic acid) or an ion binding agent (e.g., the calcium binding chelator EDTA¹). Pioneering transmission electron microscopic (TEM) investigations by Nakahara and colleagues revealed that the interlamellar matrix consists of a substructure of at least three sheets: an electron lucent inner layer enclosed by two electron dense layers [Nakahara, 1979]. The total thickness of an interlamellar matrix sheet is about 40 nm [Nakahara et al., 1982]. The core sheet was identified as the linear polysaccharide chitin [Weiss et al., 2002], possibly in the form of β -chitin [Falini et al., 2003]. Investigating the interlamellar matrix

¹Ethylene diamine tetraacetic acid

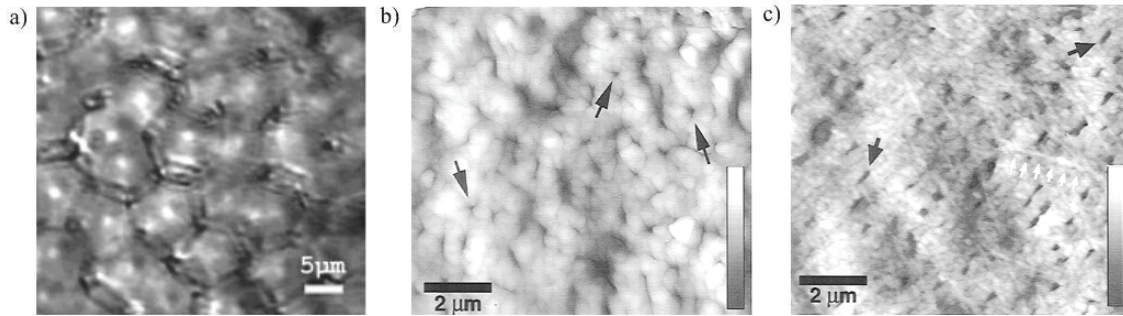


Figure 2.3.: Top views of the interlamellar matrix. (a) DIC light microscopy of the interlamellar matrix showing the intertabular matrix structure. From [Weiss et al., 2002]. (b) AFM image of the interlamellar matrix surface. Rounded proteinaceous features as well as pits (arrows) were observed. (c) AFM image of the interlamellar matrix core after protein digestion. Holes (black arrows) and fibres (white arrows) were visible. Figures (b) and (c): Height bar 0-60 nm. From [Schaeffer et al., 1997].

with scanning ion conductance microscopy and atomic force microscopy (AFM), confirmed that the matrix contains many pores [Schaeffer et al., 1997]. In AFM images, rounded features (presumably protein aggregates) of about 50 nm in diameter on the surface of the interlamellar matrix were observed, as well as pits (figure 2.3 (b)). After protein digestion, a network of fibres (presumably chitin) and holes were observed (figure 2.3 (c)). The distance between these holes was 20-100 nm and the diameter 5-50 nm. Hence, macromolecules and ions of the extrapallial fluid can easily cross the organic sheets. Staining experiments revealed that the interlamellar matrix seems to contain a chemically heterogeneous substructure underlying each platelet, possibly forming nucleating regions [Nudelman et al., 2006].

Digestion experiments with the collagen specific protease collagenase revealed that at least one of the interlamellar matrix proteins is collagenase sensitive [Schaeffer et al., 1997]. After digestion with the protease subtilisin, high amounts of prolin (a major amino acid in collagen) were found in the supernatant [Weiss et al., 2002]. Both results indicate the presence of a collagen-like protein in the interlamellar matrix.

Furthermore, it was suggested from X-ray data [Weiner and Traub, 1980], cDNA cloning and protein cleavage experiments [Sudo et al., 1997], that a silk fibroin-like protein (the chief protein found in spider and silkworm threads) is also present in the interlamellar matrix.

The so-called *intertabular matrix* is located laterally, separating the aragonite platelets and vertically connecting neighbouring sheets of the interlamellar matrix. In the top view, the intertabular matrix forms a characteristic honeycomb-like pattern with a diameter of 7-12 μm (see figure 2.3 (a)). In TEM investigations, this structure was reported as single layered and fuzzy [Nakahara, 1979]. In AFM [Arnoldi, 2001], as well as in DIC microscopic (differential interference contrast light microscopy) investigations [Weiss et al., 2002], the intertabular matrix had a fibrous appearance.

Water Soluble Matrix The water soluble fraction, obtained after the demineralization of nacre, is referred to as the *water soluble matrix*. Presumably, it is an assemblage of small molecules, peptides [Bédouet et al., 2006] and proteins. Some of the proteins are included in the mineral phase as intracrystalline proteins [Treccani, 2006], whereas others are located outside the mineral. Several water soluble proteins have been successfully purified from the water soluble matrix of abalone nacre. See table 2.3 (page 17) for an overview of known matrix proteins from abalone nacre, as well as the proposed function of each protein, derived from experimental data. Most of these proteins interact strongly with CaCO_3 . For a comprehensive overview, see [Marin and Luquet, 2004].

Calcium Carbonate Besides aragonite, two other polymorphic forms² of calcium carbonate are known (see table 2.1). The geologically most common form is calcite, since it is the most stable form of CaCO_3 , but aragonite is also found in sedimentary rocks. Vaterite is rarely found and usually only obtained by rapid crystallization. On long timescales it subsequently transforms into calcite.

Often, the polymorphs of CaCO_3 adopt a typical shape. Vaterite can be observed in a floret-like morphology, calcite crystallizes as rhombohedra and aragonite takes the form of elongated crystals (“needles”) with a roughly hexagonal base. Sometimes many aragonite crystals are bundled (see figure 2.4). This long axis of the aragonite crystals (direction of fastest growth) is aligned along the crystallographic *c*-axes of the aragonite unit cell. The *a*- and *b*-axes lie in the plane of the flat base of the crystals [Anthony et al., 1990], [Downs, 2006]. In contrast, in nacre aragonite platelets the *c*-axis corresponds to the flat side and the *a*- and *b*- axes to the laterally extended sides.



Figure 2.4.: Typical morphologies of CaCO_3 crystals. (a) SEM micrograph showing precipitated aragonite (left), vaterite (middle) and calcite (right). (b) Macroscopic rhombohedral calcite with the characteristic double refraction and (c) elongated aragonite crystal.

Table 2.1.: The CaCO_3 polymorphs calcite, aragonite and vaterite. Solubility is at 25° C, from [Plummer and Busenberg, 1982].

	Crystal system	density [g/cm^3]	solubility product [mol^2/l^2]
Calcite	Trigonal	2.71	$10^{-8.480}$
Aragonite	Orthorhombic	2.93	$10^{-8.336}$
Vaterite	Hexagonal	2.54	$10^{-7.913}$

²Crystals of the same stoichiometry, but with different crystal lattice.

2.2.1. Shell Growth

The growth of abalone shells (as well as mollusc shells in general) takes place in a specialized mineralization compartment between shell and mantle edge, referred to as the *extrapallial space*³. This space contains the so-called *extrapallial fluid*. Cells of the mantle epithelium induce the formation of the different shell layers by secretion of a specialized extracellular organic matrix into the extrapallial space. Figure 2.5 shows a schematic drawing of the shell growth for abalone⁴. In table 2.2 the inorganic composition of the extrapallial fluid, determined for a marine bivalve, is shown. The composition is similar to sea water, important deviations are the higher amount of dissolved CO₂, the lower pH-value and a slightly increased calcium concentration.

The cells located at the outermost mantle edge secrete the *periostracum*, an initial organic deposit (thickness: 100-200 nm for *H. rufescens* [Nakahara et al., 1982]). The next region of cells induces the growth of calcite layers and the innermost cells of the mantle epithelium induce the growth of nacre. The transitions between the different shell layers are very sharp (see figure 2.6 (c)), showing the strict control of the organisms over the mineral formation [Zaremba et al., 1996], [Sudo et al., 1997].

In experiments with inorganic substrates, carefully introduced between mantle epithelium and shell, an overgrowth with the order of the different shell layers, strongly resembling the order in the native shell, could be obtained (so-called flat pearls) [Fritz et al., 1994]. If the inorganic substrate already contained a previously grown nacre surface, the continuation of nacre overgrowth was observed [Zaremba et al., 1996]. Seemingly, individual cells of the mantle epithelium are not strictly limited to the production of one of the different shell layers, but are able to recognize the current state of the shell and switch between the production of the different layers by secreting different sets of macromolecules.

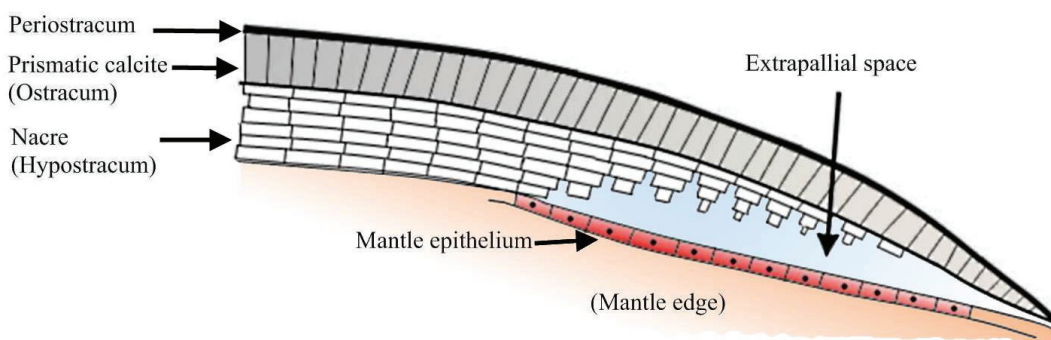


Figure 2.5.: Schematic vertical cross section (not to scale) of the outer mantle edge and the growing shell in *Haliotis*. The cells of the mantle epithelium control the composition of the extrapallial fluid. The different shell layers grow by a self-organization process. Initially (right), the organic periostracum is deposited, followed by the growth of prismatic calcite and nacre. Intermediate shell layers have been omitted for simplicity. Own drawing, partially adapted from [Zaremba et al., 1996].

³*Pallium*, Latin for cloak or mantle.

⁴Note: The details of shell growth and structure differ among the shell forming mollusc species.

Table 2.2.: Inorganic composition (average \pm standard deviation) of the extrapallial fluid of the blue mussel *Mytilus edulis* in comparison with sea water [Crenshaw, 1972]. No data are available for *Haliotis*, but a similar composition is assumed.

	Na ⁺ [mM]	K ⁺ [mM]	Ca ²⁺ [mM]	Mg ²⁺ [mM]	Cl ⁻ [mM]	SO ₄ ²⁻ [mM]	CO ₂ (aq) [mM]	pH-value
<i>Mytilus edulis</i>	442 \pm 10	9.5 \pm 0.5	10.7 \pm 0.6	58 \pm 3	477 \pm 8	23.7 \pm 1.2	4.2 \pm 0.5	7.39 \pm 0.16
Sea water	427 \pm 9	9.0 \pm 0.1	9.3 \pm 0.2	53 \pm 3	496 \pm 6	25.6 \pm 1.3	2.5 \pm 0.1	7.91 \pm 0.11

2.2.2. Nacre Growth

Figure 2.6 (a) shows a SEM image of the growth front of nacre from the abalone *Haliotis laevigata*. Stacks of aragonite platelets can be observed, forming a typical conical structure, often referred to as “Christmas trees”. The nacre growth region is often visible with the naked eye, at the border of the inner side of abalone shells, as a region of dull appearance.

The growing aragonite platelets are located between the interlamellar matrix sheets (figure 2.6 (b)). The intertabular matrix is located laterally, forming pockets which define the space of each aragonite platelet. Regions not yet filled by mineral are soaked with extrapallial fluid, containing the soluble matrix. The platelets grow laterally (in a- and b-direction) until neighboring platelets come in close contact separated only by the intertabular matrix [Nakahara, 1979]. The straight and conical structure of the stacks of growing platelets indicates a roughly constant lateral platelet growth. Until the final thickness of the nacre layer is achieved, new sheets of the interlamellar matrix are produced by the mantle epithelium.

Mineral Bridges It has been shown that the aragonite platelets are connected by mineral bridges through the porous interlamellar matrix [Schaeffer et al., 1997], [Gries et al., 2008] (see figure 2.6 (d)). For *Haliotis rufescens*, domains of 10-40 platelets with parallel a- and b- axes were reported. The domains were mostly vertical, but to some extent also extended laterally [Metzler et al., 2007]. Neighboring domains showed no correlation of the a- and b- axes. This implies that nucleation of aragonite takes place at several locations within the organic matrix, but not for each individual platelet. Seemingly, the nucleation process only influences the orientation of the aragonite c-direction, not the a- and b- orientation of the platelets.

Proposed Growth Mechanisms The detailed mechanisms which result in the formation of nacre (and other biominerals) are unknown. The following aspects of this controlled

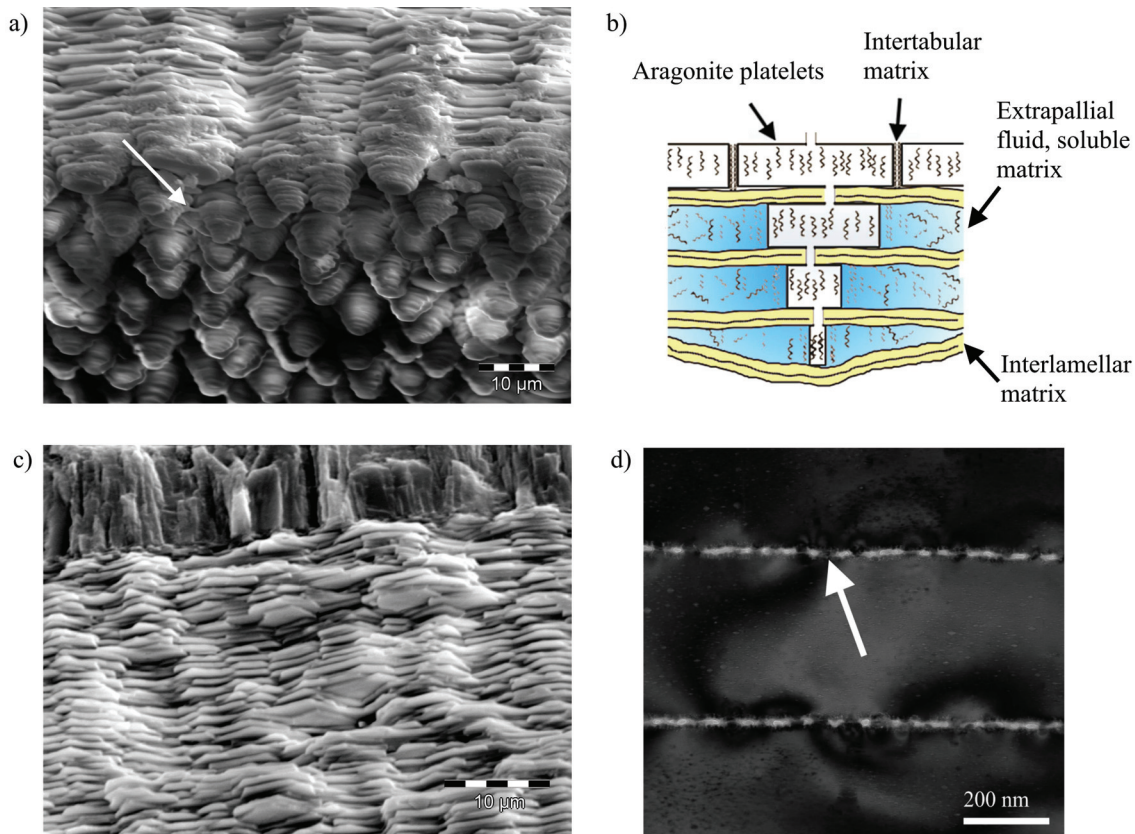


Figure 2.6.: (a) SEM image of the nacre growth region of abalone. Stacks of growing aragonite platelets can be seen in the lower part of the image. The arrow shows a remnant of the interlamellar matrix. (b) Schematic of nacre growth, adapted from [Blank et al., 2003]. The mineralization takes place in pockets of the interlamellar matrix soaked with ions and soluble matrix proteins. (c) SEM image of the transition between nacre and a calcitic shell layer. (d) Bright field TEM image of a nacre cross-section. The arrow points to one of the mineral bridges. Image kindly provided by K. Gries, University of Bremen.

mineralization process are especially notable:

- Polymorph control: Aragonite is nucleated exclusively.
- Orientation control: The *c*-axis of aragonite is oriented perpendicular to the surface of the interlamellar matrix.
- Morphology control: Aragonite in nacre grows in a highly unusual tabular shape compared to geological aragonite.
- Complete inhibition of uncontrolled nucleation in the supersaturated extrapallial fluid.

The so-called *ionotropic effect* was one of the first proposed models for the growth of nacre. According to this model, negatively charged proteins at the surface of the interlamellar matrix attract calcium ions, which subsequently attract carbonate ions and so forth. Since the (001) faces of aragonite and calcite are highly charged and almost identical [Mann, 1988], the oriented nucleation may be explained by this model but not the polymorph selectivity.

Another model proposed for the growth of nacre is *epitaxial growth* [Weiner et al., 1984]. Epitaxial crystal growth implies a spatial relationship between the matrix surface and the growing crystal. In this model, the whole matrix, or a nucleating region, contains carboxylic residues. These residues geometrically position the calcium ions in the correct two dimensional alignment, identical to the aragonite or calcite (001) face. In order to achieve this correspondance, an epitaxially nucleating β -sheet protein with Asp-X-Asp (X is a small and neutral amino acid) sequence patterns was proposed, which would match closely to the necessary distances to align calcium in the desired manner. However, so far no proof of the existence of such a surface protein has been published. Considering the rough surface of the interlamellar matrix (see figure 2.3), it is difficult to understand how the observed orientation of the *c*-axis perpendicular to the interlamellar matrix surface can be obtained. In addition, the selectivity for aragonite is not explained.

In recent years the model of *amorphous precursors* was developed. According to this idea, the space inside the organic matrix is initially filled by amorphous CaCO_3 , possibly secreted by the epithelial cells [Addadi et al., 2006]. This amorphous CaCO_3 subsequently undergoes a phase transition (Ostwald ripening) to the more stable form aragonite. According to this model, the primary role of the interlamellar matrix is to provide a space of defined shape. The phase transition is possibly induced by a nucleation center or surface charges. By artificially soaking the interlamellar matrix with charged polymers (as a model for polyanionic proteins), which are known to create amorphous colloidal CaCO_3 [Gower and Odom, 2000], it was possible to remineralize the interlamellar matrix with calcite [Gehrke, 2006]. However, no evidence for the existence of the precursors *in vivo* has been published.

So far, all models have weaknesses and none is supported by strong experimental data from crystallization experiments, structural analysis of the interlamellar matrix or investigations of nacre growth *in vivo*.

In all above described models, the role of the soluble matrix is not clearly stated⁵. However, studies showed a strong inhibiting ability of the total soluble matrix [Wheeler et al., 1981]. With ongoing success in the purification and characterization of matrix proteins, a strong interaction with calcium-carbonate *in vitro* was also found for most isolated nacre proteins (see table 2.3). Some matrix proteins promoted the crystal growth on calcite surfaces (perlucin, AP8 α , β), whereas others were inhibitory on a calcite surface or in precipitation experiments (perlwapin, perlinhibin, AP7, AP24). After incubation of a calcite surface with a supersaturated CaCO_3 solution in the presence of the nacre protein perlinhibin, overgrowth of aragonite was found, possibly by specific inhibition of calcite growth.

Hence, the possible role of the crystal interacting proteins from the soluble matrix might be the control of crystal shape (growth inhibition or promotion of specific crystal faces), polymorph (by specifically inhibiting calcite) and the general inhibition of uncontrolled

⁵Except for the polyanionic proteins in the model of amorphous precursors.

crystal growth from solution.

Finally, the ionic composition of the extrapallial fluid might also influence crystallization. For example, high magnesium contents, as present in the extrapallial fluid, favor aragonite growth [Kitano et al., 1976].

Table 2.3.: Published proteins from the organic matrix of the nacreous layer of the gastropod abalone (*Genus Haliotis*). The isoelectric point (pI) was calculated using the ExPASy server (Swiss Institute of Bioinformatics) [Bjellqvist et al., 1993]. The first 5 proteins have been isolated from the nacreous layer of *H. laevigata*, the others from *H. rufescens*. Lustrin A is presumably an insoluble matrix protein.

Protein	Sequence accession number	MW [kDa]	Most dominant amino acids	Calculated pI	Possible function	Reference(s)
Perlucin	P82596 (UniProt)	18.155	Leu (9.7 %) Arg (8.4 %) Ser, Gly, Asn (7.7 %)	7.2	Sugar binding, crystallization enhancer	[Weiss et al., 2000] [Blank et al., 2003]
Perlustrin	P82595 (UniProt)	9.338	Cys (14.3 %) Pro (9.5 %) Leu (8.3 %)	8.0	Insulin-like growth factor binding	[Weiss et al., 2000] [Weiss et al., 2001]
Perlwapin	P84811 (UniProt)	14.528	Cys (18.7 %) Pro (15.7 %) Gly (11.9 %)	8.6	Calcite growth inhibition	[Treccani et al., 2006]
Perlinhibin	P85035 (UniProt)	4.793	Cys (19.5 %) His (17.1 %) Arg (14.6 %)	8.3	Calcite growth inhibition, aragonite nucleation	[Mann et al., 2007]
Lustrin A	AF023459 (GenBank)	142.209	Ser (16.4 %) Pro (13.9 %) Gly (13.4 %)	8.1	Matrix-platelet adhesive, protease inhibitor	[Shen et al., 1997]
AP7	AF225916 (GenBank)	9.935	Leu (9.1 %) Arg, Cys, Ser, Tyr (8.0 %) Ala, Asp, Gly, Ile, Thr (6.8 %)	5.5	Calcite growth inhibition	[Michenfelder et al., 2003] [Elhadj et al., 2006]
AP8 α, β	not sequenced	7.8, 8.7	Gly (≈ 39 %) Asx (≈ 35 %) Glx (≈ 8 %)	-	Crystallization enhancer	[Fu et al., 2005] [Elhadj et al., 2006]
AP24	AF225915 (GenBank)	19.595	Thr, Asn (8.2 %) Ala (7.0 %) Asp, Val (6.4 %)	5.8	Calcite growth inhibition	[Michenfelder et al., 2003] [Elhadj et al., 2006]

2.3. Targets of the Thesis

2.3.1. Crystallization Templated by the Interlamellar Matrix

Although being the most prominent organic structure in nacre, the influence of the interlamellar matrix on CaCO_3 nucleation and growth was previously not well characterized and only sparsely investigated. Previous crystal growth experiments on nacre fracture surfaces indicated, that the interlamellar matrix has the ability to nucleate aragonite overgrowth, with the c -axis oriented identical to the c -axis of the aragonite platelets [Arnoldi, 2001]. The main obstacle for a more detailed investigation of the interlamellar matrix with respect to CaCO_3 crystallization was the absence of a suitable crystallization method. The widely used ammonium-carbonate method [Addadi and Weiner, 1985], as well as conventional double-diffusion systems [Falini et al., 2002] have severe disadvantages, like non-constant concentrations and a variable pH-value during the crystallization process.

However, potentially important surface properties of the matrix are pH-value dependent (e.g. carboxylic groups) and moreover, a too rapid crystallization may cover matrix induced effects on crystallization. Therefore, a device to crystallize slowly and under constant conditions should be developed. This newly developed device should be used to investigate the influence of the interlamellar matrix on CaCO_3 nucleation and growth.

2.3.2. Determining the Surface Free Energy of the Interlamellar Matrix

During the course of this thesis, the idea was developed, that a characterization of the interlamellar matrix with contact angles might be promising. When handling the interlamellar organic matrix in experiments, its hydrophobic properties were often noticed but not quantitatively determined. Further motivation was initiated by the finding that the interlamellar matrix may be a previously underestimated key factor for the growth of flat aragonite crystals (see section 4.1). It is known from classical nucleation theory on substrates, that crystallization may occur in a flat manner, especially when the surface free energy of the substrate is very high [Kashchiev and van Rosmalen, 2003]. But up to now, no surface free energy determination has been published for the interlamellar matrix of nacre.

Hence, it was promising to perform a determination of the surface free energy by contact angle measurements. Primarily, this should be done for a more detailed characterization of the interlamellar matrix but also possible implications on crystal growth should be considered.

2.3.3. Influence of the Soluble Matrix on Precipitation Rates

Some proteins found in gastropod nacre act as strong inhibitors of crystal growth *in vitro* e.g. AP7, AP24 [Michenfelder et al., 2003], perlwapin [Treccani et al., 2006] and perlinhibin [Mann et al., 2007], possibly preventing uncontrolled crystal formation during the growth of the material. Whereas others are known to enhance crystal formation *in vitro* e.g. the

C-type lectin perlucin [Weiss et al., 2000] or the acidic proteins AP8- α and AP8- β [Fu et al., 2005].

In order to characterize a protein as inhibitor or enhancer, crystallization studies are the method of choice. In 1981, a simple assay was published, in which a supersaturated CaCO_3 solution was created and the pH-value recorded, which decreases due to CaCO_3 precipitation. In the presence of organic matrix, the precipitation was decreased or completely inhibited [Wheeler et al., 1981].

To get an insight into the protein-crystal interaction on a molecular level, atomic force microscope (AFM) crystallization / dissolution experiments on calcite with nacre proteins in solution have been used widely, e.g. [Treccani et al., 2006], [Mann et al., 2007], [Blank et al., 2003], [Fu et al., 2005], [Giles, 1995].

Despite the advantages and numerous insights given by the crystallization studies, especially by AFM investigations, up to now they lack of easy measurable variables, which would allow a quantitative comparison of different biomineralizing compounds with respect to their function in CaCO_3 crystallization. Therefore, it was considered interesting to develop a complementary method to quantify the influence of proteins on CaCO_3 precipitation. A starting point was the precipitation method of Wheeler and colleagues mentioned above, which would be extended to a quantitative characterization of biomineralizing compounds. It was the aim to calculate CaCO_3 precipitation rates from the recorded pH-value by considering all chemical equilibria describing the system.

2.3.4. Amino Acid Analysis

In the literature concerning mollusc shell formation, acidic proteins with a high content of aspartic acid (and to a lesser extent glutamic acid) are considered very important for all parts of shell formation [Addadi and Weiner, 1985], [Gotliv et al., 2003]. This is based on reports of an extraordinarily high content of these amino acids in the soluble matrix of nacre (for *Haliothis* see: [Nakahara et al., 1982], [Bédouet et al., 2001], [Fu et al., 2005]). A strong electrostatic interaction of the charged amino acids with Ca^{2+} as well as influence on CaCO_3 nucleation and growth was postulated and found *in vitro* [Addadi and Weiner, 1985].

Yet, from the number of published nacre proteins from *Haliothis*, only the protein AP 8 [Fu et al., 2005] is likely⁶ to have an unusually high content of acidic residues (table 2.3 shows a compilation). None of the other proteins show acidic properties, which can also be seen from their isoelectric points (pI), which are not in the acidic range (e.g. pI < 5.0). Some authors attribute this gap to the unusual properties of the highly charged acidic proteins. Highly charged proteins are believed to adhere to surfaces (glassware, dialysis membranes) and bind only weakly to the anionic reagent SDS, used in SDS - PAGE, as well as to Coomassie Blue, the most common dye in SDS - PAGE [Goldberg and Warner, 1997].

⁶Until now, AP 8 has not been sequenced, but solutions with and without AP 8 have been subject to amino acid analysis.

Because of these contradictory results, an amino acid analysis of the soluble matrix from the nacreous layer should be performed - the first for *Haliotis laevigata*. The aim was to determine the amino acid composition in an independent study. This was considered important, because the given values in the literature are partially inconsistent and published chromatographic data is absent.

3

Material and Methods

3.1. Organic Material Extraction from Nacre

3.1.1. Nacre Preparation from Abalone Shells

Shells of the gastropod *Haliotis laevis* (obtained from Abalone Exports, Laverton North, Victoria Australia) were cleaned with water and a brush. Calcitic outer parts of the shells were removed by blasting with corundum slurry (Al_2O_3 , diameter 0.12-0.25 mm; slurry blaster WA70, Sigg, Jestetten, Germany). The nacreous shells were incubated for 2 min in a solution of 1:1 sodium hypochlorite (NaOCl) and ultra pure water¹ to remove organic contaminations from the surface. Hypochlorite and dissolved organic compounds were removed by extensive washing with ultrapure water. The remaining nacreous shells were crushed with a hammer in pieces of approximately 2 cm in diameter.

3.1.2. Preparation of the Interlamellar Organic Matrix

Dialysis tubes with a molecular weight cut-off (MWCO) of 6-8000 Da (SpectraPor3, Spectrum Laboratorys, Rancho Dominguez, USA) were prepared by heating up to 100° C in 3 mM ethylene diamine tetraacetic acid (EDTA), to remove the glycerol coating, inactivate proteases and eventual contaminations by heavy metal ions. The clean nacre pieces were demineralized by dialysis against 100 mM EDTA at a pH-value of 5 under constant stirring at 4° C. To prevent bacterial growth, 0.02% sodium azide (NaN_3) was added to the demineralization solutions. In order to ensure a rapid and complete demineralization, only one nacre piece per dialysis bag was used. The outer solution was exchanged every 1 - 2 days. Complete removal of mineral parts was indicated by the absence of CO_2 bubbles after \approx 20 days. After 30 days the demineralization dialysis was stopped. Total demineralization of the interlamellar matrix was confirmed by light microscopy, scanning electron microscopy of the surface and inner parts and by using Feigl's aragonite staining method (see section 3.3.3).

For storage, the interlamellar matrix was dialyzed against 10 mM sodium bicarbonate (NaHCO_3) with 0.02% NaN_3 , pH-value 8.4 at 4° C. The samples were used within one month after demineralization or discarded after this period.

3.1.3. Deproteination of the Interlamellar Organic Matrix

A buffer solution of 50 mM tris(hydroxymethyl)-aminomethane (TRIS), pH-value 8.0 and 5 mM CaCl_2 was prepared. 5 mg proteinase - K (Molecular Probes, Carlsbad, USA) was dissolved in 20 mL of this buffer (250 $\mu\text{g}/\text{ml}$). The calcium ions in the buffer stabilize proteinase-K, protecting it against slow autolysis [Bajorath et al., 1988]. Thin interlamellar matrix sheets were incubated in this solution at 40° C over night. To remove the proteinase,

¹Deionized water, further cleaned by a Milli Q Academic water purification device (Millipore, Billerica, USA).

the matrix sheets were extensively washed with a calcium free buffer solution, e.g., 10 mM NaHCO₃ with 0.02% NaN₃.

3.1.4. Preparation of the Water Soluble Organic Matrix

Clean nacre pieces were crushed with a jaw crusher (Pulverisette, equipped with ZrO₂ crushing jaws, Fritsch, Idar-Oberstein, Germany), resulting in pieces of up to 5 mm edge length. Dialysis tubes (MWCO 3500) were prepared by heating up to 100° C in 3 mM EDTA. The powder was dialyzed at 4° C against 6% acetic acid (v/v) with 0.02% NaN₃. In order to discharge the high amount of developing CO₂, the dialysis tube was placed in a large beaker containing the acetic acid, such, that the upper part was outside the solution and could be perforated. After one week, the supernatant of the solution was filtered with a 0.22 μm membrane filter.

For storage, the solution was dialyzed (MWCO 3500) against 20 mM NaHCO₃ with 0.02% NaN₃ at 4° C. In order to avoid possible effects of sodium azide in the experiments, a dialysis against 20 mM NaHCO₃ without NaN₃ was performed 12 h before experimental use.

The protein concentration of the soluble matrix was determined by the Bradford method (see section 3.2.1). Sodium dodecyl sulfate-polyacrylamide gel-electrophoresis (SDS-PAGE) in 10% gels of the protein solution was kindly performed by Meike Gummich, Biophysics Institute, University of Bremen, following established protocols.

3.2. Chemical Methods

3.2.1. Protein Concentration Determination (Bradford Assay)

For a determination of protein concentrations, the method of Bradford [Bradford, 1976] was used in the microassay form, suitable for protein concentrations in the range 1-10 $\mu\text{g}/\text{ml}$. The method is based on the binding of the dye Coomassie-Brilliant Blue G-250 to certain groups in proteins in an acidic solution. The dye binds primarily to the basic amino acid arginine, but also to other basic (His, Lys) and aromatic amino acids (Trp, Tyr, and Phe) [Compton and Jones, 1985]. Due to protein binding, the absorption maximum shifts, with a large difference at 595 nm. Figure 3.1 shows an absorbance spectrum of the dye in the visible light range with and without proteins present.

800 μl protein sample in a buffer and 200 μl dye reagent (Bio-Rad Protein Assay, Bio-Rad, Hercules, USA) are pipetted in a 1.5 ml plastic² cuvette (Plastibrand, Brand, Wertheim, Germany). Both solutions were mixed by shaking the parafilm covered cuvette. After 5 minutes, the absorbance at 595 nm was measured in a UV-VIS absorption spectrometer (1 cm pathlength).

By comparing the absorbance with a calibration measurement, using proteins at known concentrations, the unknown concentration can be obtained. The calibration measurements can be found in appendix A.5. At least two independently prepared measurements should be performed for each concentration determination.

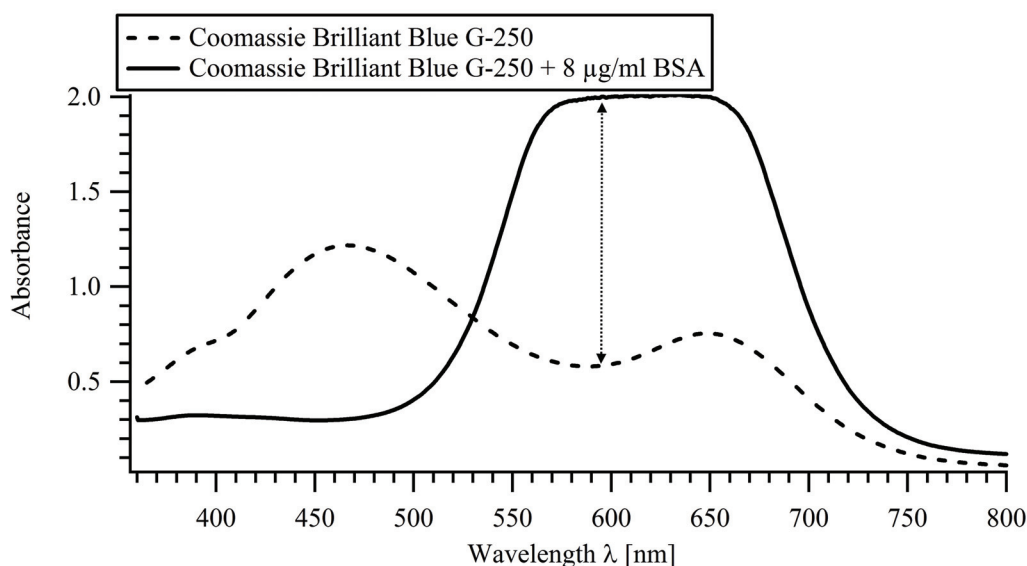


Figure 3.1.: The Bradford method for the determination of protein concentrations is based on an absorption shift of Coomassie-Brilliant Blue G-250 at 595 nm due to protein binding. Measurement of absorbance spectra of the dye without proteins and in the presence of BSA.

²Coomassie-Blue binds to quartz cuvettes.

3.2.2. Creation of Polymer Foils

Chitin Foils

For the generation of chitin films a slightly modified protocol, as described in [Khor et al., 1997], was used.

LiCl (4.8 g) in a glass flask was dried by heating to 110° C and cooled to room temperature after closing the bottle. The LiCl was dissolved in 100 mL N,N-dimethylacetamide. 0.48 g chitin flakes (from crab shells, 22720, Sigma Aldrich, Saint Louis, USA) were added to the solution and dissolved overnight under constant stirring. A thin layer of the dissolved chitin was poured into a glass petri-dish. The solvent was evaporated under a fume-hood. The chitin gel was washed by carefully filling the petri dish with water and dispensing it. Finally, the film was dried by flushing with nitrogen gas. The thickness of the resulting transparent films was tuneable by the thickness of the dissolved chitin prior to drying.

It was possible to create very thin, but homogeneous and robust films of approximately 0.1-0.2 mm thickness (for a photograph, see figure 3.7 (a)).

Chitosan Foils

For the generation of chitosan films a modified protocol, as described in [Aimoli et al., 2006], was used.

Chitosan 0.5% (m/v) (from crab shells, >85% deacetylated, Sigma Aldrich, Saint Louis, USA) was dissolved in 3% acetic acid and filtered (12-25 μm , black ribbon, Whatman, Maidstone, United Kingdom). A clean glass slide was covered with the filtrate and put in an oven at 50° C for 5 h to evaporate the solution. To separate the chitosan film from the glass, it was dipped for 5 h in 1M NaOH.

The resulting films were approximately 0.1-0.2 mm thick, transparent, homogeneous, and robust.

Carboxymethylated Cellulose and Chitin Foils

Thin films of chitin (preparation, see above) and regenerated cellulose were oxidized with 2,2,6,6-tetramethylpiperidine-1-oxyl radical (TEMPO) by Marcus Rauch (Bioengineered Ceramics Group, Prof. Dr. Cordt Zollfrank, University of Erlangen). The method changed the exposed C6 hydroxyl group of the glucose ring to a carboxylic group. The procedure was performed as described in [Isogai and Kato, 1998].

3.3. Characterization Methods for Crystallization Products

3.3.1. X-Ray Diffraction

Background

X-ray scattering is a non-destructive family of methods used to deliver various information about samples, such as crystal structure, orientation, and composition. In this work, X-ray powder diffraction (XRD) was used to identify the different CaCO_3 polymorphs calcite, aragonite and vaterite in samples after crystallization experiments. The basic operation principle is shown in figure 3.2 (a).

X-ray photons are created by the deceleration of fast electrons in an anode material. This creates a continuous radiation background (so called *Bremsstrahlung*), as well as characteristic radiation due to transitions of the atoms in the anode. For copper anodes, the typically used Cu K_α photons of $\lambda = 1.54 \text{ \AA}$ are created by the re-filling of a removed electron from the K shell ($n = 1$) by an electron of the L shell ($n = 2$). The background and other characteristic lines can be removed by using a suitable filter, resulting in roughly monochromatic radiation.

When the monochromatic X-ray photons pass through a crystalline sample, they are scattered from the lattice points of the crystal. For certain angles θ , a strong reflection can be observed. These angles are such, that neighboring rays from lattice planes with distance d can interfere constructively. Hence, for these angles, the pathlength between the X-rays is equal to the wavelength λ of the photons (or an integer factor $n\lambda$). Bragg's law describes this condition:

$$n\lambda = 2d \sin \theta \quad (3.1)$$

The geometric construction to derive Bragg's law is shown in figure 3.2 (b).

When XRD is used for the identification of unknown samples, the obtained maxima in the diffraction spectra are compared with a database. For powdered samples, containing a high number of small crystals with random orientation, a typical intensity distribution is achieved. A deviation of the observed intensity distribution from the powder diffraction pattern indicates a preferred orientation in the sample.

Experimental Procedure

Dried specimens of the precipitation or double diffusion experiments on cover glass slides were investigated by X-Ray diffraction (XRD) using Cu K_α - radiation (wavelength $\lambda = 1.54 \text{ \AA}$) with a theta / 2theta diffractometer (Seifert, General Electric Inspection Technologies, Lewistown, USA).

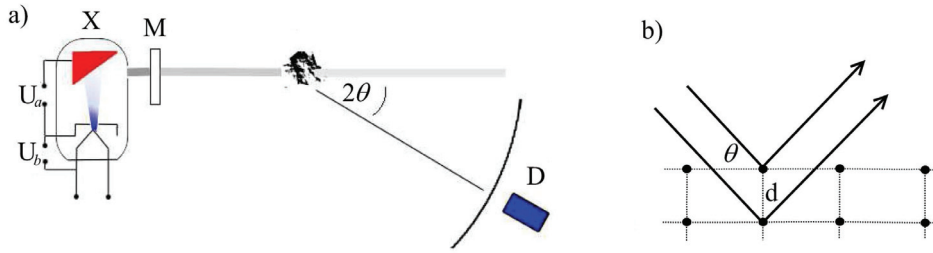


Figure 3.2.: (a) Operation principle of X-ray powder diffraction (transmission geometry). The X-ray tube (X) generates X-rays, which are filtered by a monochromator (M). The monochromatic X-rays pass a sample, where a part of the X-rays is diffracted and subsequently detected by a moveable detector (D). (b) Bragg diffraction occurs due to interference of radiation scattered on different points. For certain diffraction angles θ , given by Bragg's law, intense scattering can be observed, which depends on the distance d .

3.3.2. Scanning Electron Microscopy

Background

In scanning electron microscopy (SEM), a high energy electron beam is focused on a sample by a system of electromagnetic lenses and scanned over the sample surface *in vacuo*. In order to prevent charge accumulation on non-conducting samples (which would bend the electron beam), they are coated with a thin conducting layer, typically gold or carbon. Several interaction processes of the incident electrons with the sample can be used to obtain a topographic image of the sample, as well as information about the sample composition, e.g., by energy dispersive X-ray spectroscopy.

The high spatial resolution of an SEM of about 10 nm results from the short wavelength of the high energy electrons. The wavelength λ of the electron wave after acceleration with the energy E can be calculated according to:

$$\lambda = \frac{h}{\sqrt{2m_e E}} \quad (3.2)$$

For typical energies of 8-30 kV, the wavelength of the electrons is below 1 nm. The main resolution-limiting factor is the repulsion of the charged electrons in the electron beam.

In most scanning electron microscopes, a detector for secondary electrons is used on a routine basis. Secondary electrons are electrons removed from the shells of the gold-coat atoms by the incident high energy electrons. Typical energies of secondary electrons are 1-50 eV. The detection is performed using a laterally positioned scintillator-photomultiplier detector, which attracts electrons through a positively charged grid. Due to the relatively low energy of secondary electrons, only electrons from surface features pointing towards the detector have a good probability of reaching it. Hence, images obtained with this type of electrons have a distinct three dimensional appearance.

Detectors for back-scattered electrons are also frequently available. A portion of the inci-

dent electrons is back-scattered by elastic scattering. Thus, back-scattered electrons contain a high energy of several keV. Since back-scattering depends on the atomic number and the high energy electrons penetrate the sample volume several ten nm, this mode of operation contains information about the sample composition. Detection is usually performed using a semiconductor-detector placed above the sample. The resolution of this detection mode is lower in comparison to secondary electron detection, but it is not so sensitive to sample charging because of the higher electron energy.

Experimental Procedures

Dried specimens of the precipitation or double diffusion experiments on cover glass slides were gold coated with a sputter coater (K550, Emitech, Montigny, France) and investigated at 20 kV using a Camscan Series 2 (Cambridge Instruments, Cranberry Township, USA) scanning electron microscope in secondary or back-scattered electron imaging mode.

3.3.3. Aragonite Sensitive Staining (Feigl Test)

Aragonite can be distinguished from calcite by using the staining methods of Feigl [Feigl et al., 1973] and Meigen [Meigen, 1902]. These methods rely on the slightly higher solubility of aragonite compared to calcite. After etching of the crystal surface, the local pH-value will change stronger in the case of aragonite, which can be used for a precipitation reaction.

The aragonite staining was performed with the Feigl method, as described by Arnoldi [Arnoldi, 2001], [Kido, 1996]. 7.2 g $\text{MnSO}_4 \cdot \text{H}_2\text{O}$ was dissolved in 100 mL water and heated while stirring constantly. 1 g of Ag_2SO_4 was added and the solution was further heated until it started to boil. The solution was filtered with a paper filter. Afterwards, one droplet of 1 M NaOH was added to the solution. After 90 min, the solution was filtered again with a paper filter to remove precipitate and stored in a closed dark bottle.

To perform an aragonite determination, a droplet of the Feigl stain was added on the surface of interest. After a few minutes, the presence of aragonite was indicated by the formation of a black precipitate, whereas in the case of calcite, the solution remained clear.

3.4. Double-Diffusion Crystallization Experiments

3.4.1. Introduction

The influence of the interlamellar matrix of nacre and several other polymeric surfaces on CaCO_3 nucleation and growth was investigated with a newly developed double diffusion system. The double diffusion system was designed such that a constant composition of the diffusing solutions was given. This was achieved by a constant flow-by of the diffusing solutions. A detailed description of this newly developed double diffusion device can be found in the results section 4.1, where the necessity for the development of the system will be explained.

In the current section, the experimental conditions for the double diffusion experiments and the evaluation by scanning electron microscopy (SEM) and X-ray diffraction (XRD) will be described.



Figure 3.3.: Interlamellar matrix of nacre on a neoprene spacer ring before performing a double diffusion experiment. The diameter of the matrix disk is 14 mm.

3.4.2. Experimental Procedure

Double Diffusion Experiments

Crystallization experiments were carried out by double diffusion across an ion permeable membrane. The diffusing solutions were constantly renewed with a peristaltic pump to keep concentrations and pH-value constant and prevent crystallization in solution. Figure 4.4 in the results section shows a drawing of the experimental setup. Several types of membranes were used:

- Interlamellar organic matrix of nacre (preparation, see section 3.1.2)
- Interlamellar organic matrix of nacre deproteinated with proteinase - K (preparation, see section 3.1.3)
- Chitin film (preparation, see section 3.2.2)
- Chitosan film (preparation, see section 3.2.2)
- Cellulose film (MWCO 3500 dialysis membrane)
- Carboxymethylated cellulose film (preparation, see section 3.2.2)
- Carboxymethylated chitin film (preparation, see section 3.2.2)

Membrane pieces of 14 mm diameter were created with a punch and placed on a neoprene ring of 14 mm outer, 12 mm inner diameter and 0.48 mm height (see figure 3.3). In case of

very thin membranes, a second neoprene ring was placed on the other side of the membrane as a spacer. The two sides of the crystallization box were flown through by 20 mM CaCl₂ and 20 mM NaHCO₃ (pH 8.4), respectively, with a speed of 0.5 ml/min/side up to a total volume of 480 ml/side (\approx 10 h). At the end of the experiment the membranes were cut into halves and dried at room temperature on a glass cover slide with different sides to the top. As a control, identically treated excess membrane pieces (except mineralization) were kept and investigated with scanning electron microscopy.

Scanning Electron Microscopy

The specimens were cut into two pieces with a scalpel and dried on a glass cover slide. This was done such that of both sides (left and right side during the double diffusion experiment) one half was on top. The SEM investigation was performed as described in section 3.3.2.

X-ray Diffraction

Some specimens were investigated with X-ray diffraction. For this purpose, specimens were dried on a cover glass slide. The experimental conditions of the XRD experiments are described in section 3.3.1. In order to localize the CaCO₃ polymorph aragonite on some mineralized samples, an aragonite sensitive staining was performed, as described in section 3.3.3.

A part of the specimens (space filling mineralization in the insoluble matrix, nacre and powdered nacre from *Haliotis laevigata*) were investigated at the Institut für Röntgenphysik, University of Göttingen, Germany, with the aid of Anja Glisovič. A z-axis diffractometer equipped with bent collimating Göbel mirrors, motorized slits, and a fast NaI scintillation counter (Cyberstar, Oxford Instruments, Abingdon, United Kingdom) controlled by SPEC (Certified Scientific Software, Cambridge, USA) were used. The mirrors were optimized to select Cu K _{α} radiation.

3.5. Contact Angle Measurements

3.5.1. Introduction

The surface free energy of the interlamellar organic matrix of nacre was determined with contact angle measurements. The evaluation technique of Owens and Wendt [Owens and Wendt, 1969] was used, which is especially suitable for polymer surfaces. First, a brief introduction to the theory of surface free energy determination by contact angle measurements is given before the details of the practical implementation will be presented.

3.5.2. Theoretical Background

Surface Free Energy

If the surface of a sample is increased, for example by deformation of a liquid surface, work is required. To increase the surface, a number of molecules from the bulk have to move to the newly formed surface. There, the molecules will be situated at a phase interface with fewer favorable interaction partners compared to the bulk (figure 3.4). Hence, surfaces contain a specific (free) energy per unit area of a given substance, which corresponds to the work required to create that area.

Many effects known from everyday life arise from the existence of surface free energy: Small water droplets will form spheres to minimize their surface. Water striders can walk on water, because their hydrophobic feet cannot bend the water surface enough to penetrate it. Adhesives do not stick to Teflon³ coated cookware because its extremely low surface energy makes it energetically unfavourable.

For a more formal introduction, consider the work dW needed to change a surface area by an infinitesimal amount dA . Because new surface of the same sort is created it is obviously proportional to dA with the constant of proportionality γ :

$$dW = \gamma dA \quad (3.3)$$

At constant volume and pressure, this work dW equals the change in free energy dF , when changing the surface area A by an amount dA . Hence, the constant of proportionality in equation 3.3 can be written as:

$$\gamma = \left(\frac{\partial F}{\partial A} \right)_{V,T} \quad (3.4)$$

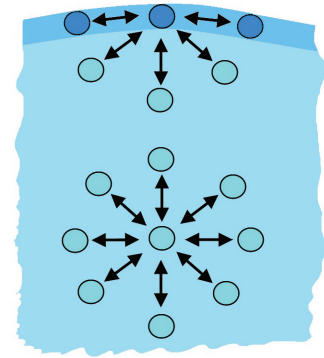


Figure 3.4.: The particles at the surface are at a higher energetic state than particles in the bulk, because they have fewer interaction partners. Therefore, the formation of surfaces is energetically unfavourable.

³poly-tetrafluoroethylene, Teflon is a brand name

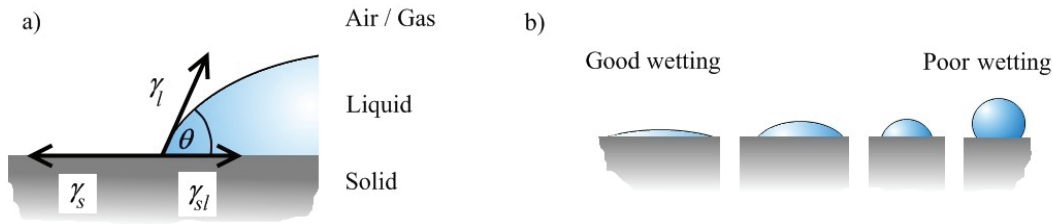


Figure 3.5.: (a) The contact angle θ of a droplet is a result of a balance between the solid surface tension γ_s , which tries to spread the droplet (minimizing free solid surface) and the liquid and interface surface energies γ_l and γ_{sl} which try to minimize contact between liquid and solid. (b) Examples of different wetting behaviors. In the case of water, the left surface would be termed hydrophilic and the right hydrophobic.

This defines the *surface tension* γ , which therefore corresponds to the work needed to increase a surface about unit area under constant volume and temperature [Atkins and De Paula, 2002], [Adamson, 1990]. Especially for solid surfaces, γ is often referred to as *surface free energy*, implying a surface of unit area. At interfaces of two condensed phases, γ is usually referred to as *interfacial tension*.

Since γ is constant, systems can lower their free energy ($dF < 0$) by reducing their surface ($dA < 0$). Therefore liquids will adopt shapes of minimal surfaces. For liquids, a number of methods for the direct measurement of surface tension are known. For example, the Wilhelmy slide method [Wilhelmy, 1863] or du Noüy's ring method [du Noüy, 1919] (for an overview of these and other methods, see [Adamson, 1990]). They all benefit from the free deformability of fluid surfaces according to external forces.

Young - Equation

The surface free energy of solid surfaces cannot be measured directly. However, the contact angle of a droplet on a solid surface contains information about the solid surface tension γ_s . If a liquid is brought into contact with a solid (figure 3.5), the resulting contact angle depends on the three involved surface tensions. The surface tension of the liquid γ_l and the newly formed solid - liquid interface γ_{sl} act to minimize contact area, whereas the solid surface tension γ_s acts to maximize contact area. The result is described by the Young equation:

$$\cos \theta = \frac{\gamma_s - \gamma_{sl}}{\gamma_l} \quad (3.5)$$

First of all, contact angles allow the classification of materials as hydrophobic (high contact angle with water), hydrophilic (low contact angle with water), or something in-between. By finding expressions for γ_{sl} , which depend on known variables, it is possible to measure γ_s . The Fowkes and Owens-Wendt models discussed below are of this type. A different approach (which minimizes γ_{sl} and therefore allows to estimate γ_s) was developed prior to the Fowkes and Owens-Wendt models, and will be discussed briefly.

Critical Surface Tension

In the 1950's, Zisman and colleagues developed a semi-empirical approach, where several measurements with different liquids were performed and plotted against $\cos \theta$ (figure 3.6 (a)) [Fox and Zisman, 1950]. The hypothetical surface tension where the liquid would spread completely, e.g. $\cos \theta = 1$, was referred to as the *critical surface tension* γ_{crit} of the solid. This critical surface tension was often identified as the surface tension of the solid. Two aspects argue against this: First, the relationship between $\cos \theta$ and γ_l in equation 3.5 is not always linear, but Zisman's approach uses a linear extrapolation to obtain γ_{crit} . Second, the interfacial tension γ_{sl} is not necessarily zero at $\cos \theta = 1$, which has to be the case when $\gamma_s = \gamma_{crit}$ (compare equation 3.5). Nonetheless, if the method of critical surface tension is used carefully, it will narrow down the value of solid surface tension and will help to predict wetting behavior.

Interfacial Tension - Fowkes Model

In 1964, Frederick Fowkes developed a model for the interface tension γ_{sl} , for systems where the interaction partners can interact only via London dispersion forces. As an example, Fowkes used an hypothetical interface between a saturated hydrocarbon and mercury. In mercury, mainly two types of interatomic forces are present: the metallic bond and London dispersion forces (induced fluctuating electric dipoles). The attraction between saturated hydrocarbons is entirely due to London dispersion forces. Fowkes assumed that the surface tension of mercury can be divided into a dispersion and metallic part $\gamma_{Hg} = \gamma_{Hg}^d + \gamma_{Hg}^m$. This is justified by the fact that the surface tension arises independently from the different types of intermolecular forces. For interfaces, where the partners can interact only via London dispersion forces, he proposed the use of the geometric mean:

$$\gamma_{sl} = \gamma_s + \gamma_l - 2\sqrt{\gamma_s^d \gamma_l^d} \quad (3.6)$$

For equal substances with only dispersion forces acting (e.g. two hydrocarbons) the interfacial surface tension disappears. If one of the two substances has only a very low dispersion component, the interfacial surface tension will be high. Theoretical calculations about London interactions at interfaces and empirical data verified the use of above equation 3.6 [Fowkes, 1964].

Interfacial Tension - Owens and Wendt Model

An extension to this model for the interfacial tension was introduced in 1969 by Owens and Wendt [Owens and Wendt, 1969], who developed a semi-empirical model suitable for polymer-liquid interfaces [Żenkiewicz, 2007]. Similar to Fowkes, they separated the surface tension of any nonmetallic liquid or surface into a polar (containing hydrogen-bonding and dipole-dipole interactions) and a dispersive component (containing dipole-apolar and apolar-apolar

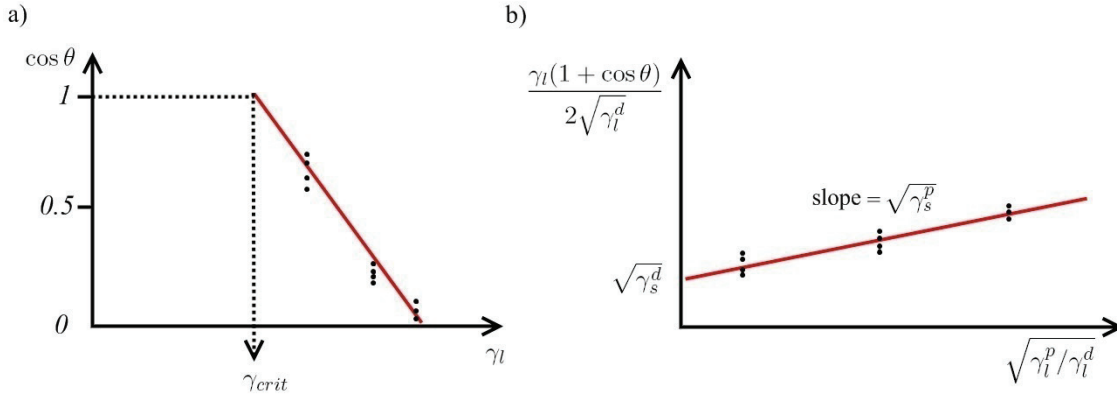


Figure 3.6.: (a) Zisman plot. The critical surface tension γ_{crit} is obtained by extrapolation to $\cos \theta = 1$. (b) Owens-Wendt plot. The surface tension is treated as sum of dispersive γ_s^d and polar γ_s^p component. Two or more liquids with known γ_l^d and γ_l^p are applied on a surface and plotted as shown above. The components of the solid surface tension are obtained as the square root of the slope and the vertical axis intercept of the linear fit.

interactions):

$$\gamma = \gamma^d + \gamma^p \quad (3.7)$$

For the interfacial tension they assumed the expression:

$$\gamma_{sl} = \gamma_s + \gamma_l - 2\sqrt{\gamma_s^d \gamma_l^d} - 2\sqrt{\gamma_s^p \gamma_l^p} \quad (3.8)$$

which follows the principle that interfaces of similar substances are energetically favorable. If this expression is combined with the Young equation 3.5, the following equation results:

$$\cos \theta = \frac{\gamma_s - (\gamma_s + \gamma_l - 2\sqrt{\gamma_s^d \gamma_l^d} - 2\sqrt{\gamma_s^p \gamma_l^p})}{\gamma_l} \quad (3.9)$$

This can be rearranged to the following very useful equation:

$$\frac{\gamma_l(1 + \cos \theta)}{2\sqrt{\gamma_l^d}} = \sqrt{\gamma_s^d} + \sqrt{\gamma_s^p} \sqrt{\frac{\gamma_l^p}{\gamma_l^d}} \quad (3.10)$$

The term on the left side depends only on the contact angle and values of the dispersive and polar surface tension components for various liquids which can be found in the literature (see table 3.1). If it is plotted against $\sqrt{\gamma_l^p / \gamma_l^d}$, a linear relationship is expected with the unknown $\sqrt{\gamma_s^d}$ as intersection with the vertical axis and $\sqrt{\gamma_s^p}$ as the slope. Therefore (by measuring the contact angle of two or more liquids on a solid surface and a line fit) it is possible to obtain the surface tension components of the solid (figure 3.6 (b)).

Other expressions for the interfacial tension γ_{sl} have been described in the literature. Wu's method divides the interfacial tension into a dispersive and polar component like the

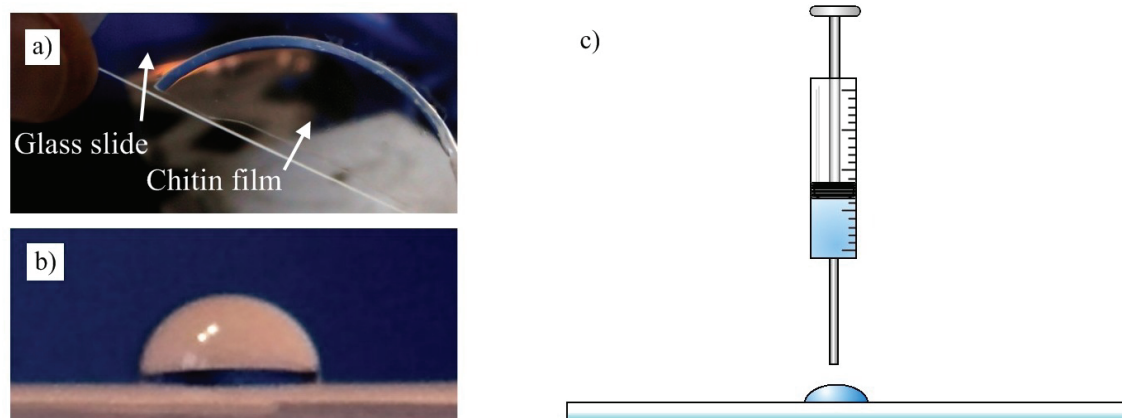


Figure 3.7.: (a) Chitin film on a glass slide before contact angle measurement. (b) Example image of a contact angle (water on paraffin). Droplet diameters were typically in the range of 2-4 mm. (c) The sessile drop method. A small droplet of a test liquid is applied onto a glass slide coated with material to investigate. Images were taken immediately after equilibrium was achieved.

Owens-Wendt model, but uses the harmonic mean instead of the geometric mean and is especially suitable for low energy surfaces [Wu, 1973]. The approach of van Oss, Good and Chaudhury divides the surface tension into a van der Waals component and a Lewis acid-base component comprised of electron donor and acceptor properties [van Oss et al., 1988].

The application of one of the different theoretical models on contact angle measurements may result in different values for the surface tension or surface tension components (see for example [Gindl et al., 2001] or [Żenkiewicz, 2007]). Therefore, the quantities obtained should be interpreted carefully and not necessarily considered as absolute values. Furthermore, it should be kept in mind that roughness and chemical homogeneity of the investigated surfaces as well as the swelling behavior modify the resulting contact angle.

3.5.3. Experimental Procedure

The following surfaces were investigated with contact angle measurements:

- interlamellar organic matrix of nacre (preparation, see section 3.1.2)
- interlamellar organic matrix of nacre deproteinated with proteinase - K (preparation, see section 3.1.3)
- chitin film (preparation, see section 3.2.2)
- paraffin wax

In the case of the biopolymers, flat specimens with an edge length of several cm were carefully placed on glass microscope slides. The biopolymer coated microscope slides were flushed with nitrogen gas until the surfaces were completely dry and flat (figure 3.7 (a)). In the

Table 3.1.: Total surface tension γ_l with dispersive γ_l^d and polar γ_l^p component of the used test liquids.

	γ_l [mN/m]	γ_l^d [mN/m]	γ_l^p [mN/m]	Reference
Water	72.8	22.1	50.7	[Chen et al., 2001]
Formamide	58.2	39.5	18.7	[Chen et al., 2001]
Diiodomethane	50.8	48.5	2.3	[Chen et al., 2001]
Glycerine	63.4	37.2	26.2	[Zhang et al., 2001]
Ethylene	48.3	29.3	19.0	[Zhang et al., 2001]
Dimethylsulfoxide (DMSO)	43.6	34.9	8.7	[Smith and Pitrola, 2000]
Dimethylformamide (DMF)	37.3	32.4	4.9	[Smith and Pitrola, 2000]

case of the paraffin wax, glass microscope slides were coated by dipping the slides in molten paraffin wax, so that a very smooth paraffin surface was achieved.

The contact angle measurements were performed at room temperature with the sessile drop method. For each measurement $3 \mu\text{l}$ test liquid was gently placed onto the investigated surface using a microliter syringe (figure 3.7 (b), (c), see table 3.1 for a list of test liquids used). At least three different liquids were used for each surface with a minimum of six individual experiments per test liquid on a surface. In order to minimize contamination of the test liquids, the syringe was cleaned extensively when changing the test solution. Cleaning was performed by flushing the syringe several times with ultrapure water before flushing it several times with the test liquid.

After achieving equilibrium, images were captured as quickly as possible to avoid reduction of the contact angle due to fluid absorption by the surface. Equilibrium was typically achieved after one or two seconds depending on the viscosity of the liquid. Images of droplets were captured with a commercial digital camera (DSC-T100, Sony, Berlin, Germany) under optimized illumination conditions. Each surface spot was only used once because of possible deformation or chemical modification of the surfaces by the test liquids. The contact angle was calculated with the equation $\theta = 2 \arctan(2h/d)$ (which can be derived from basic trigonometry) by measuring height h and diameter d of the droplets with computer graphic software (Canvas 9, ACD Systems, Victoria, Canada).

3.6. CaCO₃ Precipitation Assay

3.6.1. Introduction

CaCO₃ precipitation experiments were performed, using a previously published method [Wheeler et al., 1981]. This method was extended in order to calculate CaCO₃ precipitation rates, which is described in the results section (see 4.3). Here you find the experimental details of the precipitation experiments.

Additionally, infra-red light absorption measurements were performed during some precipitation experiments to characterize the turbidity of the solution. Furthermore, the precipitated CaCO₃ crystals were analyzed by X-ray diffraction and scanning electron microscopy.

3.6.2. Experimental Procedure

Precipitation Assay

60 ml of a 20 mM carbonate solution was prepared in a 200 ml Duran glass vessel (Schott, Mainz, Germany) by dissolving NaHCO₃ in ultra pure water and adding 0.5 ml 0.05 M NaOH to increase the initial pH - value. In some experiments bovine serum albumin, lysozyme or the soluble nacre protein fraction (see section 3.1.4) was added to the carbonate solution. A solution of 60 ml 20 mM CaCl₂ was prepared by dissolving CaCl₂*2H₂O in ultra pure water.

To start precipitation the CaCl₂ solution was rapidly poured into the vessel containing the NaHCO₃ solution. The vessel was stirred at constant rate, to achieve good homogeneity of the solution. To reduce the amount of CO₂ exchange with the environment, the solution was covered with an aluminum foil. All experiments have been performed at room temperature (18-24° C). At least six experiments per data point have been performed.

pH - Value Determination

The pHvalue was measured with a single-rod measuring electrode (WTW SenTix Mic, Weilheim, Germany) connected to a pH meter (PP-20, Sartorius, Göttingen, Germany). The electrode was calibrated once a week at pH 4, 7 and 9 by using standard calibration buffers. After each experiment the electrode was dipped in 1 M HCl for 5 min and ultra pure water to remove precipitate crystals and protein remnants. Between experiments the clean electrode was stored in 3 M KCl solution. Data was collected from the pH meter with a computer using the scientific software package IGORpro (WaveMetrics, Portland, OR, USA) in 3 s intervals over RS 232 connection.

Infra Red Absorption Measurement

In some experiments infra red (IR) absorption of the solution was measured with a self-made electrode containing a IR light emitting diode (SFH 484, Siemens, Munich, Germany) and IR phototransistor (LPT 80 A, Siemens, Munich, Germany). The phototransistor was

operated in the regime where it responds linear to the light intensity. Data was collected with an analog to digital board (National Instruments, Austin, USA) in 3s intervals with a computer using the scientific software package IGORpro. Experiments with absorption measurements were not included in the rate calculations, because in such experiments the higher hetero surface area (beaker and sensor surface) resulted in clearly enhanced rates. Those experiments were performed with fully enveloped beakers to reduce ambient light. A detailed circuit diagram and an image of the sensor can be found in appendix A.4.

Scanning Electron Microscopy

The precipitate was collected at the end of some mixing - experiments with a pipette and dried on a glass cover slide. The dried precipitate was investigated by scanning electron microscopy as described in section 3.3.2.

X-ray diffraction

The dried precipitate on cover glass slides was investigated by X-Ray diffraction as described in section 3.3.1.

3.7. Amino Acid Analysis

3.7.1. Introduction

The amino acid composition (percentage of the different amino acids) of the water soluble organic matrix of nacre from *Haliotis laevigata* was investigated. Amino acid analysis was performed by high performance liquid chromatography (HPLC) separation of phenylisothiocyanate (PITC) derivatives of amino acids obtained by hydrolysis of the soluble matrix [Heinrikson and Meredith, 1984]. After demineralization and isolation of the soluble matrix, four different approaches to investigate the amino acid composition were performed.

First, the soluble matrix was examined without further treatment. Because the soluble matrix is presumably a complex mixture, three further approaches to purify the matrix proteins were carried out: 1.) Amino acid analysis was performed after ultracentrifugation of the soluble matrix. 2.) The amino acid composition was also investigated after ZipTip⁴ purification. 3.) The soluble matrix was purified by cation ion exchange chromatography and analyzed by amino acid analysis.

The current section starts with a description of the background of the methods used (see subsection 3.7.2). First, an introduction to HPLC based amino acid analysis utilizing PITC derivatives is given, before basic principles of HPLC are explained. The section concludes with the details of the practical implementation (see subsection 3.7.3).

3.7.2. Theoretical and Methodical Background

Amino Acid Analysis by HPLC Separation of Phenylthiocarbamyl (PTC) Amino Acids

Amino acid analysis utilizing phenylthiocarbamyl (PTC) amino acids is performed in several steps, which are illustrated in figure 3.8. The starting point is usually a protein mixture, which should be analyzed. This protein mixture is hydrolyzed to obtain the free amino acids. The most common technique to hydrolyze proteins is using 6 M HCl for 24 h at 110° C [Fountoulakis and Lahm, 1998]. Ideally, the acid hydrolysis breaks only peptide bonds between the amino acids without further modifying them. In a good approximation,

⁴Specialized pipette - tips filled with octadecyl functionalized porous silica.

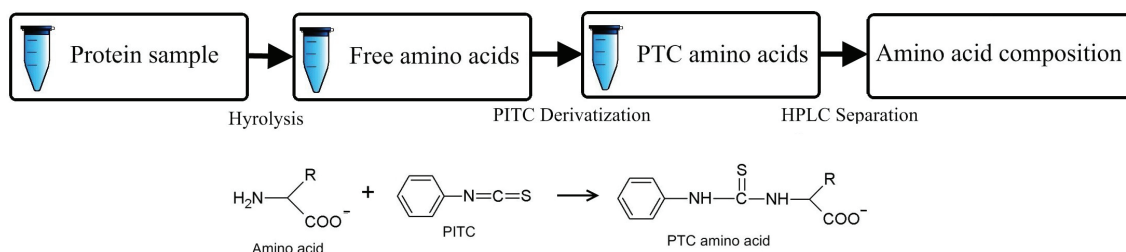


Figure 3.8.: Overview flow scheme of amino acid analysis with phenylthiocarbamyl (PTC) amino acids and HPLC. Below, the derivatization of an amino acid with phenylisothiocyanate (PITC) to a PTC amino acid is shown. Own drawing, adapted from [Janssen et al., 1986].

this is the case for most amino acids, with the special exceptions of glutamine, asparagine and cysteine.

During HCl hydrolysis, glutamine and asparagine will be converted to glutamic or aspartic acid, respectively. A method to individually determine glutamine / glutamic acid and asparagine / aspartic acid is the chemical modification of glutamine and asparagine before hydrolysis. By reaction of denatured proteins with [bis(trifluoroacetoxy)iodo]benzene (BTI), glutamine and asparagine will be converted to diaminopropionic or diaminobutyric acid [Soby and P., 1981] and therefore will not react to the acid forms during hydrolysis. The proportions of glutamine / glutamic acid and asparagine / aspartic acid can then be determined by two independent determinations of a BTI treated and an untreated sample.

Cystine (Cys₂, the dimer of cysteine) and cysteine are relatively unstable during acid hydrolysis, especially in the presence of carbohydrates [Gehrke et al., 1985]. An easy and reliable method to determine cysteine content is to perform an additional hydrolysis in the presence of sodium azide, which oxidizes cysteine and cystine to cysteic acid [Manneberg et al., 1995]. PTC-cysteic acid is stable and can be easily detected by HPLC.

Some amino acids (especially tyrosine and histidine) are partially destroyed by halogenation with increasing hydrolysis time. This can be greatly reduced by adding the scavenger phenol to the hydrolysis solution [Janssen et al., 1986].

After protein hydrolysis, the next step is the derivatization of the free amino acids to make them easily detectable by a light absorption measurement after chromatographic separation. In this work the widespread method of pre-column derivatization with phenylisothiocyanate (PITC) is used. The reaction behaviour of PITC with amino acids is well known. PITC is used in Edman degradation of isolated proteins (a method for amino acid sequence analysis developed by Pehr Edman more than 50 years ago) [Edman, 1950]. Under mild alkaline conditions, PITC reacts with the amine group of amino acids (including the secondary amino acids proline and hydroxyproline) resulting in phenylthiocarbamyl (PTC) amino acids (see figure 3.8). Alkaline conditions are provided by triethylamine (TEA), present in the coupling solution. At room temperature, the coupling reaction is essentially complete in less than 10 minutes. Excess PITC is volatile and can be removed by drying the sample in a rotary evaporator [Cohen and Strydom, 1988].

The last step in the amino acid analysis procedure is the chromatographic separation of PTC-amino acids by HPLC, which takes less than 30 min without column equilibration and cleaning times. After separation, the PTC-amino acids can be easily detected and quantified by measuring UV-light absorption at 254 nm. Under optimal conditions, the detection sensitivity of PTC-amino acids is in the low picomolar range [Cohen and Strydom, 1988], [Janssen et al., 1986]. To quantify the amount of each amino acid, it is necessary to perform a calibration for each amino acid. Amino acid standards of a number of concentrations were PITC derivatized and separated by HPLC. For each amino acid the peak area is plotted

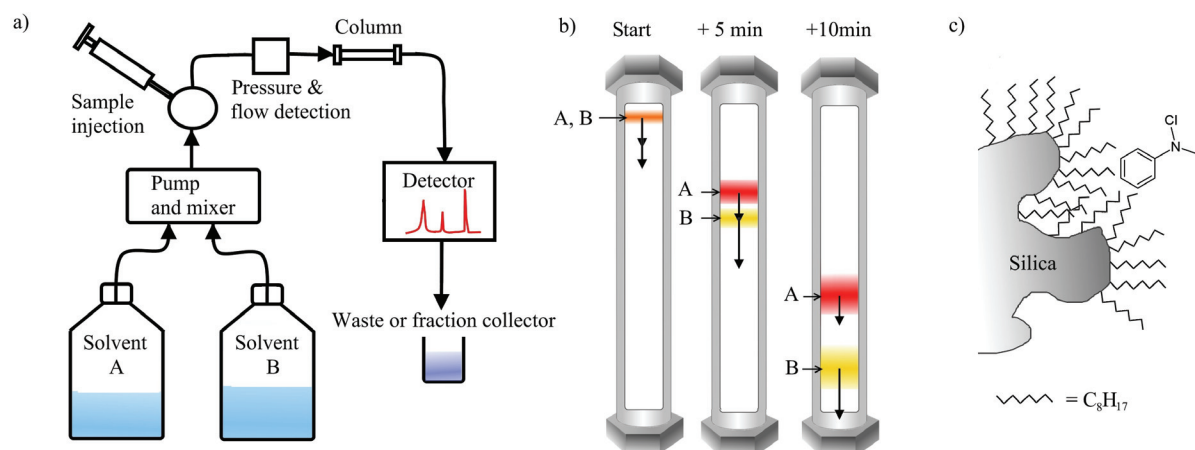


Figure 3.9.: (a) Diagram of a HPLC system. One or more solvents are mixed and transported by a pump. A mixture of compounds can be injected in the flow path and transported through the column. The interaction of the column material and the solvents separates some or all of the compounds. A detector (usually connected to a computer) detects the passing of compounds, e.g. by UV absorbance measurement. (b) Example separation of two compounds A (red) and B (yellow). Initially A and B are mixed (orange). With advancing time the compounds A and B will be separated, because A has a stronger interaction with the column material and migrates slower than B. Diffusive processes of the analytes in the column cause peak broadening (strongly overemphasized for illustrative purposes) with increasing run time. (c) Schematic surface of a C8 reversed phase silica particle. The silica is functionalized with octadecyl chains, which interact with apolar parts of analyte molecules. Own drawings, adapted from [Lindsay, 1987] (a) and [Dong, 2006] (b, c).

against the concentration, resulting in a linear relationship (unless the HPLC column is overloaded). Unknown concentrations of the sample can be obtained by measuring the peak area of each amino acid and comparing it with the linear fit to the calibration data.

High Performance Liquid Chromatography

In general, chromatography is a set of methods to separate mixtures of compounds (the *analytes*). Chromatography can be used for the purification of compounds from a mixture or for quantitative analysis. The separation is achieved by transportation of the analytes dissolved in a *mobile phase* (a gas in gas chromatography or a liquid in liquid chromatography) through a *stationary phase* interacting with both analytes and mobile phase.

High performance liquid chromatography (HPLC) is a modern form of liquid chromatography (LC), which allows the usage of stationary phases in the form of very small particles (typically spherical, 3-10 μm in diameter) packed in a column. The use of small particles improves resolution and reduces analysis time, but requires high pressure for delivery of the mobile phase [Lindsay, 1987]. The components of a basic HPLC system are shown in figure 3.9 (a). One or more solvent reservoirs contain the mobile phases. A high pressure pump generates the flow. The sample loop allows injecting of a sample into the system. The column (ideally) separates the sample. Behind the column a detector is placed (most often UV-VIS absorbance detectors but many other types, such as fluorescence or conductivity

detectors, are also used) to observe the passing of compounds, which can be discarded or collected in fractions.

In figure 3.9 (b) the separation process of two substances (A and B) is shown in more detail. The migration speed of analytes depends on the strength of interaction between the analyte and the stationary phase. Additionally, the mobile phase always competes with the analytes at the stationary phase surface. Substance A interacts more strongly with the stationary phase than B. Therefore it migrates more slowly, resulting in a higher retention time. The separation can be performed either isocratic - with constant mobile phase composition - or in the gradient mode, where the composition of the mobile phase is changed over time. The latter is often advantageous for the separation of complex mixtures, but requires a more complex instrumentation and the development of a suitable gradient can be a time consuming process.

Most often, reversed phase (RP) columns are used⁵. RP - HPLC columns contain porous silica particles, functionalized with alkyl groups. The interaction of the analytes with the stationary phase is based on apolar interaction (van der Waals forces and solvophobic or hydrophobic effect). As a rule of thumb in RP - HPLC, the more polar and the smaller a compound is, the earlier it will appear in the chromatogram. Common RP materials are C4 (butyl) functionalized silica for proteins and C18 (octadecyl) functionalized silica for small proteins, peptides and organic molecules. In gradient separations the first solvent is usually an aqueous buffer with low affinity to the RP - column, which is increasingly mixed with an organic solvent with low polarity like acetonitrile, methanol, tetrahydrofurane or hexane. The more apolar the mobile phase composition is, the stronger is the driving force for analyte migration.

Besides RP - HPLC and normal phase HPLC, other separation modes known from column based LC are also available for HPLC systems. Of importance for this work (although used in an LC system) is ion exchange chromatography (IAC). In IAC the column material has negative (cation exchanger) or positive ionic groups at the surface (anion exchanger). Molecules are separated by electrostatic interaction with counter-ions of the column material. In IAC, mobile phases are aqueous salt or buffer solutions. Often gradients of increasing ionic strength are used. Ions from the mobile phase compete with analyte molecules at the charged stationary phase surface, forcing the analyte migration.

Good starting points for further reading about HPLC and chromatographic separation techniques are [Lindsay, 1987], [Lottspeich and Engels, 2006] and [Dong, 2006].

⁵The term reversed phase is of historical origin, as normal phase HPLC (unmodified silica particles with silanol groups interacting with the analytes) was developed first.

3.7.3. Experimental Procedures

Preparation of water soluble organic matrix of nacre

The water soluble organic matrix of nacre from *Haliotis laevigata* was obtained by demineralization with 6% acetic acid. The solution was always filtered using a 0.22 μm filter. For details, see section 3.1.4. This solution was investigated by amino acid analysis without further purification (1.) and after each of the following purification methods: ultracentrifugation (2.), C18 ZipTip purification (3.) and cation-exchange purification (4).

Ultracentrifuge purification: The water soluble matrix was obtained by demineralization with 6% acetic acid as described in section 3.1.4. 120 ml of a solution containing 35 $\mu\text{g}/\text{ml}$ protein (determined by Bradford assay, see section 3.2.1) was ultracentrifuged at 44000 rpm for 2 h at 4° C (LE-80K, Beckman Coulter, Fullerton, USA). The supernatant was used for amino acid analysis.

ZipTip purification: The water soluble matrix was obtained by demineralization with 6% acetic acid as described in section 3.1.4. 22 μg (protein content determined by Bradford assay) of a frozen soluble matrix sample, previously dried by rotary evaporation, was re-dissolved in 30 μl water with 0.1% (v/v) trifluoroacetic acid (TFA). The soluble matrix was then treated with specialized pipette tips, which contain octadecyl functionalized porous silica particles (C18 ZipTip, Millipore, Billerica, USA). The protocol proposed by the manufacturer was followed. 10 ml of each of the following three solutions were prepared:

- An *equilibration and washing solution* containing water with 0.1% TFA
- A *wetting solution* composed of 100% acetonitrile
- An *elution solution* composed of 50% acetonitrile with 0.1% TFA

The following steps were performed to purify the samples:

1. Wetting and equilibration:

The silica particle surface was wetted by soaking and dispensing 10 μl wetting solution with a pipette (2x). Then, the ZipTips were equilibrated by soaking and dispensing 10 μl equilibration solution (2x).

2. Sample binding and washing:

To bind the proteins from the sample to the ZipTip, it was pipetted in and out ten times. Weakly bond molecules were flushed away by soaking the ZipTip with washing solution and dispensing it to a waste container (2x).

3. Elution:

The remaining sample was eluted by soaking and dispensing elution solution three times without introducing air.

Cation exchange chromatography: The water soluble matrix was obtained by demineralization with 6% acetic acid as described in section 3.1.4. The soluble matrix in acetic acid was centrifuged at 15000 rpm for 15 min at 4° C (Sorvall SS 34, Thermo Fisher, Waltham, USA). Then, the supernatant was filtered with a 0.22 μ m membrane filter. The resulting solution was dialyzed against 20 mM Na-citrate buffer with 0.02% NaN₃ at pH 4.8. Cation - ion exchange chromatography was performed using a carboxy methyl functionalized - sepharose column (HiTrap-CM sepharose fast flow, Amersham Biosciences, Piscataway, USA) and a LC system (Gradifrac, Amersham Biosciences, Piscataway, USA). Solvent A consisted of 20 mM Na-citrate buffer with 0.02% NaN₃ at pH 4.8; solvent B consisted of 20 mM Na-citrate buffer with 0.02% NaN₃ at pH 4.8 and 1 M NaCl. All solutions were degassed before use. The ion exchange chromatography was performed at 4° C. After sample application (250 ml) to the column and flushing of the column for 15 min with 100% A at 5 ml/min, a linear gradient from 100% A to 100% B in 10 min with a flow rate of 5 ml/min was used. All fractions with a significant absorption at 280 nm were pooled and used for amino acid analysis. The ion exchange chromatography was kindly performed by Meike Gummich, Biophysics Institute, University of Bremen.

BTI Treatment of Proteins

A protein sample (typically 100 μ g) in 2 ml solution of 5 M guanidine hydrochloride and 0.01 M trifluoroacetic acid was mixed with 2 ml of freshly prepared [bis(trifluoroacetoxy)-iodo]benzene (BTI) in dimethylformamide (36 mg/ml). The mixture was incubated in the dark for 4 h at 60° C. After incubation, the solution was dialyzed (MWCO 3500) against water. The BTI treated and denatured protein was visible as a white precipitate. It was extracted by adding 1 ml of n-butyl acetate to the dialysis membrane and shaking of the dialysis tube. After ten minutes the upper phase, which contained n-butyl acetate and proteins, was drawn off with a pipette. The extraction step was repeated three times. The pooled BTI treated proteins in n-butyl acetate were dried by rotary evaporation before hydrolysis.

Protein Hydrolysis

Proteins were fragmented in amino acids by liquid phase hydrolysis. The proteins bovine serum albumin (BSA) (A9418, Sigma Aldrich, Saint Louis, USA), lysozyme (L6876, Sigma Aldrich, Saint Louis, USA) and the soluble organic matrix prepared as described above in this section were used. If protein samples were not available in dry form, a microcentrifuge tube (2 ml) was filled with a solution containing 0.1 mg - 2 mg protein and dried by rotary evaporation until complete dryness was achieved.

A hydrolysis solution of 1.5 ml of 6 M HCl with 0.02% Phenol was added to the resulting protein pellet. The solution was incubated in an oven at 110° C for 24 h. The microcentrifuge tube was tightly wrapped with aluminum foil to prevent bursting of the cover caused by

the heat. After this, the acid was removed by rotary evaporation until complete dryness was achieved. For determination of cysteine, in some samples 0.20% (w/v) sodium azide (NaN_3) was added to the hydrolysis solution (warning: risk of explosion, see [Manneberg et al., 1995]) to react cystine to cysteic acid.

Phenylisothiocyanate (PITC) Derivatization of Amino Acids

Dried amino acids from protein hydrolysis or amino acid standard mixtures were redissolved with 5 μl 50% water / ethanol. 10 μl coupling buffer was added and the tube was mixed with a vortex shaker. The coupling buffer consisted of 1 ml PITC, 2 ml TEA, 1.11 ml water and 7 ml Ethanol. It was prepared weekly and stored in darkness at 4° C. After an incubation period of 10 min at room temperature the coupling buffer was removed by rotary evaporation. Until further HPLC analysis, dry PITC derivatized samples were stored at -18° C and stable for at least several weeks [Heinrikson and Meredith, 1984].

Calibration and Peak Identification

The calibration was performed using an amino acid standard (Amino acid standard A 2908, Sigma Aldrich, Saint Louis, USA) in the range of 0.25 - 4 nmol. Identification of unknown peaks was performed by comparing the order of elution with similar separations in the literature (e.g. [Janssen et al., 1986]) and by adding isolated PTC-amino acids to some calibration runs⁶. The standard solutions were PITC derivatized and separated by HPLC using the protocols described in this section. The calibration was performed by plotting the peak area A against the amount of amino acid n and fitting of the data with a linear function. The slope of the fit $\Delta n/\Delta A$ served to determine unknown amounts of amino acids, e.g., from hydrolyzed samples by multiplication with the measured peak area A .

HPLC Separation of Phenylthiocarbamyl (PTC) Amino - Acids

The HPLC separation of the PTC - amino acids was performed according to R. Ebert [Ebert, 1986]. A buffer system of two solvents A and B was used. Solvent A consisted of 50 mM Na - acetate buffer, with 2.75 ml/l TEA. The pH-value was adjusted to exactly 6.40 with phosphoric acid. Solvent A was filtered with a 0.22 μm filter before further use. Solvent B consisted of 50% solution A (v/v), 40% acetonitrile (v/v) and 10% methanol (v/v). It was not further filtered, because solvent B consisted of the filtered solvent A and two HPLC-grade solutions. PTC amino acids were dissolved in 0.2 - 2 ml solvent A, depending on the desired concentration. Before each HPLC run, the system was equilibrated for ten minutes with 95% solvent A and 5% solvent B at 1 ml/min. For greatest accuracy, the 100 μl injector loop was always filled completely. A HPLC system (Model 600, Waters, Eschborn, Germany) equipped with a 4.6 x 150 mm Spherisorb ODS-2 C-18 3 μm particle diameter,

⁶For example, by adding PTC-methionine to the standard, the pronounced peak can then be identified as PTC-methionine.

Table 3.2.: Gradient program for fast separation of PTC-amino acids according to R. Ebert [Ebert, 1986].

Time [min]	%A	%B	Flow [ml/min]
0.0	95	5	1.0
4.5	80	20	1.0
6.5	80	20	1.0
10.5	50	50	1.0
15.5	50	50	1.0
16.0	0	100	1.0
17.2	0	100	1.0
17.5	0	100	1.5
21.5	0	100	1.5
22.0	95	5	1.5
26.0	95	5	1.5
26.1	95	5	1.0

150 Å pore width column (MZ-Analysentechnik, Mainz, Germany) was used. The column was protected with an 0.5 µm inlet filter (Rheodyne 7335, IDEX HS, Oak Harbor, USA). The gradient was used as shown in table 3.2. The detection of the PTC - amino acids was performed at 254 nm with an UV - absorbance detector (Model 2487, Waters, Eschborn, Germany). Peak areas were determined with the software of the HPLC system (Empower, Waters, Eschborn, Germany).

4

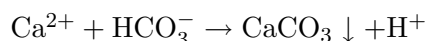
Results and Discussion

4.1. Double-Diffusion Crystallization under Constant Conditions

4.1.1. Introduction

The influence of the interlamellar organic matrix of nacre from *Haliotis laevis* on CaCO_3 nucleation and growth was investigated. For this purpose, a new crystallization method to crystallize slowly with constant pH-value, supersaturation and ionic strength was developed.

This was important, since surface properties of most biogenic surfaces are pH-value dependent. Furthermore, even without biogenic or ionic impurities, CaCO_3 nucleation and growth is a very delicate process, depending on many variables such as temperature, stirring-speed, supersaturation, ionic strength and pH-value (compare e.g., [Wang et al., 1999], [Ogino et al., 1987], [Söhnle and Mullin, 1982], [Franke and Mersmann, 1995]). The last three parameters are difficult to control. In most crystallization methods, supersaturation and ionic strength will decrease with time due to the consumption of the crystallizing ions. Additionally, the pH-value changes, because of the chemistry of CaCO_3 precipitation:



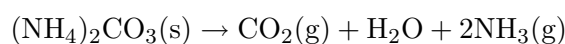
To show the necessity for the development of a new crystallization method in greater detail, two widely used methods to investigate the influence of biopolymers on CaCO_3 crystallization - the ammonium-carbonate method and the conventional double-diffusion method - are discussed at the beginning of this section. The development of the new method for the slow crystallization of CaCO_3 on the interlamellar matrix under defined conditions follows.

The influence of the interlamellar matrix and other polymeric surfaces on CaCO_3 nucleation and growth was studied with the newly developed method. This section concludes with the presentation and discussion of these investigations. Practical details of these investigations can be found in the materials and methods, section 3.4.

4.1.2. Ammonium-Carbonate Method

The ammonium-carbonate gas diffusion method [Addadi and Weiner, 1985] is a simple and frequently used method to investigate the influence of proteins (or more generally: additives) on CaCO_3 crystallization.

A drawing of the experimental setup is shown in figure 4.1 (a). Ammonium-carbonate ($(\text{NH}_4)_2\text{CO}_3$) powder is placed in a sealed desiccator. Small vessels, containing solutions with typically 7.5 mM CaCl_2 and the proteins to investigate, are also placed in the desiccator and covered with pierced aluminium foil to slow down gas diffusion. The ammonium-carbonate powder decomposes at room temperature and ambient pressure to carbon dioxide, water and ammonia, according to the following reaction:



Gaseous carbon dioxide and ammonia will diffuse into the vessels containing the CaCl_2 solution. Because ammonia is a base, it increases the pH-value of the solution. Hence, most of the dissolved CO_2 will exist in the carbonate form CO_3^{2-} , creating a supersaturated CaCO_3 solution. CaCO_3 precipitation will occur, possibly altered by present proteins. After one or two days, the morphology of the precipitated crystals is investigated by SEM and compared with crystals obtained without additives (typically rhombohedral calcite).

The major drawback of the ammonium-carbonate method is the high pH-value during crystallization. Figure 4.1 (b) shows a measurement of the pH-value course during an ammonium-carbonate gas diffusion experiment. Due to the ammonia uptake, the pH-value rises to values of about 9.8. A pH-value of 9.8 is much higher than any physiological pH-value. Hence, investigated biomineralizing proteins may have different properties, e.g., surface charges. Furthermore, due to the high pH-value and the constant uptake of CO_2 , the crystallization is presumably very rapid at the initial phases¹.

Because of these disadvantages, the method was considered unsuitable for investigating the influence of the interlamellar matrix on CaCO_3 nucleation and growth.

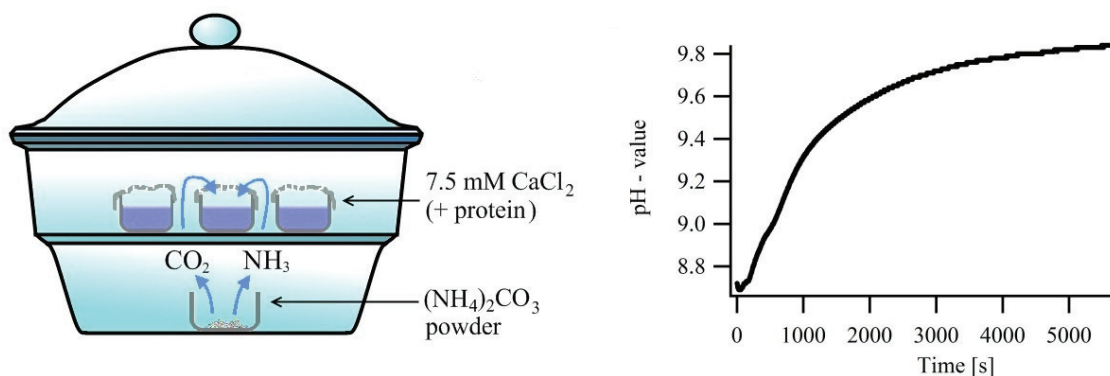


Figure 4.1.: The ammonium-carbonate gas diffusion method to precipitate CaCO_3 under the influence of proteins. (a) Experimental setup. Ammonium-carbonate powder decomposes to CO_2 and NH_3 in a sealed desiccator. Both gases will diffuse into vessels containing a solution of CaCl_2 and proteins (e.g. extracted from nacre). (b) Time course of the pH-value, measured for an ammonium-carbonate gas diffusion experiment. Due to the ammonia uptake, the pH-value rises to levels which cause experimental problems: a non physiological environment for the investigated biomolecules and a too rapid crystallization.

4.1.3. Conventional Double-Diffusion

A different method, more suitable to slowly crystallize on surfaces, is double-diffusion crystallization. In this method, two reservoirs contain the solutions necessary to create a supersaturated CaCO_3 solution. The reservoirs are separated by an ion permeable membrane, so that the solutions will diffuse through the membrane and crystallization can occur (compare figure 4.2). Typical conditions are 10 mM CaCl_2 in one reservoir and 10 mM NaHCO_3 in the other [Falini et al., 2002]. Additives such as MgCl_2 or biomineralizing proteins may be present in the solutions. Compared to the ammonium-carbonate method, double-diffusion

¹Because at high pH-values, all dissolved CO_2 will exist in the form CO_3^{2-} , creating a high supersaturation.

crystallization has several advantages, when crystallization on, and influenced by, surfaces is investigated. The crystallization is slow, allowing the investigated surfaces to influence nucleation and growth maximally. Furthermore, the risk of collecting crystals precipitated from the solution (which may then be interpreted wrongly as nucleated on the surface) is lower than in the ammonium-carbonate method, because of the lower supersaturation² and of the vertical installation of the investigated membrane.

However, the drawback of conventional double-diffusion setups is that the crystallization conditions are not constant. The carbonate solution diffuses in the calcium-chloride solution and vice versa. Furthermore, the pH-value locally drops due to CaCO_3 precipitation and mixing of the two solutions (see section 4.3). Attempts to keep the pH-value constant by computer controlled addition of NaOH [Becker et al., 2003] cannot circumvent the problem of inconsistent carbonate and calcium concentrations.

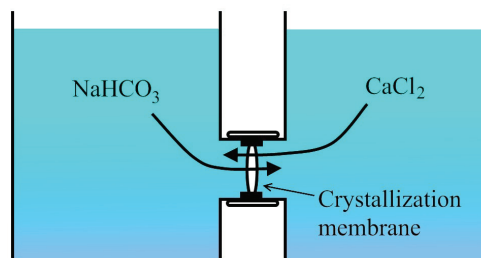


Figure 4.2.: In conventional double-diffusion systems an ion-permeable membrane separates two reservoirs containing the calcium and carbonate ions. They mix by diffusion and can crystallize at the membrane.

4.1.4. Development of a Crystallization Device for Controlled Crystallization on a Polymeric Surface

To avoid the problems of the crystallization methods described above³, a new crystallization method was developed. The main aspects, considered for the design of the method, were:

- Crystallization of CaCO_3 on an ion permeable, polymeric surface.
- Slow and steady crystallization, that allows the surface to exert a maximal influence on crystal formation.
- Crystallization under constant and physiological pH-value and constant concentrations.
- Avoidance of the collection of precipitated crystals nucleated from solution.

The first version of the newly developed crystallization device is shown in figure 4.3 (a). The design was derived from conventional double-diffusion systems and a crystallization system developed at the University of Duisburg-Essen [Becker and Epple, 2005]. The device was built from polycarbonate and consists of two halves, which was joined with screws to form

²In particular, the upper limit of the supersaturation can be controlled better, compared to the ammonium-carbonate method.

³Also other methods for CaCO_3 crystallization were not suitable to crystallize on the interlamellar matrix: for example methods where calcium and carbonate salts were mixed directly before passing a reaction chamber [Volkmer et al., 2005]. The pH-value and ionic composition will change after mixing and crystal nuclei may form, which could be collected by the investigated polymeric surface and wrongly interpreted as nucleated on the surface.

a crystallization box. The inside held a thin, disk shaped and perforated box in which the investigated polymeric surface was embedded. Calcium and carbonate salt solutions passed through the box, constantly renewed by a peristaltic pump. The solutions mixed by diffusion and crystallized on the polymeric surface, as in conventional double-diffusion systems, but due to the constant renewal of the solutions, the pH-value and concentrations remained constant.

Initial investigations of the system showed the potential for improvements:

- 1.) Because the flow of solutions is relatively slow (typically 0.5 ml/min) and laminar, the radial distribution of ions outside the flow path occurs mainly by diffusion. Dye tests showed that the lateral motion of ions would presumably be too slow to achieve constant conditions, as shown in figure 4.3 (b).
- 2.) Embedding of the investigated surface inside a perforated box was not optimal, as this increased the diffusion path.

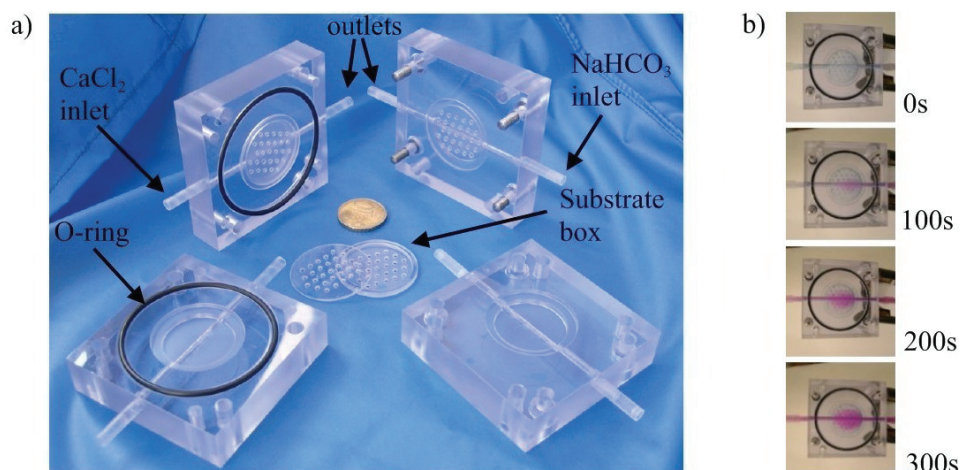


Figure 4.3.: (a) First version of the double-diffusion crystallization system. Two boxes consisting of two halves and a disk-shaped substrate box are shown. The ion permeable substrate surface (e.g., the interlamellar matrix of nacre) was embedded in a very thin and perforated substrate box. The solutions, containing carbonate and calcium ions, were constantly pumped and mixed by diffusion through the membrane. For comparison, a 10 cent coin with a diameter of 19.75 mm is shown. (b) Investigation of the radial distribution of a dye in the crystallization box by transporting the dye through the system. The radial distribution was too slow for constant conditions.

The final design of the crystallization box is shown in figure 4.4. Detailed engineering drawings can be found in appendix A.3. Solutions containing calcium or carbonate salts were pumped through the box, separated by the investigated surface where they mixed by diffusion. To improve the radial distribution of solutions, the inside of the box was designed narrowly (14 mm diameter) and two parallel flow channels per side were used. The inside

was built such that investigated surfaces could be mounted directly inside the box when necessary, with the help of one or two neoprene spacer rings. This had the advantage of a smaller diffusion path between the two sides of the box.

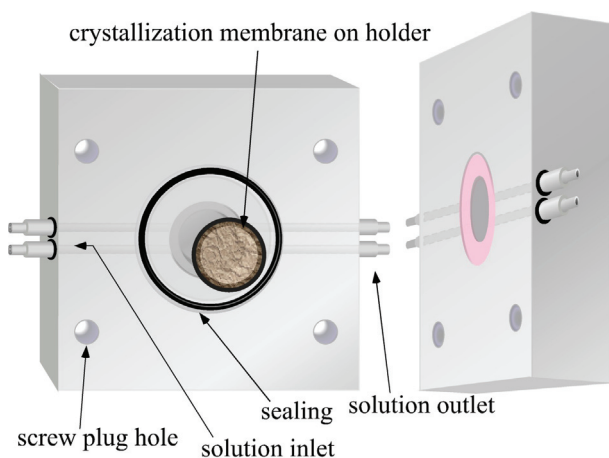


Figure 4.4.: Double-diffusion crystallization box (opened). An ion permeable membrane separates the constantly pumped carbonate and calcium ion containing solutions, which mix by diffusion through the membrane. Two flow channels per side were used, to obtain a better radial distribution of ions.

4.1.5. Results and Discussion

Artificial Polymeric Surfaces

In figure 4.5, representative SEM images of crystallization experiments on the polymeric substrates cellulose, carboxymethylated cellulose⁴, chitin and carboxymethylated chitin are shown. The most frequently observed polymorphs were calcite (rhombs), aragonite (needle-balls) and in a few cases vaterite (florets). Comparable results were also obtained by crystallization on chitosan. The crystal morphology was identical to precipitated crystals from solutions and no influence of the surface on the crystal morphology could be observed. This is in accordance with similar experiments [Falini et al., 2002], [Becker and Epple, 2005], indicating that on most surfaces and without dissolved additives, usually only calcite, aragonite and, by rapid crystallization, vaterite crystallize.

Interlamellar Matrix

In crystallization experiments using the interlamellar matrix, crystals with a greatly altered habit were obtained. The figures 4.6 (a-f) and 4.7 (a-d) show a compilation of typical results⁵.

⁴The prominent hydroxyl-group at position 6 of the glucose ring was functionalized with a carboxymethyl-group in order to create a negatively charged surface.

⁵Additionally, on almost all samples, unspecific crystallization was found. For example, in figure 4.6 (a), the left half of the SEM image is covered with calcite rhomboeda and a few vaterite florets.

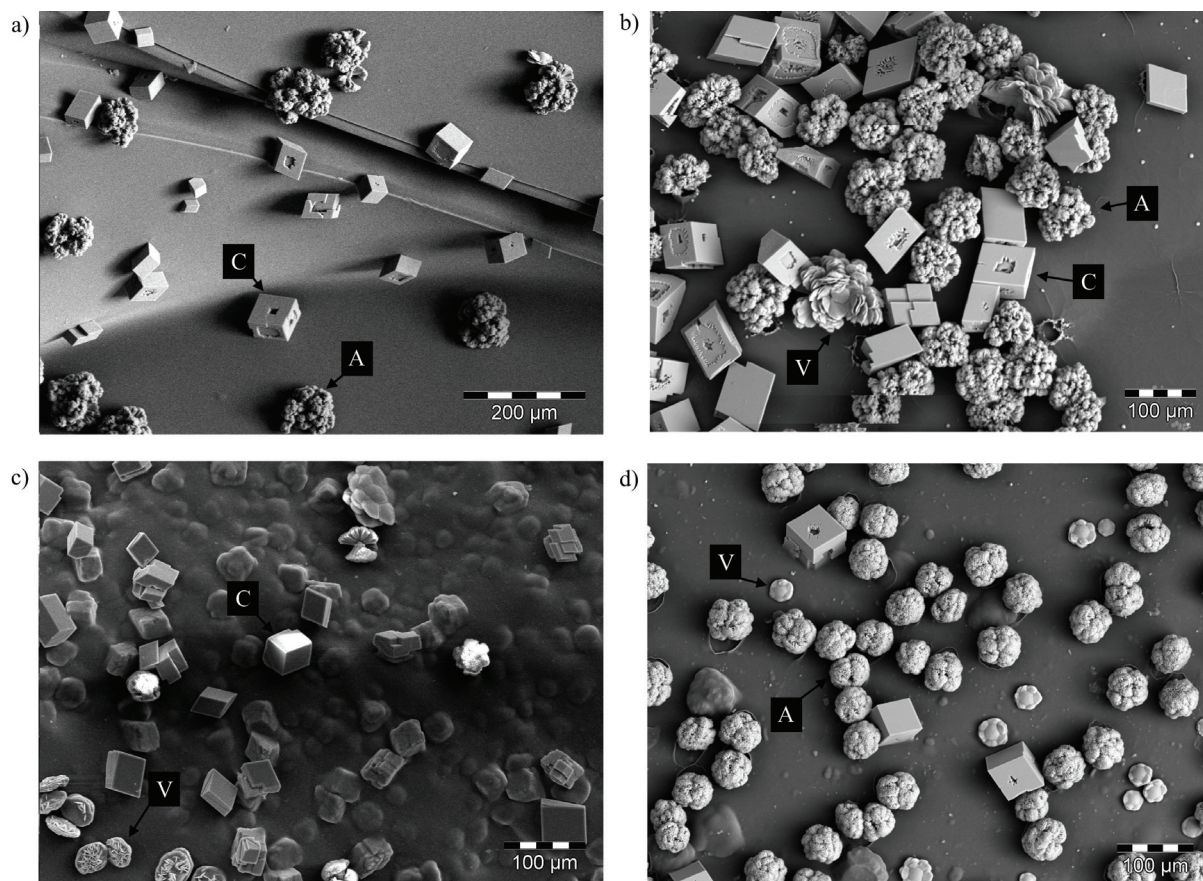


Figure 4.5.: Images of several artificial polymeric surfaces after CaCO_3 crystallization by double-diffusion under constant conditions (20 mM NaHCO_3 , pH-value 8.4 and 20 mM CaCl_2). (a) Cellulose, (b) carboxymethylated cellulose, (c) chitin, (d) carboxymethylated chitin. Only crystals with typical polymorph morphologies were obtained. The following crystals are labeled in the images: calcite (C, rhombs), aragonite (A, needleballs) and vaterite (V, florets).

Crystals grown on the surface of the interlamellar matrix were mostly flat and roundish or roughly polygonal. The boundary of the crystals was often congruent with the outline of the underlying honeycomb-like structure (intertabular matrix) of one or several platelet imprints. This indicates that preferred nucleation occurs on the surface of the interlamellar matrix between the honeycomb-like intertabular matrix.

Often large assemblies of up to 100-200 μm lateral dimension were observed, seemingly composed of subunits corresponding to the inside of the honeycomb-like structure (compare figure 4.6 (c)). The subunits, which were visible in many cases, had a typical diameter of 10-15 μm . The assemblies were mostly isolated and in several cases roughly circular (compare figure 4.6 (d)). This indicates that they originate from an isolated nucleation, which laterally expanded.

In several cases, the mineralization was clearly located inside the interlamellar matrix, shown by the bending of matrix sheets by the crystals (arrow in figure 4.6 (c)).

In contrast, in some of the experiments the honeycomb-like structure was mineralized

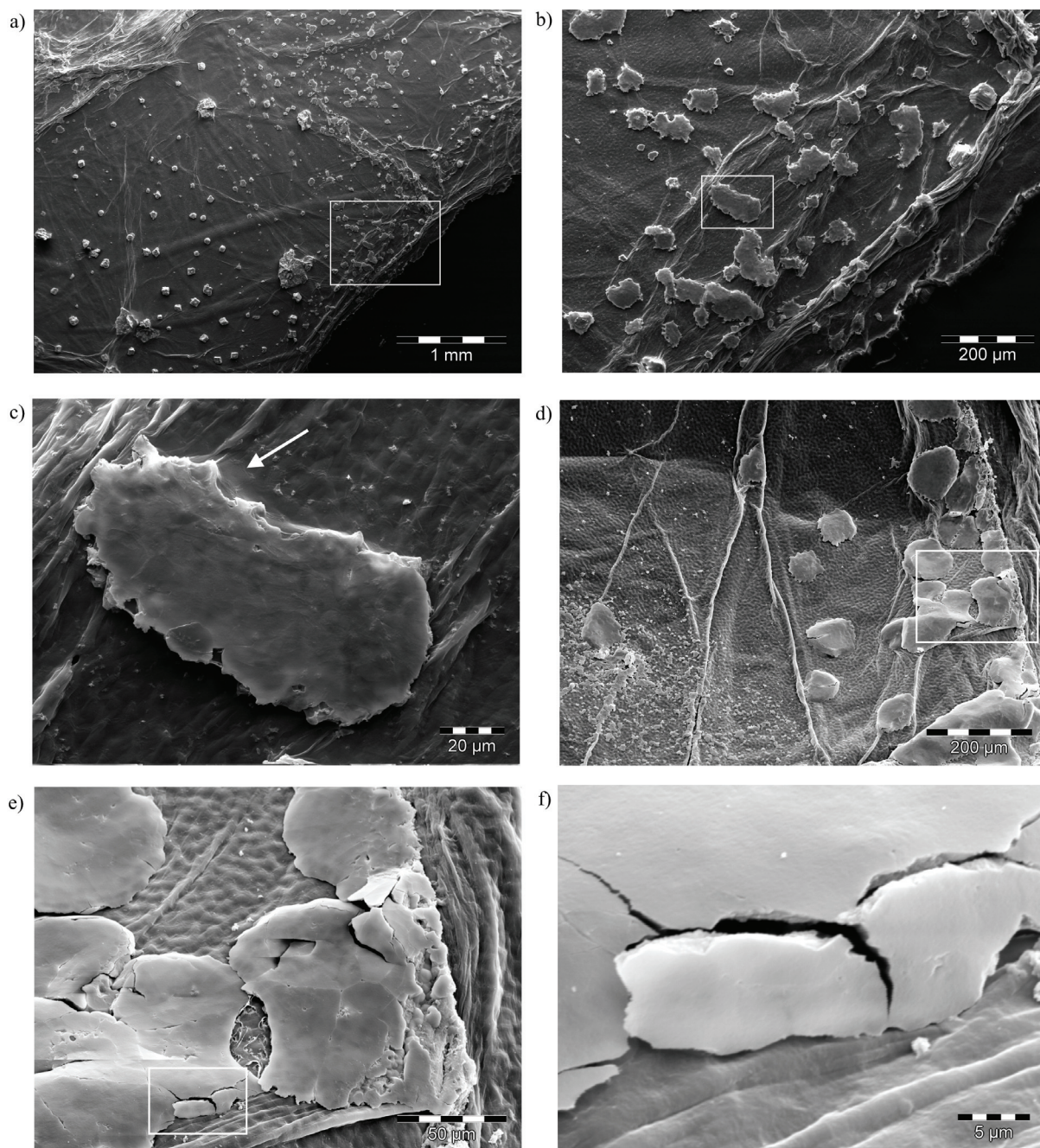


Figure 4.6.: Typical SEM images of the interlamellar matrix of nacre after CaCO_3 crystallization by double-diffusion under constant conditions. The flat crystals grown on the surface of the insoluble matrix show a high similarity to tablets of growing nacre. Images (a)-(c) and (d)-(f) are successive magnifications of the same location. On the lower left of image (a), unspecific crystallization, calcite rhombs and vaterite florets, are visible. In image (c), the bending of the interlamellar matrix sheets by sub-surface crystals can be seen (arrow), indicating that crystal growth inside the matrix occurred. Crystallization conditions of all images were: 20 mM NaHCO_3 , pH-value 8.4 and 20 mM CaCl_2 .

(see arrow in figure 4.7 (d)), whereas the inside of the honeycomb-like structure was not mineralized or less mineralized. Two possibilities are suggested. Either the intertabular matrix holds back high amounts of nucleating proteins, that were pushed away during the

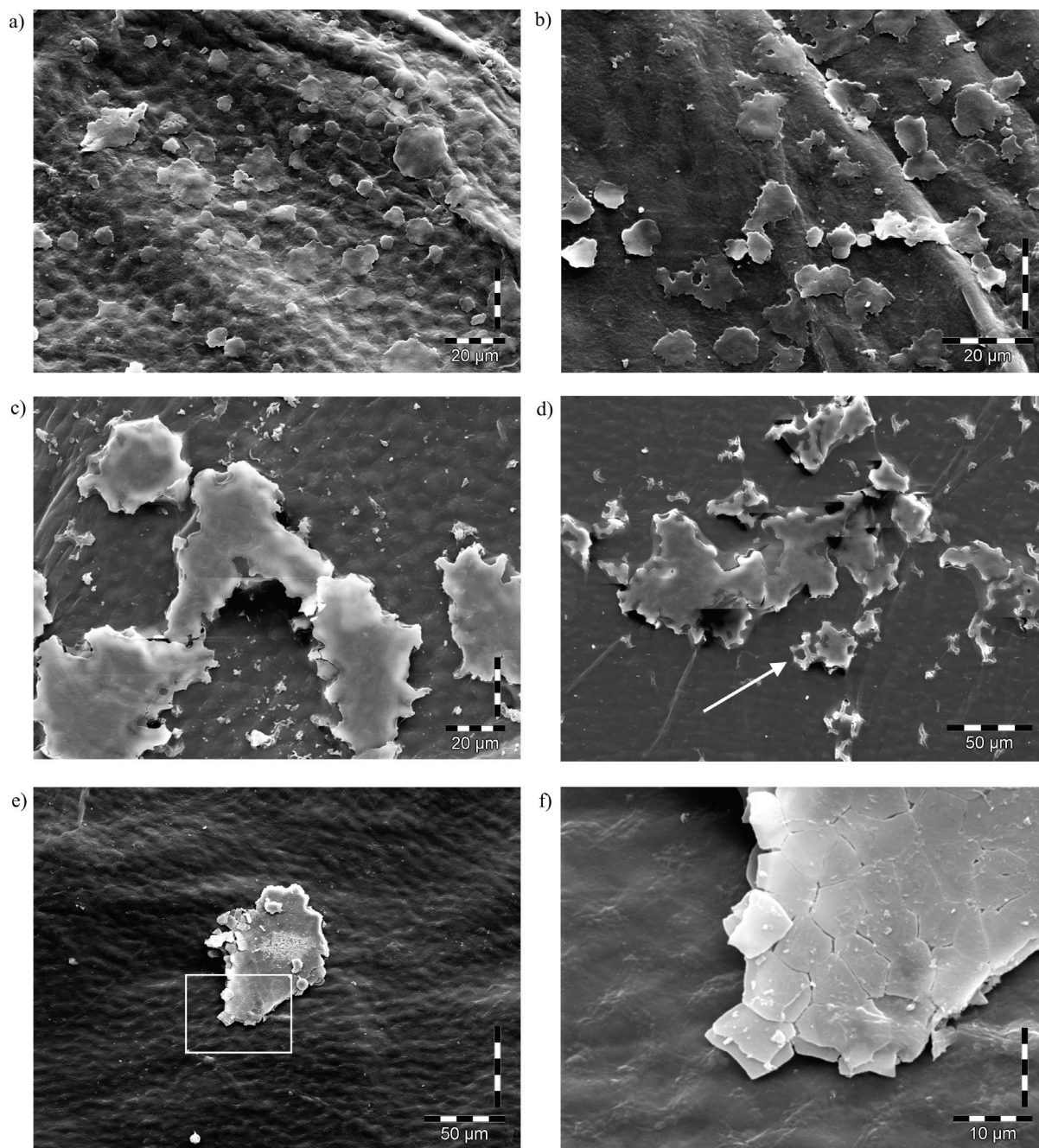


Figure 4.7.: (a)-(d): More typical SEM images of the interlamellar matrix of nacre after CaCO_3 crystallization by double-diffusion under constant conditions. The flat crystals grown on the surface of the insoluble matrix show a high similarity to tablets of growing nacre. In image (d), an example of the mineralization of the honeycomb-like structure (intertabular matrix) is shown (arrow), which was observed often. Also, the bending of matrix sheets by underlying crystals can be seen in figure (d). Images (e) and (f) show a singular result, where two layered crystal platelets were obtained. Here, the morphology was practically identical to nacre platelets. Crystallization conditions of all images were: 20 mM NaHCO_3 , pH-value 8.4 and 20 mM CaCl_2 .

growth of the original material, or the structures are artifacts, produced by flaking off of charged crystals under the influence of the electron beam.

Investigation of the mineralized interlamellar matrix by X-ray diffraction (see figure 4.8) resulted in two aragonite peaks and the main calcite peak at $2\theta = 29.4^\circ$. Since nearly all of the samples also contained locations with unspecific crystallization, it was necessary to determine the polymorph of the flat crystal sheets. This was done by performing an aragonite sensitive stain on a sample, previously investigated by XRD. Hereby, it was shown, that the flat crystal sheets were indeed aragonite. A crystalline orientation of the crystal sheets seems likely, as the XRD peaks differ strongly from an aragonite powder diffractogram (compare figure 4.10 (e)).

The growth of flat sheets of (presumably oriented) aragonite indicates that the interlamellar matrix of nacre is a key factor for the growth of nacre. It is interesting that neither on chitin nor on the negatively charged carboxymethylated polymers, similar growth modifications were observed. It must be added, that additional double diffusion experiments in the presence of magnesium (up to 50 mM) were performed, since this ion favors aragonite growth [Kitano et al., 1976] and is present in the extrapallial fluid [Crenshaw, 1972]. However, only aragonite with the typical geological appearance was obtained on the interlamellar matrix (not shown).

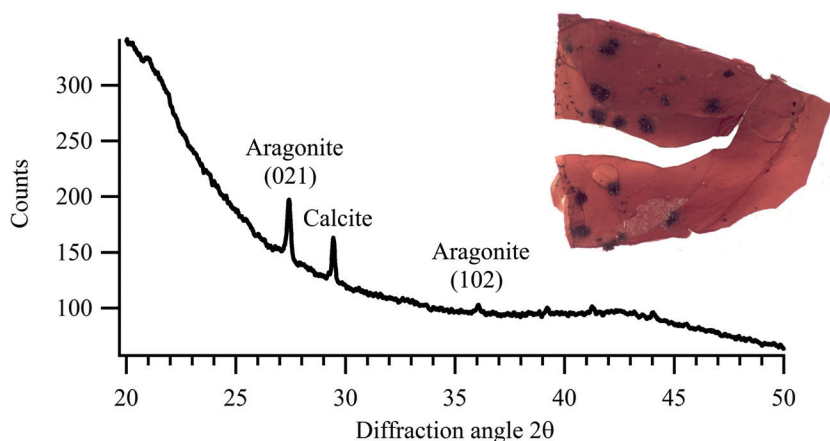


Figure 4.8.: X-ray diffraction of the interlamellar matrix after CaCO_3 crystallization by double-diffusion under constant conditions revealed that aragonite and calcite were present. The inset (upper right) shows a photograph of the same interlamellar matrix sample after performing Feigl's aragonite sensitive stain. The typical assemblies of flat crystals stained positive (black), indicating that the flat crystal sheets are the source of the aragonite peak and the calcite peak is presumably derived from unspecific crystallization. The image was captured by Jutta Bonnet, Institute for Solid State Physics, University of Bremen. The edge length is approximately 7 mm. The image was contrast enhanced, for a clearer display.

In some cases, specimens with macroscopic, space-filling mineralization inside the membrane with the characteristic iridescent appearance were obtained (4.10 (a-d)). SEM investigations on these samples showed that the mineralization morphology was nearly identical to that of natural nacre, with sheets of platelets formed inside the insoluble matrix. In figure 4.10 (a), a region is displayed where the insoluble matrix surface cracked during preparation,

uncovering sheets of platelets under the surface. In figure 4.10 (e), a XRD measurement of a space-filled sample compared with XRD on natural nacre and nacre powder (both *Haliotis laevis*) is shown. All samples showed aragonite peaks. The space-filled sample and the natural nacre have very similar peak intensities. Compared to the powder sample the intensities are different, with some peaks completely suppressed, indicating preferred crystal orientation. In the remineralized interlamellar matrix at $2\theta = 29.4^\circ$ also the main calcite peak was visible, showing that not only aragonite was nucleated. It is unclear why space-filling crystallization was only obtained sometimes, and it is unknown what the conditions for a safe reproduction are.

Interlamellar Matrix after Deproteination

The interlamellar matrix was treated with proteinase-K. SEM images after a mineralization experiment are shown in figure (figure 4.9).

Two new features of the deproteinated surfaces were remarkable: 1.) In the SEM images of these surfaces, the complete degradation of the honeycomb-like structure could be observed. 2.) The surface differed noticeably from untreated samples by the appearance of small pits. The distance between the pits was roughly 5-10 μm , resembling the size of the aragonite platelets in nacre. A similar structure was previously reported after deproteination of nacre cleavage planes [Arnoldi, 2001]. This indicates that the pits are a distinct structure underlying each aragonite platelet.

By mineralization with the double-diffusion setup, small, flat crystal platelets were obtained. Again, the obtained crystals were of highly unusual morphology, when compared to the experiments with artificial polymers. Interestingly, no large assemblies of platelets were

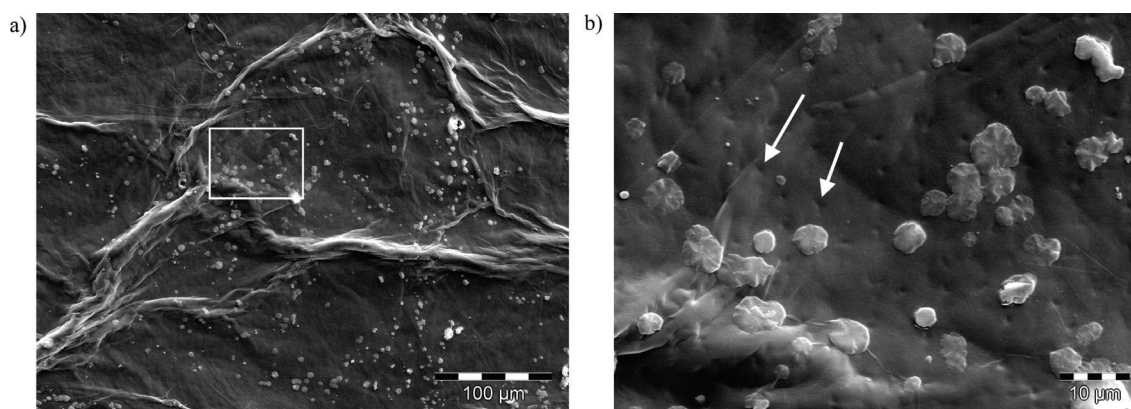


Figure 4.9.: SEM images of the interlamellar matrix of nacre, deproteinated with proteinase-K after CaCO_3 crystallization by double-diffusion under constant conditions (20 mM NaHCO_3 , pH-value 8.4 and 20 mM CaCl_2). Image (b) is a magnification of image (a). In the magnification, the absence of the honeycomb like structure (intertabular matrix) and the occurrence of small pits on the matrix surface can be observed (arrows). The crystals on the deproteinated samples were more flattened, smaller and had a lower tendency to form large assemblies, when compared to the native interlamellar matrix.

observed, which was a typical feature for the crystal growth on the unmodified interlamellar matrix.

A hypothetical explanation for this is that a central nucleating region was seemingly unaffected by the protease-K treatment. However, the regions necessary to favor lateral crystal growth might have been degraded, as the crystals did not exceed a few μm . Although speculative, this would be in accordance with findings on nacre of the bivalve *Atrina rigida*, in which a heterogeneous structure underlying each aragonite platelet with a central region of acidic proteins was reported [Nudelman et al., 2006]. This region might be resistant to proteinase-K treatment, which cleaves behind aromatic and aliphatic amino acids [Ebeling et al., 1974].

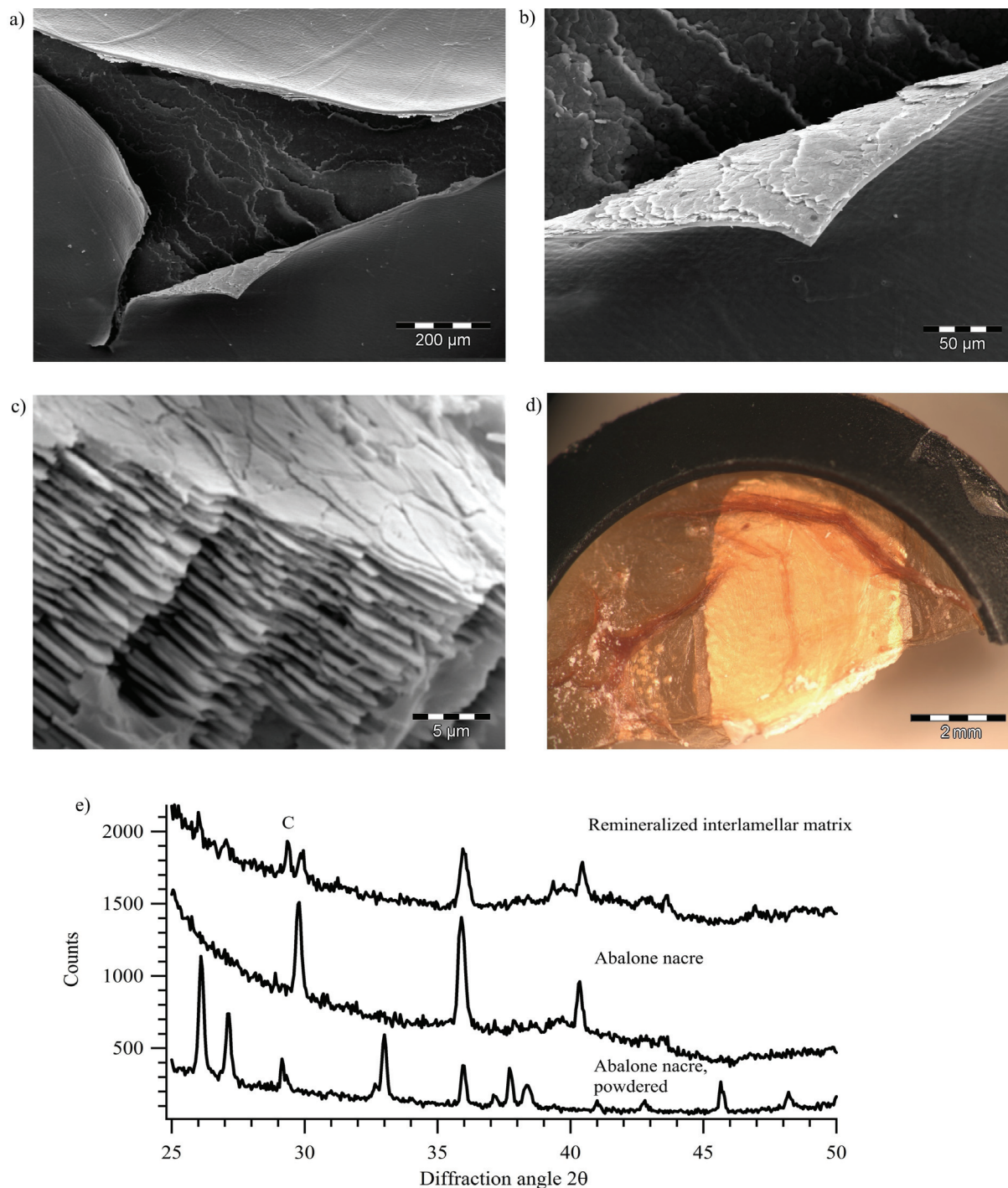


Figure 4.10.: In some cases, large macroscopic assemblies strongly resembling natural nacre were obtained after double-diffusion crystallization. (a), (b) Attached sheets of platelets inside the insoluble matrix and no mineral on the surface in a region where the matrix cracked during preparation. (c) Fracture region, showing the stacking of platelets identical to natural nacre. (d) Photograph showing the macroscopic assembly inside the interlamellar matrix, which had an iridescent appearance. (e) XRD of powdered nacre, native nacre (shifted) and the mineralized matrix (shifted) as shown above. Powdered nacre shows peaks identical to aragonite powder. The XRD of native nacre and the remineralized matrix was taken at 38° (surface, beam). In both cases, compared to the nacre powder, most of the peaks are missing and the samples show a strong dependency (not shown) on the specimen orientation related to the X-ray beam due to the high crystal orientation. In the remineralized matrix, a calcite peak was present at $2\theta = 29.4^\circ$ (labeled by a C over the peak). Crystallization conditions were: 20 mM NaHCO_3 , pH-value 8.4 and 20 mM CaCl_2 .

4.2. Surface Free Energy Determination

4.2.1. Introduction

For a better characterization of the interlamellar matrix, the surface was investigated with contact angle measurements. The previously only qualitatively observed hydrophobic behavior of the matrix should be quantified. Furthermore, the surface free energy, as well as dispersive and polar contributions to the surface free energy should be determined. The surface free energies were obtained by measuring contact angles of a series of test liquids on the surface. Experimental details of the measurements and details of the evaluation method of Owens and Wendt, which was used here, are described in section 3.5.

First, the results for the surface free energy measurements will be described and discussed. The section concludes with the brief description of the hypothesis that particular surface free energy properties of the interlamellar matrix are responsible for the growth of flat crystals.

4.2.2. Results and Discussion

In order to obtain equilibrium contact angles as described by Young's equation (equation 3.5), it is a prerequisite that the surface has to be dry. For complex polymeric materials like the interlamellar matrix, this is often problematic, because they can swell due to liquid absorption. To make matters worse, the structure of the interlamellar matrix is such, that it is especially permeable to the extrapallial fluid, as this is a requirement for nacre growth. Hence, the stability of contact angles had to be investigated before further measurements could be performed: Figure 4.11 shows the decrease of contact angles (water droplets on the interlamellar matrix) with time due to swelling and, to a lesser degree, evaporation⁶. During the first 50 s the decrease was roughly linear with a slope of $\approx -0.3^\circ/\text{s}$, slowing down with increasing water content of the interlamellar matrix. As a result, all further imaging of contact angles was performed as quickly as possible after the droplet was sessile.

Table 4.1.: Average contact angles (in degrees) of water on the three investigated biopolymer surfaces and as a reference on paraffin wax, which is highly hydrophobic.

Surface	Average contact angle and standard deviation
Paraffin wax	109.3 \pm 4.4
Interlamellar matrix	79.3 \pm 4.1
Interlamellar matrix, deproteinated	36.7 \pm 6.0
Chitin film	49.5 \pm 2.2

The most direct way to characterize surfaces with contact angles is to compare the contact angles of water. Table 4.1 lists the average contact angles of water on the investigated

⁶A contact angle decrease of $\approx -0.06^\circ/\text{s}$ due to evaporation was measured on a solid surface by Malte Launspach, Biophysics Institute, University of Bremen. The decrease of volume retracts the droplet. Retracting contact angles are always lower than advancing or the initial sessile contact angles.

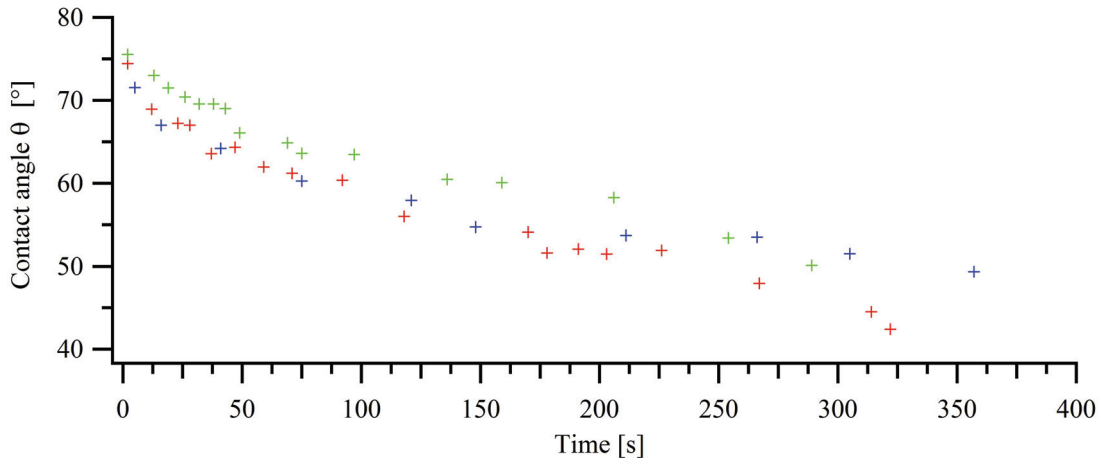


Figure 4.11.: The contact angle (water on the interlamellar matrix) depends on the time elapsed since liquid application. Three different series of measurements on the matrix are shown (red, green, blue). The initially dry matrix swells due to water uptake. The higher water content leads to lower contact angles with water. As a result: all further contact angles were captured as quickly as possible after droplet application.

surfaces. The contact angle on the interlamellar matrix is 79.3° , which can be described as slightly hydrophobic. After deproteination with proteinase-K the properties of the interlamellar matrix changed dramatically towards a contact angle of 36.7° .

The evaluation according to Owens and Wendt was validated using paraffin wax and a good linear relationship could be obtained in this case (Pearsons coefficient of regression $R^2 = 0.88$). The polar surface free energy was almost zero, as expected for paraffin wax - a mixture of completely apolar alkanes. The determined total surface free energy of 19.2 mN/m was in the range of reference values for paraffin wax [Krüss GmbH, 2008]. Figure 4.12 shows the plot according to Owens and Wendt, including a linear fit for all four substrates. Also in the case of the biopolymer surfaces, the fit was satisfying⁷. Table 4.2 lists all determined surface free energy values.

Table 4.2.: Polar γ^p , dispersive γ^d and total surface free energy γ of the investigated surfaces. Values are in $[\text{mN/m}]$.

Surface	γ	γ^p	γ^d
Paraffin wax	19.2	0.3	18.9
Interlamellar matrix	47.2	2.8	44.4
Interlamellar matrix, deproteinated	58.4	49.0	9.4
Chitin film	49.8	30.9	18.9

The surface free energy of the interlamellar matrix is almost entirely obtained from apolar

⁷Here the data points for the highly viscous glycerine and glycol had the highest deviation from the linear relation presumably due to the longer time taken to achieve equilibrium contact angle. Pearsons coefficients of regression for the linear fit: interlamellar matrix $R^2 = 0.73$, interlamellar matrix, deproteinated $R^2 = 0.95$, chitin $R^2 = 0.96$.

interactions as the dispersive component is very dominant. This corresponds to the slightly hydrophobic properties of the surface. The absolute value of 47.2 mN/m of the surface free energy is relatively high, when compared with other polymeric surfaces [Kaelble, 1970]. After enzymatic cleavage of proteins, the properties of the interlamellar matrix reverse: the polar surface free energy component becomes dominant and the dispersive component very low. In the measurements, chitin showed a very similar behavior to the deproteinated interlamellar matrix. These results agree with the structure of the interlamellar matrix, which contains a core of chitin [Weiss et al., 2002] coated with proteins [Schaeffer et al., 1997]. Hence, the proteins at the surface of the interlamellar matrix are highly apolar. One candidate for the hydrophobic surface protein may be a silk fibroin-like protein, which presence in the interlamellar matrix has been assumed [Weiner and Traub, 1980], [Sudo et al., 1997].

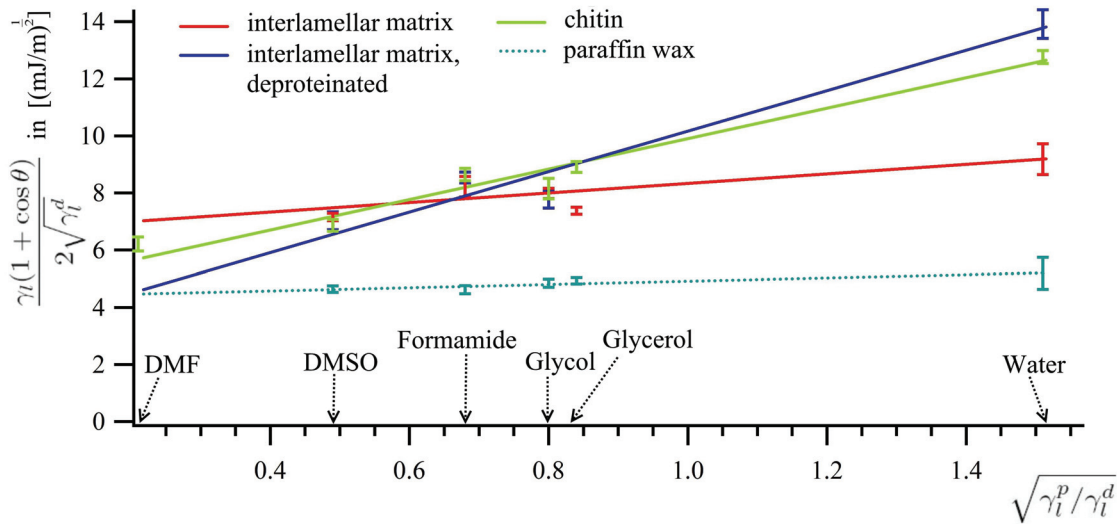


Figure 4.12.: Owens-Wendt plot of contact angle measurements on four substrates: the interlamellar matrix (red), the interlamellar matrix after deproteination with proteinase - K (blue), a chitin film (green) and paraffin to validate the method (gray). The error bars represent the standard deviations. Test liquids are identified by the ratio $\sqrt{\gamma_l^p / \gamma_l^d}$ on the horizontal axis. The most polar liquid on the right is water, followed by glycerol, glycol, formamide, DMSO and DMF (from right to left). The vertical axis corresponds to an expression according to the Owens-Wendt theory, depending only on the liquid and the determined contact angles θ . The slopes of the linear fits represent $\sqrt{\gamma_s^p}$. The intersections with the vertical axis represent $\sqrt{\gamma_s^d}$. The surface free energy of the interlamellar matrix has a high apolar component (the slope of the fit is small). After deproteination of the interlamellar matrix, the polar surface free energy increases (the slope increases) at the expense of the dispersive component (vertical axis intersection). In the deproteinated state, the matrix has similar surface energy properties like a chitin film, which is assumed to build the core of the interlamellar matrix.

It is important to keep in mind that the properties determined by contact angle measurements are average properties. In other words, it is possible that locally constricted polar regions of the interlamellar matrix exist. Hence, these results are not contradictory to a recent publication indicating that a substructure underlying the aragonite platelets exists

[Nudelman et al., 2006]. But an often cited earlier suggestion that the surface of the interlamellar matrix is completely covered by Asp rich proteins [Weiner et al., 1984] could not be verified, because this would result in a high polar component of the surface free energy.

The pronounced swelling of dried interlamellar matrix due to water uptake was interesting. It seems unlikely, that the surface is responsible for this behavior, as it is (slightly) hydrophobic. This seemingly contradictory result may be explained by the sub-structure of the interlamellar matrix sheets: Underneath the hydrophobic protein surface, chitin and presumably other biopolymers (e.g. proteins) are located. At least one of these substances may have a high affinity for water, resulting in the observed swelling behaviour. But it must be noted, that also capillary action due to the high inner surface may play a role.

4.2.3. Hypothesis of Flat Crystal Growth in Nacre due to Surface Free Energy Properties

The idea was developed, that certain surface free energy properties of the interlamellar matrix might be responsible for the unusual flat crystal growth, as observed in the double-diffusion experiments (see section 4.1). For a final validation of this, a surface free energy determination of the aragonite (001) surface is required. This work is currently in progress in a follow-up project performed by Malte Launspach, Biophysics Institute, University of Bremen.

The variable of interest is the theoretical⁸ contact angle θ of an initial aragonite nucleus on the interlamellar matrix.

A low contact angle corresponds to good wetting. Ideal wetting is achieved for $\theta \approx 0$. Therefore, if the calculated contact angle of aragonite (001) on the interlamellar matrix is low, a flat crystal growth may result from especially suitable surface energy properties of the interlamellar matrix.

A second aspect, depending on the contact angle, is the favoring of nucleation on the matrix surface. In classical nucleation theory of spherical, cap-shaped nuclei on a substrate (compare section A.2), the nucleation on a surface is strongly favored compared to nucleation from the solution. This is expressed by a lowering of the critical nucleus size n^* , which describes the number of particles needed to form a stable nucleus. The variable, determining the lowering of n^* compared to nucleation from solution, is the contact angle θ . The lower the contact angle is, the stronger nucleation is favored [Kashchiev and van Rosmalen, 2003].

The contact angle can be calculated by using Young's equation (subscripts M for interlamellar matrix and A for the (001) aragonite surface):

$$\cos \theta = \frac{\gamma_{M-H_2O} - \gamma_{A-M}}{\gamma_{A-H_2O}} \quad (4.1)$$

⁸The contact angle of a microscopic, spherical and cap-shaped nucleus, as it is used in nucleation theory on a substrate. Details see section A.2.

The different interfacial energies can be approximated by using the expression of Owens-Wendt (see equation 3.8):

$$\gamma_{M-H_2O} = \gamma_M + \gamma_{H_2O} - 2\sqrt{\gamma_M^d \gamma_{H_2O}^d} - 2\sqrt{\gamma_M^p \gamma_{H_2O}^p} \quad (4.2)$$

$$\gamma_{A-M} = \gamma_A + \gamma_M - 2\sqrt{\gamma_A^d \gamma_M^d} - 2\sqrt{\gamma_A^p \gamma_M^p} \quad (4.3)$$

$$\gamma_{A-H_2O} = \gamma_A + \gamma_{H_2O} - 2\sqrt{\gamma_A^d \gamma_{H_2O}^d} - 2\sqrt{\gamma_A^p \gamma_{H_2O}^p} \quad (4.4)$$

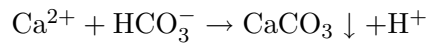
So far, only the interfacial energy between the interlamellar matrix and water can be calculated, resulting in $\gamma_{M-H_2O} = 33.5$ mN/m. The other two quantities γ_{A-M} and γ_{A-H_2O} , necessary to calculate θ , can be obtained after a determination of the surface free energy components of the (001) aragonite surface.

The hypothesis contains several necessary simplifications, such as spherical, cap-shaped nuclei. Possible nucleating regions on the matrix and the influence of the soluble matrix are also ignored. Nonetheless, the proposed ideas might help to explain the lateral growth of aragonite, as well as a favored nucleation on the matrix surface under the low supersaturation of the extrapallial fluid [Crenshaw, 1972]. In both contexts (nucleation and lateral growth), a comparison of calculated contact angles using surface free energy values of calcite and other aragonite faces would be interesting.

4.3. CaCO₃ Precipitation Assay

4.3.1. Introduction

In 1981 Wheeler and colleagues described an assay to investigate the influence of the organic matrix on CaCO₃ precipitation [Wheeler et al., 1981]. They performed simple CaCO₃ precipitation experiments, by mixing solutions of CaCl₂ and NaHCO₃ and recording the pH-value. Due to the chemistry of the system, CaCO₃ precipitation is accompanied by a pH-value drop, which can be summarized in the following reaction:



Practical details of the precipitation assay were described in section 3.6.

During this thesis, this assay was extended such, that the observed pH-value drops can be used to calculate the amount of precipitated [CaCO₃] and the precipitation rate $d[\text{CaCO}_3]/dt$. The newly developed method to determine precipitation rates by measuring the pH-value will be described in the next section, targeting on the calculation of a function $x(\text{pH})$, where x denotes the amount of precipitate. Therefore, it is necessary to describe briefly the essentials of the complex chemical system.

The section concludes with the application of the method. Results of measurements of the influence of the soluble organic matrix on CaCO₃ precipitation rates will be presented and discussed.

4.3.2. Development of a Calculation Method for CaCO₃ Precipitation Rates

First, only the carbonate species in a solution (for example, by dissolution of NaHCO₃ or CO₂ in water) are considered. The amount of carbon atoms, c_0 , is now distributed over the chemical species carbonic acid [H_2CO_3^*] = [$\text{CO}_2(\text{aq})$] + [H_2CO_3], bicarbonate [HCO_3^-] and carbonate [CO_3^{2-}]. The laws of mass action describe the equilibrium concentrations of the carbonate species:

$$K_{a1}^* = K_{a1} \frac{\gamma_{\text{H}_2\text{CO}_3^*}}{\gamma_{\text{H}^+} \gamma_{\text{HCO}_3^-}} = \frac{[\text{HCO}_3^-][\text{H}^+]}{[\text{H}_2\text{CO}_3^*]} \quad (4.5)$$

$$K_{a2}^* = K_{a2} \frac{\gamma_{\text{HCO}_3^-}}{\gamma_{\text{H}^+} \gamma_{\text{CO}_3^{2-}}} = \frac{[\text{CO}_3^{2-}][\text{H}^+]}{[\text{HCO}_3^-]} \quad (4.6)$$

Where γ_x denote activity coefficients, which can be calculated by the extended Debye - Hückel equation [Truesdell and Jones, 1974]. K_{a1} , K_{a2} represent the acid dissociation constants, which can be approximated for a given temperature by empirical expressions [Plummer and Busenberg, 1982]. K_{a1}^* , K_{a2}^* are the effective acid dissociation constants, altered by the activity coefficients.

Since carbon conservation (CO₂ out- or in - gassing is neglected) is assumed, the following

equation results for the amount c_0 of carbon atoms:

$$c_0 = [H_2CO_3^*] + [HCO_3^-] + [CO_3^{2-}] \quad (4.7)$$

By combining the laws of mass action with the carbon conservation in the system, equations for the distribution of carbonate species depending on $[H^+]$ can be obtained:

$$[H_2CO_3^*] = \frac{[H^+]^2 c_0}{[H^+]^2 + K_{a1}^*[H^+] + K_{a1}^* K_{a2}^*} \quad (4.8)$$

$$[HCO_3^-] = \frac{[H^+] c_0 K_{a1}^*}{[H^+]^2 + K_{a1}^*[H^+] + K_{a1}^* K_{a2}^*} \quad (4.9)$$

$$[CO_3^{2-}] = \frac{c_0 K_{a1}^* K_{a2}^*}{[H^+]^2 + K_{a1}^*[H^+] + K_{a1}^* K_{a2}^*} \quad (4.10)$$

In the presence of the cations sodium and calcium, to some extent the ion pairs $NaCO_3^-$, $NaHCO_3^0$, $CaCO_3^0$ and $CaHCO_3^+$ will form. The equilibrium amount of each ion pair is described by the laws of mass action:

$$K_{NaCO_3^-} = \frac{\gamma_{NaCO_3^-} [NaCO_3^-]}{\gamma_{Na^+} [Na^+] \gamma_{CO_3^{2-}} [CO_3^{2-}]} \quad (4.11)$$

$$K_{NaHCO_3^0} = \frac{\gamma_{NaHCO_3^0} [NaHCO_3^0]}{\gamma_{Na^+} [Na^+] \gamma_{HCO_3^-} [HCO_3^-]} \quad (4.12)$$

$$K_{CaCO_3^0} = \frac{\gamma_{CaCO_3^0} [CaCO_3^0]}{\gamma_{Ca^{2+}} [Ca^{2+}] \gamma_{CO_3^{2-}} [CO_3^{2-}]} \quad (4.13)$$

$$K_{CaHCO_3^+} = \frac{\gamma_{CaHCO_3^+} [CaHCO_3^+]}{\gamma_{Na^+} [Ca^{2+}] \gamma_{HCO_3^-} [HCO_3^-]} \quad (4.14)$$

The equilibrium constants can be found in [Plummer and Busenberg, 1982] and [Akagi and Kono, 1995]. Taking those ion pairs into account, the conservation of carbon atoms can be expressed in the following equation:

$$c_0 = [H_2CO_3^*] + [HCO_3^-] + [CO_3^{2-}] + [NaCO_3^-] + [NaHCO_3^0] + [CaCO_3^0] + [CaHCO_3^+] \quad (4.15)$$

If all carbon species and the ions calcium, sodium and chlorine are considered, the charge conservation can be expressed as follows (K_w denotes the ion product of water):

$$[H^+] + [Na^+] + 2[Ca^{2+}] + [CaHCO_3^+] = K_w/[H^+] + [Cl^-] + [HCO_3^-] + 2[CO_3^{2-}] + [NaCO_3^-] \quad (4.16)$$

Compared to $CaCO_3$ precipitation, all reactions are very fast⁹. Therefore, during precipitation, all carbonate species and ion - pairs can be considered in equilibrium. They adapt within milliseconds to concentration changes due to $CaCO_3$ precipitation, which takes place

⁹The slow carbon dioxide hydration can be neglected in the considered pH - regime > 7.0 .

at a timescale of seconds to minutes. Because precipitation removes carbon atoms from the equilibria described above, the amount of free carbon $c(t)$ over time will decrease:

$$c(t) = c_0 - x(t) \quad (4.17)$$

In the same way, the amount of dissolved calcium $ca(t)$ decreases by precipitation:

$$ca(t) = ca(t = 0) - x(t) \quad (4.18)$$

Where $x(t) = [CaCO_3](t)$ denotes the amount of precipitate.

The equations 4.17 and 4.18 combined with the charge neutrality equation 4.16, the distribution of the carbonate species: equations 4.8, 4.9 and 4.10 and the laws of mass action for the ion pairs, equations 4.11, 4.12, 4.13 and 4.14, describe the system completely. Thus, by knowing the initial concentrations and the pH - value at a given time, the amount x of precipitate can be calculated.

This set of equations can be used to calculate the amount of precipitate x for a given pH - value using mathematical computer software or an aqueous solution simulation program like PHREEQC (used here) [Parkhurst and Appelo, 1999]. The resulting function $x(pH)$ (see figure 4.13) can be used to determine the amount of precipitate x by measuring the pH - value.

To calculate the precipitation rate $d[CaCO_3(s)]/dt$, the calculated precipitate $x(t)$ was smoothed with a cubic spline across 20 - 50 interpolation - points. This was necessary because of digit jumps in the recorded pH - values (e.g. 7.40 to 7.39), which would cause a high slope at the point of digit jump and no slope in between digit jumps. The smoothing was programmed using the scientific software package IGORpro (Wavemetrics, Portland, USA). The pH - course of a typical experiment is shown (figure 4.14 (a)). By using the precipitate function $x(pH)$, the amount of precipitate over time was calculated (figure 4.14 (b), solid curve). The time derivative of the smoothed precipitate resulted in the precipitation rate (figure 4.14 (b), dashed curve). In each experiment the maximum precipitation rate was chosen as a parameter.

4.3.3. Results

In figure 4.14 (a), the pH - course of an example measurement without additive is shown. Immediately after mixing, a sudden pH - value drop occurs for a few seconds. Presumably, this is caused by ion-pair formation [Wheeler et al., 1981]. The pH - value then stabilizes to a plateau value with slightly varying length. During this period the solution is metastable and not turbid (compare figure 4.15). After several tens to hundreds of seconds the solution starts to become turbid and the pH - value begins to drop, indicating precipitation. At

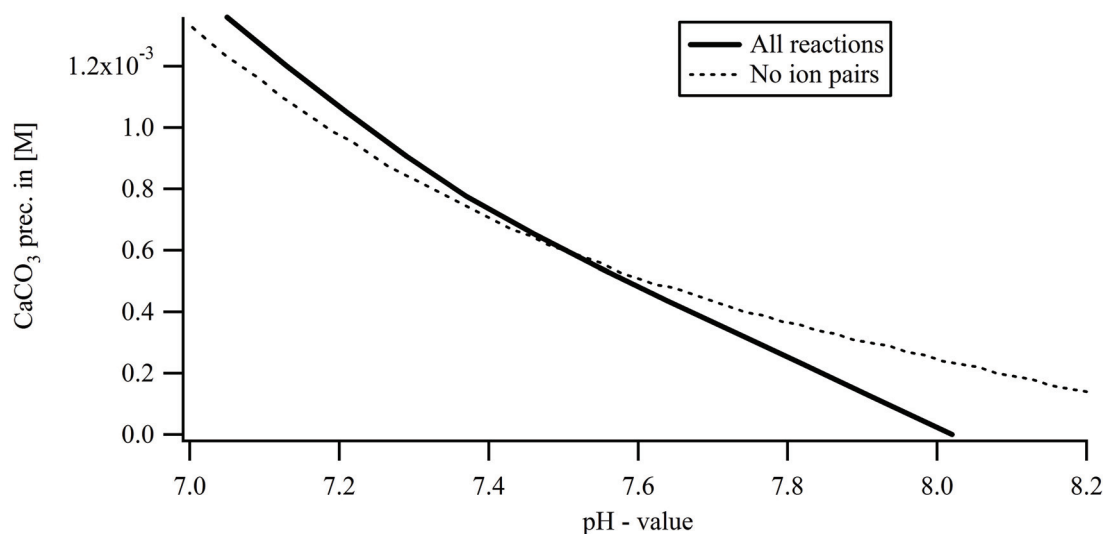


Figure 4.13.: The pH - value during CaCO_3 precipitation experiments can be used to calculate the amount of precipitate. The graph shows calculations for the mixing of 60 ml of 20 mM NaHCO_3 with 0.5 ml of 0.05 M NaOH and 60 ml of a 20 mM CaCl_2 solution. Due to the chemistry of the system, CaCO_3 precipitation results in a pH - value drop. It is important to include ion pair formation, as the result of a complete calculation (solid line) deviates greatly from calculations without ion pairs (dashed line).

the beginning the precipitation rate accelerates very quickly, reaching a maximum relatively soon after the reaction started. Due to consumption of dissolved calcium and carbonate and the decreasing pH, the precipitation rate slowly decreases and stops after a while.

Figure 4.15 illustrates the course of the pH - value and IR - transmittance of four different illustrative experiments. The reference experiment and the experiment with 6 $\mu\text{g}/\text{ml}$ BSA differ only slightly by a lower slope of the pH decrease in the experiment with BSA (resulting in a lower precipitation rate) and a slightly higher final pH - value in the experiment (higher saturation state of the solution after precipitation). When mixing was performed in the presence of soluble matrix (here: 1 $\mu\text{g}/\text{ml}$, see figure 4.15 (c) for an SDS - PAGE of the protein mixture), precipitation could be completely inhibited and the solution stayed completely clear.

The positive slope of the pH was caused by CO_2 out gassing. When the soluble organic matrix was added after precipitation had already started, the precipitation could be stopped nearly instantaneously, indicated by a sharp bending in the pH - course and the turbidity.

In each experiment the maximum precipitation rate was chosen as a parameter. A series of experiments with the soluble organic matrix of nacre, BSA and lysozyme was performed at varying concentrations. In figure 4.16, the influence of the different additives on the maximum precipitation rate is shown. Lysozyme has a very low influence on the observed precipitation rates, whereas BSA shows inhibitory potential at concentrations of 10 $\mu\text{g}/\text{ml}$

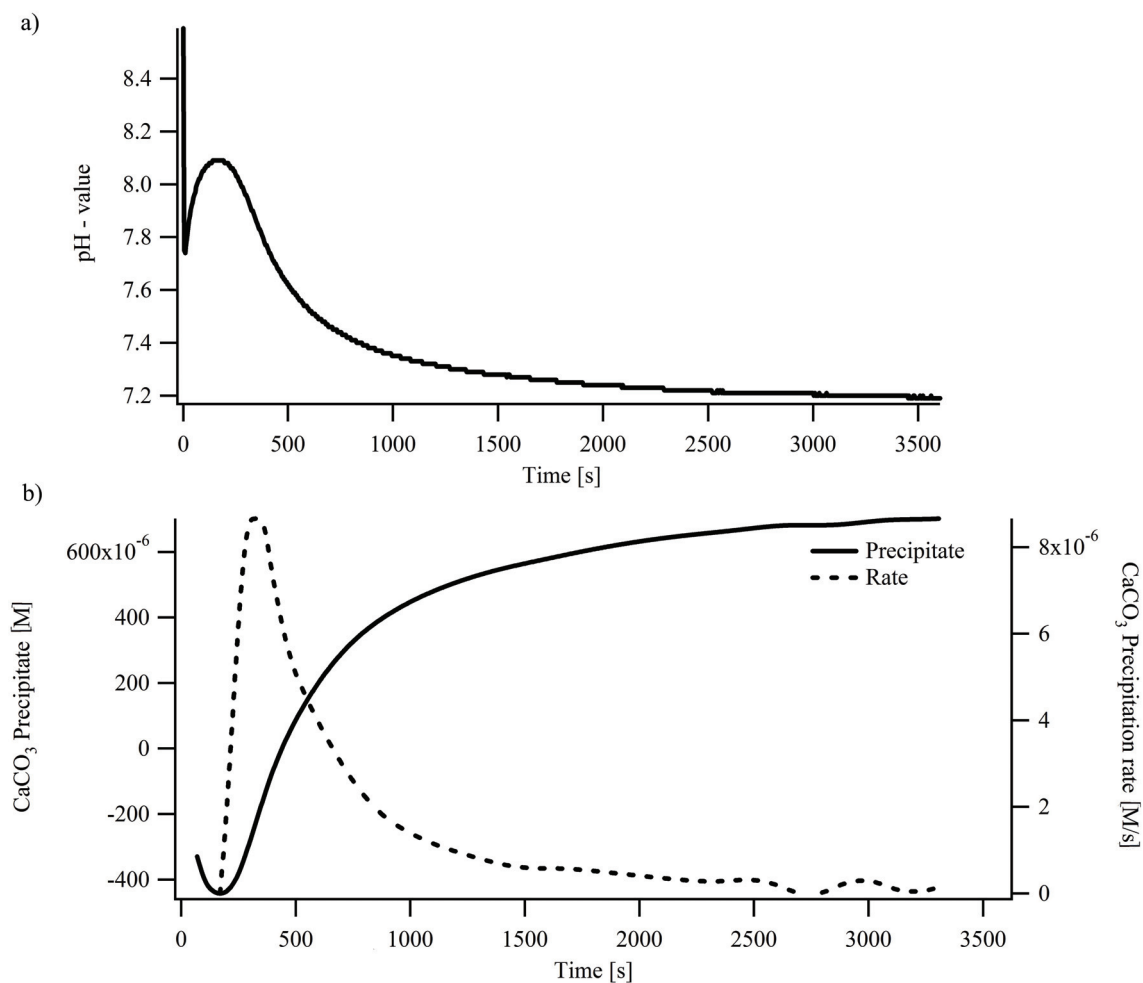


Figure 4.14.: Example evaluation of the precipitation experiments. 60 ml of 20 mM NaHCO₃ with 0.5 ml of 0.05 M NaOH and 60 ml of 20 mM CaCl₂ were mixed. (a) Typical pH - value course for a mixing experiment. This is used to calculate the precipitation rate. (b) Calculated amount of CaCO₃ precipitate and precipitation rate. Typically the rate rises very quickly to a maximum value and slowly decreases to zero afterwards. The maximum of the precipitation rate was taken as a parameter.

and higher. For BSA the maximum effect was a decrease of precipitation rates to one third when compared to reference experiments.

In contrast, the soluble organic matrix of nacre showed an overall pronounced rate modifying effect, with a strong concentration dependence on the effect type. Enhanced rates by a factor of 1.5 (compared to experiments without additives) were observed at concentrations of 0.02 $\mu\text{g}/\text{ml}$. Further increase of the organic matrix concentration led to a lower and lower precipitation rate until precipitation was completely inhibited at concentrations of 1.0 $\mu\text{g}/\text{ml}$ and higher.

XRD investigation of dried precipitate was performed. The obtained diffraction peaks without additive (figure 4.17, (a)) and in the presence of 0.6 $\mu\text{g}/\text{ml}$ matrix proteins (figure

4.17, (b)) showed that in both cases calcite was precipitated as indicated by the peaks at $2\theta = 29.4^\circ$ ((104) plane of calcite, $d = 3.03 \text{ \AA}$) and $2\theta = 31.5^\circ$ ((006) plane of calcite, $d = 2.8 \text{ \AA}$) [Downs, 2006]. The amplitudes of the calcite peaks were different in the two experiments, most likely caused by morphological differences in the two experiments, which led to some orientation during drying on the glass cover slides.

4.3.4. Discussion

The method of calculating the maximum CaCO_3 precipitation rate in an easy to implement tabletop experiment is an extension of experiments published in 1981 [Wheeler et al., 1981]. The presented method is complementary to other functional studies on biomineralizing proteins, e.g., the ammonium carbonate method or AFM investigations (*in vitro* crystallization with proteins on calcite surfaces under growth or dissolution conditions). These two methods give an insight into the mechanisms of crystal growth modification by proteins (and polymorph selection when combined with XRD), but they lack easily comparable parameters, which can be measured with the presented method.

Although mixtures of nacre proteins were used which presumably also contained proteins not interacting with CaCO_3 , it was possible to inhibit the growth of CaCO_3 completely from a highly supersaturated solution with protein concentrations of only $1.0 \mu\text{g/ml}$. The mechanism of inhibition can be concluded from AFM investigations on growing calcite surfaces (e.g. [Treccani et al., 2006], [Mann et al., 2007]). Like other crystal modifying proteins, nacre proteins bind to certain surface features (often steps), locally blocking the attachment of ions and thus increasing the solubility of CaCO_3 by preventing subcritical nuclei to become supercritical.

The function of this strong inhibitory capability is possibly to prevent uncontrolled crystal growth in the supersaturated extrapallial fluid, or when crystal face and / or polymorph specific, a more subtle morphological growth control. When compared to other proteins, nacre proteins (as examples for other biomineralizing proteins in CaCO_3 biomineralization) influence CaCO_3 nucleation and growth extremely specified (figure 4.16). The multi function plasma protein BSA, which also binds to Ca^{2+} for transport reasons, was slightly inhibitory at high concentrations, but it did not prevent nucleation completely. With the antibacterial protein lysozyme as an example of a very unspecific protein, no significant effect on the rates was observable.

At very low concentrations, the inhibitory potential of the organic matrix disappeared and a significant rate enhancement by a factor of 1.5 was observed (figure 4.16). This interesting concentration dependence of the rate modifying capability of the organic matrix might be the superposition of enhancing effects from some matrix proteins and inhibiting effects from other proteins, with different concentration dependencies. In this interpretation, enhancing compounds were active at concentrations where inhibition is not yet possible, but at higher concentrations the inhibiting compounds dominated by blocking all subcritical nuclei.

A different interpretation of this concentration dependency is induced by recent mea-

surements of the enhancing / inhibiting capability with model peptides in AFM growth experiments on calcite [Elhadj et al., 2006]. The authors found a contrast behavior for isolated compounds with enhancement at low concentrations and inhibition at higher concentrations. The capability to enhance calcite step propagation at low concentrations was found to be dependent on both the degree of peptide net negative charge and the degree of hydrophilicity. As an explanation for the rate enhancement mechanism, the authors propose a catalytic lowering of the energy barrier for ion attachment. The acidic peptides may ease the incorporation of Ca^{2+} by their local electrostatic potential. Hydrophilic peptides locally restructure water around the crystal surface and therefore ease ion diffusion from the bulk to the surface.

In contrast to the inhibitory effect, this proposed catalytic effect needs no additive binding to the crystal nuclei surface, whereas in the inhibitory concentration range each monomolecular step of a crystal has to be blocked by one molecule. Although somewhat simplified, this might explain why enhancement takes place at lower concentrations than inhibition.

In the light of this highly concentration-dependent behavior, it may be too simple to conclude that either inhibition or enhancement is caused by a certain type of biomineralizing protein. In this study, the influence on precipitation of a mixture of nacre proteins (> 3500 Da) was investigated, representing the addition of single protein effects. It is yet unknown if isolated proteins also show this two-sided behavior, or if a superposition of effects was measured. To get the full picture, a wide concentration range using isolated or recombinant proteins should be investigated.

The growth of nacre is a complex interplay of controlled nucleation as well as polymorph and crystal face dependent growth control. According to the presented results, the mode of operation of all participating proteins strongly depends on their local concentrations in the extrapallial fluid.

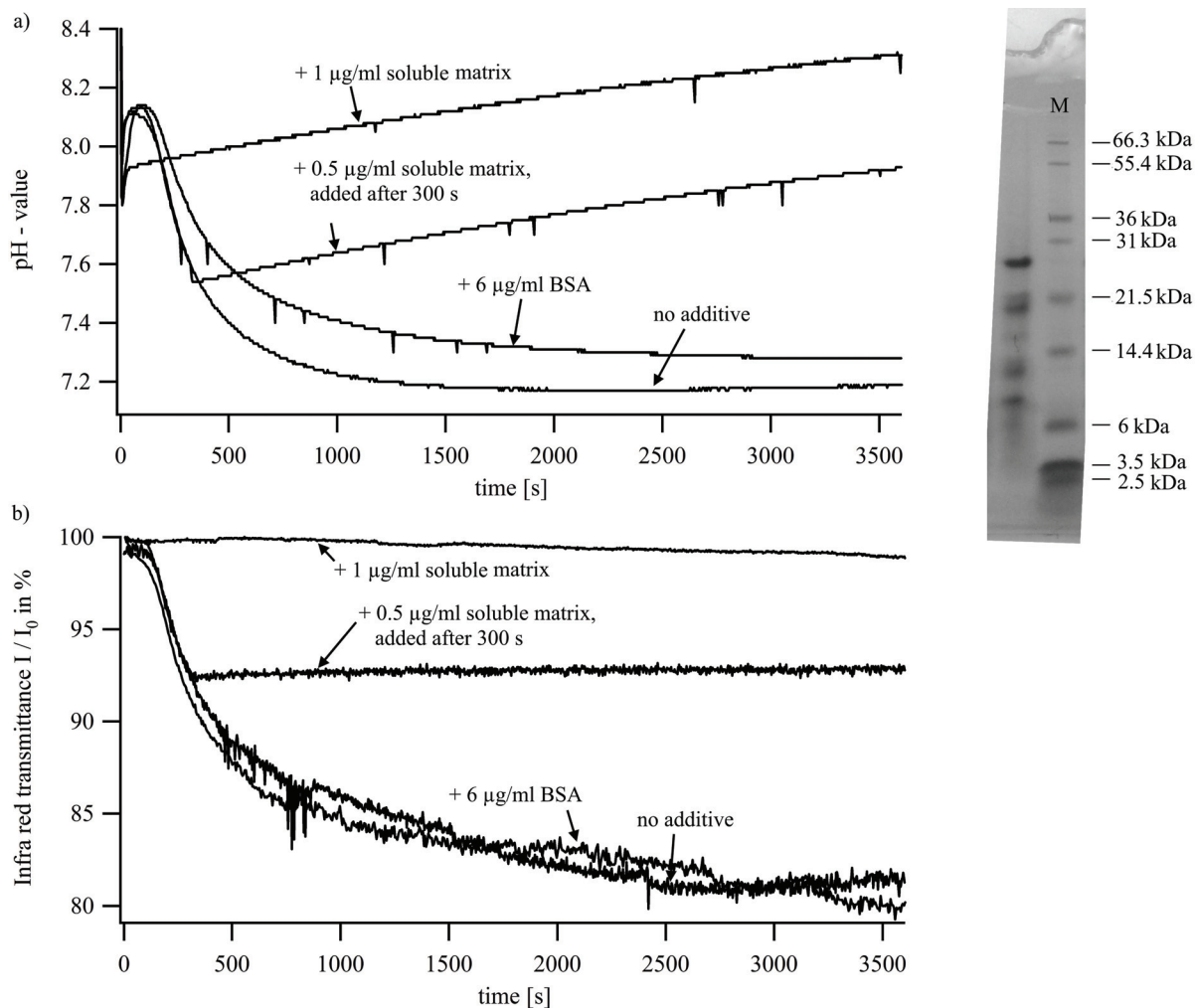


Figure 4.15.: Composition of illustrative and representative precipitation experiments. 60 ml of 20 mM NaHCO_3 with 0.5 ml of 0.05 M NaOH and 60 ml of 20 mM CaCl_2 were mixed. (a) pH - courses. (b) IR - transmittances. The experiments with no additive and BSA differ only slightly, whereas the soluble organic matrix shows a pronounced inhibiting capability even when added to the solution after precipitation began. (c) SDS - PAGE of the protein mixture obtained by dissolving nacre from the gastropod *Haliotis laevigata* with 6 % acetic acid (left column). The right column represents the protein standard with molecular weights in kDa.

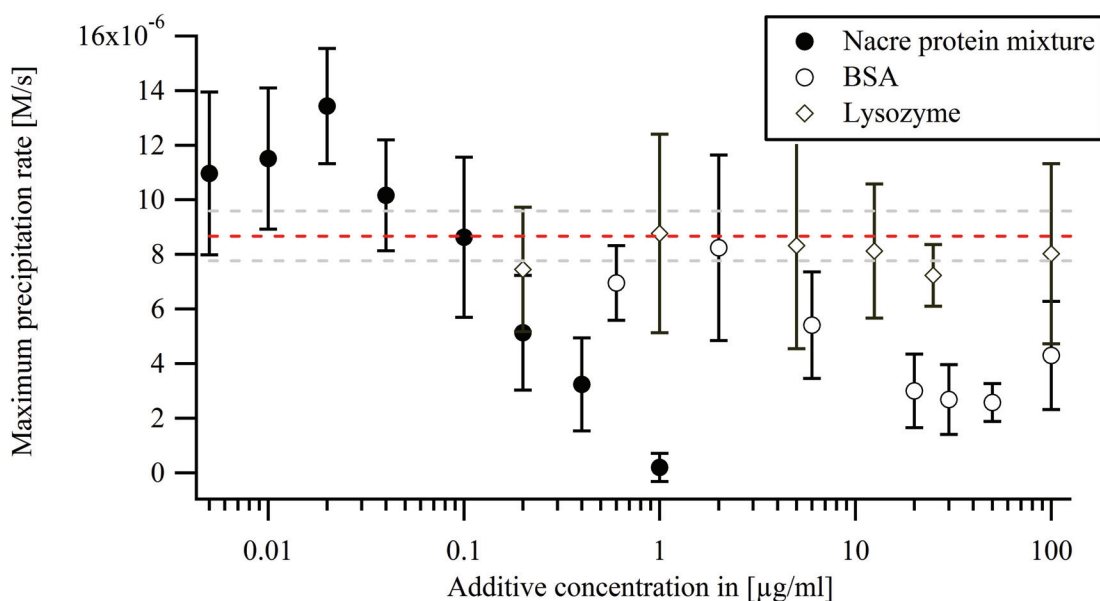


Figure 4.16.: Comparison of maximum precipitation rates in the presence of the nacre soluble matrix (filled circles), Lysozyme (rhombs) and BSA (empty circles). 60 ml of 20 mM NaHCO_3 with 0.5 ml of 0.05 M NaOH and 60 ml of 20 mM CaCl_2 were mixed and the precipitation rate calculated from the pH - value. Each data point represents the average of at least six experiments. Error bars represent the 95% confidence interval of the average. The dashed line represents the reference experiment without additive with 95% confidence interval (gray dashed lines). In low concentrations the soluble matrix enhanced the precipitation rates up to a factor of 1.5. At higher concentrations, the mixture of nacre proteins shows a very strong potential of inhibiting crystal growth compared to the non - specific BSA. Lysozyme addition has no, or only a very low, effect on the precipitation rate.

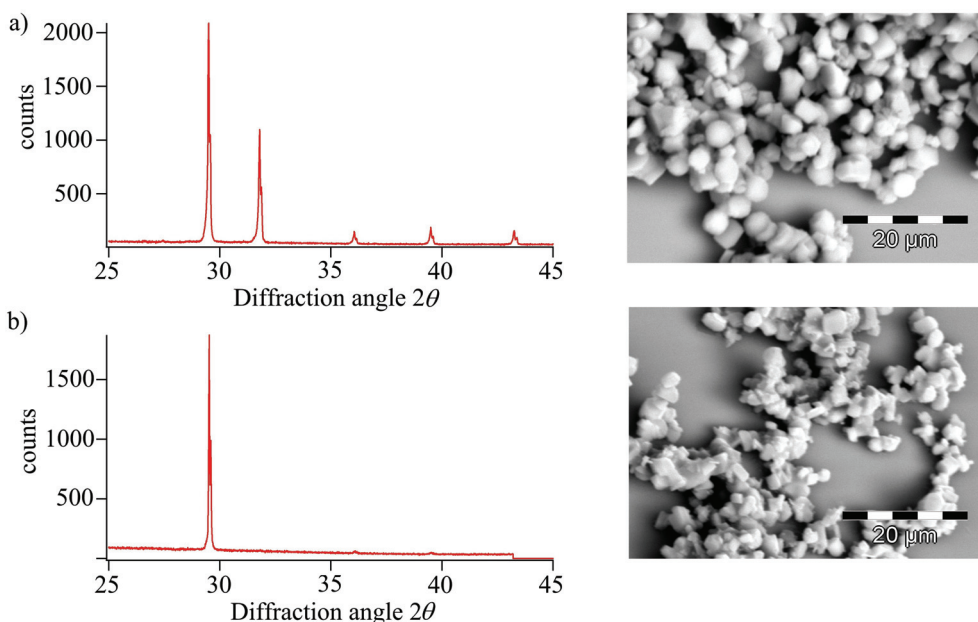


Figure 4.17.: Crystals obtained in the precipitation experiments. (a) XRD and SEM of precipitate without additives. (b) XRD and SEM (backscattered electrons) of precipitation experiment with 0.6 $\mu\text{g/ml}$ soluble matrix. In both cases calcite was precipitated with slight morphological differences.

4.4. Amino Acid Analysis

4.4.1. Introduction

The soluble organic matrix of nacre from the gastropod *Haliotis laevigata* was subject to an amino acid analysis. This investigation was performed because of the discrepancy between published results indicating high contents of acidic amino acids in the soluble matrix and the low or average content of these residues in the purified proteins. The amino acid analysis procedure and the preparation of the soluble matrix was performed as described in section 3.7.3.

Initially, extensive work was expended to establish the method, including a reproducible separation of all amino acids and a calibration for each amino acid. This will be described in the first part of this section. Next, the results of validation tests using known proteins are presented. After these necessary preparations, the amino acid analysis was performed using the soluble organic matrix of nacre. Description and discussion follows in the final part of the current section.

4.4.2. Establishment and Calibration of the Method

For a quantitative amino acid determination it was necessary to perform a calibration using amino acid standards. These calibration experiments also served as tests for the stability of the procedure. The constancy of retention times had to be tested as well as the ability to perform a complete separation of all amino acids. In figure 4.18 (a), a chromatogram of the amino acid standard is shown. As previously observed [Ebert, 1986], the retention times turned out to be quite sensitive to the column equilibration time before performing the HPLC gradient run. Therefore, the column was always equilibrated for 10 min before each HPLC gradient run with the solution mixture of the gradient start. The first eluting PTC - amino acids always had a stronger variation in retention times than the later eluting (the average standard deviation for the first three amino acids was approximately 25 s, the last six had a standard deviation of approximately 6 s). The deviation from the mean retention time was always similar for neighbouring peaks, leaving the order of elution unchanged, which was important for the identification of peaks.

The separation of several amino acids was problematic. In the first experiments the arginine and threonine peaks as well as the alanine and proline peaks were merged. Further investigation showed that the separation of these amino acids was extremely sensitive to the TEA concentration (which acts through an ion pairing mechanism [Cohen and Strydom, 1988]) and the pH-value. A higher concentration of TEA generally resulted in higher retention times for acidic amino acids (especially cysteic acid, aspartic acid and glutamic acid) because binding to the hydrophobic column was improved. By performing a NaOH titration of the aqueous buffer A, it became evident that the pH-value of 6.40 in the PTC-amino acid separation protocol by Ebert [Ebert, 1986] was problematic (see figure 4.18 (d)). At this

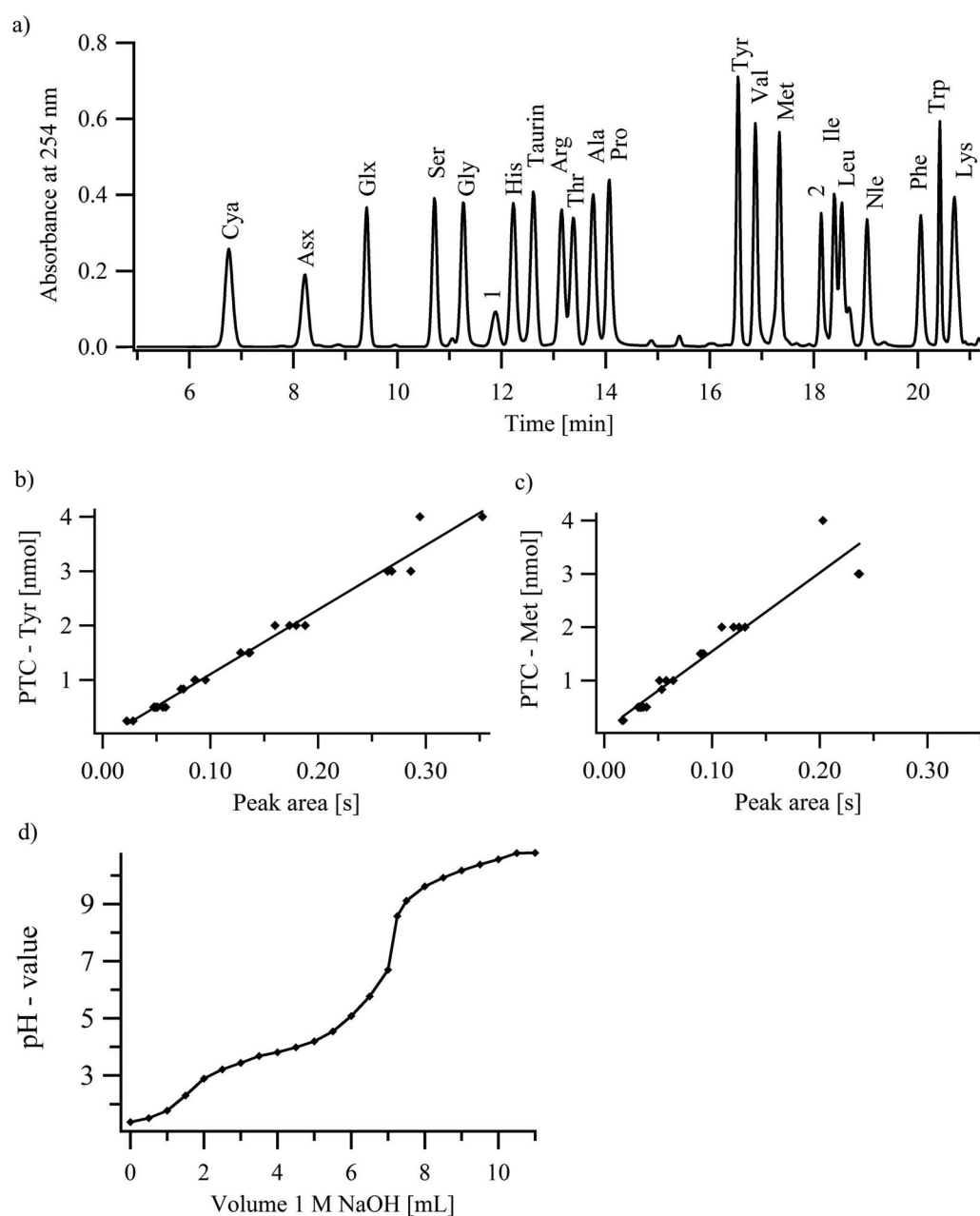


Figure 4.18.: (a) Chromatogram of C18 - HPLC separation of PITC derivatized amino acid standard solution (A 2908, Sigma Aldrich, Saint Louis, USA) for calibration. Peaks were identified by measuring the absorbance at 254 nm. The standard three letter amino acid codes were used with Nle referring to norleucin and Cya referring to cysteic acid. Asx stands for the sum Asp + Asn, and likewise Glx for Glu + Gln. The numbers in the chromatogram correspond to ammonium (1) and to cystine (Cys_2) (2). The amount of each amino acid was 4 nmol, except for cystine with an amount of 2 nmol. (b), (c) Example of calibration plots of the amino acid analysis method with linear fit. The peak area (at 254 nm) is plotted against the amount of PTC-amino acid. The best (b, tyrosine) and the worst fit (c, methionine) are shown. (d) Acid-base titration of buffer A to examine the pH - value stability, which was crucial for separation of several amino acids. 100 ml buffer A (50 mM Na-acetate, 2.75 ml TEA, initial pH 6.40 adjusted with H_3PO_4) was titrated with 1 M NaOH, the starting pH-value was achieved by HCl addition. The solution was very sensitive to pH-value changes at pH 6.40, the optimum pH-value for amino acid separation.

Table 4.3.: Calibration values $\Delta n/\Delta A$ for the PTC-amino acids at 254 nm in the order of elution. Unknown amounts of amino acids can be obtained by multiplying the peak area A with the specific calibration value.

Amino acid	Three letter code	Amount per peak area $\Delta n/\Delta A$ [nmol/s]	Standard deviation $s_{\Delta n/\Delta A}$ [nmol/s]
Cysteic acid	Cya	15.83	0.49
Aspartic acid	Asp	14.99	0.76
Glutamic acid	Glu	17.05	0.43
Serine	Ser	16.52	0.55
Glycine	Gly	15.43	0.48
Histidine	His	13.65	0.45
Arginine	Arg	16.02	0.53
Threonine	Thr	14.16	0.59
Alanine	Ala	13.48	0.53
Proline	Pro	13.07	0.34
Tyrosine	Tyr	11.85	0.29
Valine	Val	12.29	0.34
Methionine	Met	14.75	0.85
Isoleucine	Ile	17.62	0.41
Leucine	Leu	14.28	0.47
Phenylalanine	Phe	18.17	0.62
Tryptophane	Trp	18.44	0.69
Lysine	Lys	13.39	0.51

pH-value the buffering capacity was nearly minimal. Experiments with systematic variation of TEA and pH-value showed that the optimal separation conditions were unfortunately indeed at a pH-value of 6.40 with a concentration of 2.75 ml/l TEA. Already at a deviation in pH-value of 0.1 the four problematic amino acids peaks (Arg, Thr, Ala, Pro) were merged substantially¹⁰. Hence, the pH-adjustment with phosphoric acid was performed with utmost care, the solution was covered tightly to reduce CO₂ ingassing and the constancy of the pH-value of the buffer was checked on a regular basis.

When following these precautions a complete separation of PTC - amino acids was possible without problems. A calibration plot was performed for each amino acid and a reasonable linear relationship of PTC-amino acid amount and peak area was obtained for all amino acids (see figure 4.18 (b), (c)). Table 4.3 shows the resulting slopes of the linear fit for all required amino acids from the standard solution.

4.4.3. Validation of the Procedure Using Known Proteins

Before the amino acid analysis of unknown samples, the whole procedure was validated using proteins of known composition. The aim was to determine the accuracy of the obtained values and discover possible pitfalls of the method. The proteins lysozyme and bovine serum albumin were hydrolyzed, PITC derivatized and analyzed by HPLC. Furthermore,

¹⁰Such a small deviation of the pH-value can occur easily in a solution which is in use for over a week, e.g., by CO₂ ingassing or influence of the glass.

the method for cysteine content determination (hydrolysis in the presence of 0.20% NaN_3) was tested on both proteins. The separated determination of asparagine / aspartic acid and glutamine / glutamic acid content (BTI treatment of denatured proteins) was tested using BSA.

Table 4.4.: Determined amino acid composition of known proteins for a validation of the amino acid procedure. The numbers represent average molar fractions in %. The predicted values for lysozyme are from [Canfield, 1963] and those for BSA are from [Brown, 1975] and [Hirayama et al., 1990]. Cya corresponds to the cysteine content. Asx stands for Asp + Asn, Glx for Glu + Gln.

Amino acid	Lysozyme			BSA		
	observed	deviation	(predicted)	observed	deviation	(predicted)
Cya	6.4	0.0	(6.4)	5.4	-0.4	(5.8)
Asx	14.8	-1.9	(16.7)	8.5	-0.5	(9.0)
Glx	4.0	0.0	(4.0)	12.2	-0.8	(13.0)
Ser	9.2	1.3	(7.9)	4.5	-0.8	(5.3)
Gly	12.1	2.6	(9.5)	3.0	0.2	(2.8)
His	0.8	0.0	(0.8)	2.8	0.2	(2.6)
Arg	5.7	0.1	(5.6)	4.7	0.4	(4.3)
Thr	10.8	2.1	(8.7)	3.8	-1.8	(5.6)
Ala	9.7	0.2	(9.5)	8.5	0.6	(7.9)
Pro	2.0	0.4	(1.6)	4.9	0.3	(4.6)
Tyr	2.1	-0.3	(2.4)	3.6	0.1	(3.5)
Val	5.1	0.3	(4.8)	6.2	-0.1	(6.3)
Met	1.1	-0.5	(1.6)	0.8	0.0	(0.8)
Ile	5.6	0.9	(4.7)	2.0	-0.5	(2.5)
Leu	6.0	-0.4	(6.4)	9.4	-1.3	(10.7)
Phe	2.9	0.5	(2.4)	3.8	-1.1	(4.9)
Trp	0.0	-2.4	(2.4)	0.3	-0.2	(0.5)
Lys	1.8	-3.0	(4.8)	15.6	5.7	(9.9)

In figure 4.19 two example chromatograms of PITC derivatized lysozyme hydrolysate are shown. Figure 4.19 (a) shows a chromatogram where conventional (6 M HCl, 0.2% phenol, 110 °C, for 24 h) hydrolysis was performed, whereas figure 4.19 b shows a chromatogram after hydrolysis in the presence of NaN_3 . Both chromatograms are of good quality with easily identifiable peaks and a low number of unknown peaks. In the chromatogram 4.19 (b) the occurrence of a cysteic acid (Cya) peak before the Asx peak is visible, indicating that the oxidation of cysteine and cystine to cysteic acid during the hydrolysis in the presence of NaN_3 did occur. Comparison of several chromatograms obtained after conventional hydrolysis with those after hydrolysis in the presence of NaN_3 revealed that in the latter the methionine peaks were always lowered (compare the Met peaks in figure 4.19 (a) and (b))¹¹.

In table 4.4 the determined amino acid fractions for BSA and lysozyme are shown. Comparison of the obtained values with values obtained from the protein sequences showed that generally most amino acids could be determined with a good precision with two major ex-

¹¹This results from partial oxidation of methionine to methionine sulfone in the presence of NaN_3 [Fountoulakis and Lahm, 1998]

ceptions: Lysine could not be determined with satisfying precision (deviation -3.0% and +5.9%) possibly because of an overlapping peak with by-products of the PITC derivatization, which elute after 20 min. The determined fractions of threonine for both proteins had a relatively high deviation (-2.0% and +1.9%) from the predicted values, likely due to a partial overlap of the threonine peak with the arginine peak.

HPLC separation of hydrolyzed and PITC derivatized BSA after BTI treatment led to separated values for asparagine / aspartic acid and glutamine / glutamic acid. The chromatograms were highly altered (several unknown peaks occurred; only a few PTC - amino acid peaks could be identified) compared to chromatograms without BTI treatment (data not shown). The percentages of Asp and Glu were calculated by taking the molar fraction of Arg as a reference, because the Arg peak was easy to identify and not denoted among the altered amino acids by [Soby and P., 1981]. The aspartic acid peak was reduced to 5.00%; whereas without BTI treatment the Asx peak was 8.5%, resulting in Asp = 5.0% and Asn = 3.5% (predicted values Asp = 6.8%, Asn = 2.3%). In the same manner, the glutamic acid content was determined as 10.1% and glutamine as 2.1% (predicted values Glu = 9.6%, Gln = 3.5%). Although the above deviations from the predicted fractions were only moderate, the results after the BTI treatment were considered as insecure: The results highly depend on the accuracy of the amino acid taken for reference while having strongly altered chromatograms at the same time.

4.4.4. Soluble Organic Matrix of Nacre

In figure 4.20, a typical chromatogram of the PTC - amino acids obtained by hydrolysis of the soluble matrix without further protein purification is shown. A high number of peaks of unknown origin was present, creating a noisy background of the chromatograms. Two of the unknown peaks were especially dominant: one eluting directly after glycine (possibly ammonium) and one directly after proline. Because of the high number of unknown peaks, which often eluted close to, or overlapped with, amino acid peaks, a determination of amino acid fractions was not possible.

Using further protein specific purification, each method led to easily evaluable chromatograms. Ultracentrifugation, cation exchanger purification and C18 - ZipTip purification of the soluble matrix increased the protein fraction in the samples, as the chromatograms contained mostly peaks belonging to PTC - amino acids (figure 4.21). The determined amino acid fractions are shown in table 4.5. The amino acid fractions were reproducible for each purification method but differed greatly from method to method.

Four amino acids were peculiarly high after all methods: proline, glycine, leucine and alanine. Among these amino acids, the proline content had the greatest dependency on the purification method. After ultracentrifugation, about one of four of the obtained amino acids was proline, whereas after cation exchange chromatography about one of seven and after ZipTip purification one of ten amino acids was proline.

The fraction of the potential acidic residues Asx and Glx was also very dependent on

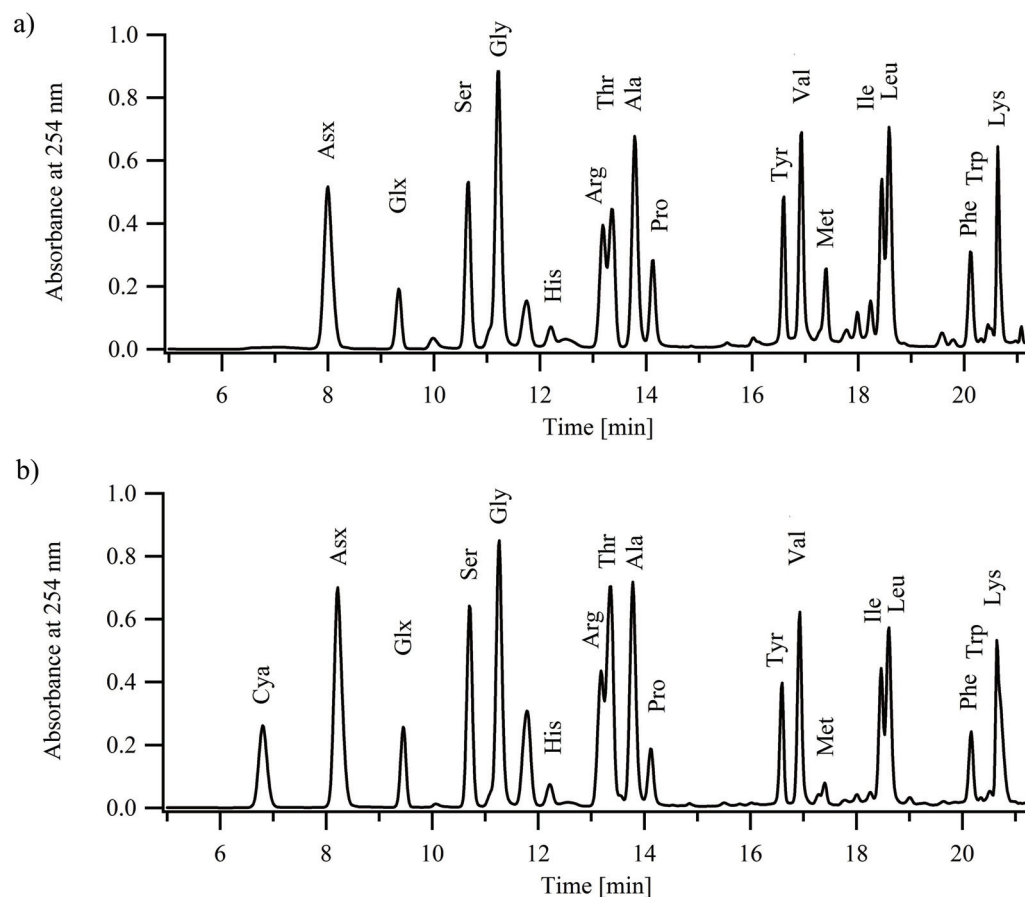


Figure 4.19.: Validation of the procedure. Chromatograms of PTC-amino acids obtained by hydrolysis of lysozyme. (a) Using conventional (6M HCl, 0.2% phenol, 110 °C, for 24 h) protein hydrolysis and (b) using hydrolysis in the additional presence of 0.20% NaN₃ for cysteine determination. The occurrence of the cysteic acid peak indicates the reaction of cystine and cysteine to cysteic acid.

the purification method¹². Using ultracentrifugation to purify the matrix resulted in a very low Asx and Glx yield (Asx + Glx = 3.9%). When using ZipTips or a cation exchanger for protein purification, a higher amount of potential acidic amino acids was obtained, especially in the case of the ZipTips, where one fifth of the amino acids was potentially acidic (Asx + Glx = 20.6%).

Furthermore, when using ZipTip and cation exchanger purification, an unknown peak eluted between the Glx and Ser peaks, which is possibly hydroxyproline¹³.

Collagen indicators: With all purification methods, high levels of proline and glycine were observed. Additionally, a peak which may belong to hydroxyproline was observed when using

¹²The treatment with BTI to identify Asp and Glu resulted in no evaluable chromatograms. Hence, only Asx and Glx values could be determined.

¹³The same retention behaviour (elution between glycine and serine) was also found for hydroxyproline during the establishment of the method (data not shown) and is also reported by [Heinrikson and Meredith, 1984] using a comparable system.

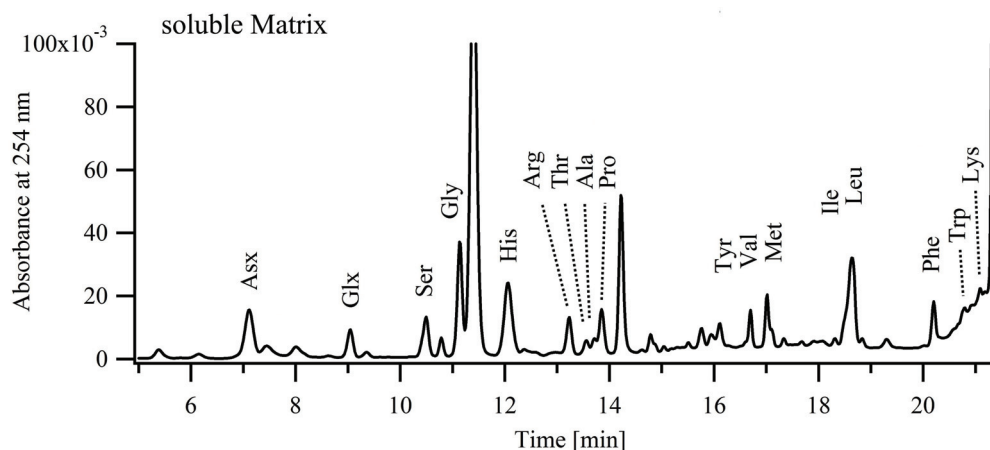


Figure 4.20.: Best case chromatogram of the PTC - amino acids obtained by hydrolysis of the soluble organic matrix extracted by demineralization of nacre with 6% acetic acid and 0.22 μm filtration. This represents the usual preparation of the soluble matrix. However, without further purification steps to increase the protein content in the sample, the amount of unknown peaks was too high to safely identify amino acids and their fractions.

the C18 - ZipTips or the cation exchanger for purification. Hydroxyproline is a nonstandard amino acid derived by hydroxylation of proline. Hydroxyproline is known to occur almost exclusively in the fibrous protein collagen, where it is a major component [Kesava Reddy and Enwemeka, 1996]. Collagen has a typical sequence pattern composed of Gly-X-Y, where X is often proline and Y often hydroxyproline.

In a previous study, a high level of proline was found in supernatants of the interlamellar matrix after treatment with the protease subtilisin [Weiss et al., 2002]. Furthermore, it was reported that some of the interlamellar matrix proteins were sensitive to the collagen-specific protease collagenase [Schaeffer et al., 1997]. It seems likely that a collagen-like protein was present in the samples, presumably originating from the interlamellar matrix. As the crushed nacre is in constant motion¹⁴ during the demineralization process, the interlamellar matrix may be subject to partial mechanically induced disintegration. Hence, smaller particles originally linked to the interlamellar matrix, may become part of the dissolved components.

However, it is unlikely that a collagen - like protein is the main source of the high proline fraction obtained after ultracentrifugation, as the major part of the fibrous protein collagen would be removed by ultracentrifugation. This is supported by the result that the presumed hydroxyproline peak was barely present in the chromatograms after ultracentrifugation.

Silk Fibroin-Like Protein: Besides the high proline and glycine levels, the alanine content was quite high ($\approx 8\%$) after each purification method. This may be considered as a further indicator for the suggested silk-like protein component in the interlamellar matrix, as silk fibroin has the dominant amino acids alanine, glycine and proline [Gatesy et al., 2001]. Previously, silk fibroin was proposed as a matrix component, because proteins with β -

¹⁴Due to the stirring of the solution and because of the CO_2 release.

sheet conformation (as silk fibroin) have been found by X-Ray diffraction studies of the interlamellar matrix [Weiner and Traub, 1980] on various mollusc shells. Furthermore, sequence patterns similar to silk fibroin were obtained by cleavage of proteins from the interlamellar matrix of the pearl oyster *Pinctada fucata* [Sudo et al., 1997].

Extraction Yields Using Different Methods: The amino acid composition was highly dependent on the purification method. It is unclear whether one of the compositions represents the protein composition of the soluble matrix as present during nacre growth. Different classes of proteins were enriched with the different purification methods.

So far, cation exchange chromatography has been the most successful method of nacre protein purification for *Haliotis*. In the amino acid analysis, the three most dominant amino acids after cation exchanger purification were Pro, Gly and Leu. This is well represented by the nacre proteins perlucin, perlustrin and perlwapin purified by this method¹⁵ as well as lustrin A, where these three amino acids are often among the three most dominant ones (compare table 2.3 on page 17).

The higher amount of potential acidic proteins binding to the C18 material indicates the presence of acidic proteins in the organic matrix. Furthermore, research showed that SDS - PAGE in combination with Coomassie Blue staining is not suitable to visualize acidic proteins and therefore this class of proteins might have been overlooked [Goldberg and Warner, 1997], [Gotliv et al., 2003]. This is also supported by the high Asx levels of about 22% found in *Haliotis rufescens* [Fu et al., 2005], [Nakahara et al., 1982].

The high content of unidentified material in the chromatograms without further protein specific purification was interesting (see figure 4.20). This indicates, that a large proportion of the soluble matrix are no proteins or peptides, which was also the finding of a recent investigation of the soluble matrix from nacre of the giant oyster *Pinctada margaritifera* [Bédouet et al., 2006]. Generally, little is known about the composition of the soluble matrix *in vivo*, especially about possible non-protein components, e.g., polysaccharides and small organic molecules. However, for the present work, the matrix preparation was performed with MWCO 3500 dialysis against acetic acid; therefore, only molecules with a molecular weight of at least a few kDa can be a possible source of the non-protein matter.

Published amino acid fractions for nacre of *Haliotis tuberculata* [Bédouet et al., 2001] and *Haliotis rufescens* [Nakahara et al., 1982], [Fu et al., 2005] also showed high fractions of glycine and alanine. However, high proline and leucine fractions, as observed here, were previously not reported. Nor could the reported Asx fractions of over 20% be reproduced with any of the preparation methods. The reason for this difference is unclear. In the cited works, powdered nacre was demineralized, whereas in this study, nacre pieces of a few mm size were used, which may result in a different matrix composition. As this is the first amino acid composition study for soluble matrix proteins of nacre from *Haliotis laevigata*, it is also possible that different species of *Haliotis* contain different matrix compositions. Just one

¹⁵At least as the initial purification step.

Table 4.5.: Amino acid compositions of soluble matrix fractions after different purification procedures. The values represent average molar fractions in %. The three most abundant amino acids are printed in bold letters. Cya corresponds to the cysteine content. Asx stands for Asp + Asn, Glx for Glu + Gln.

Amino acid	Ultra - centrifuge purified	Cation exchanger purified	C18 - ZipTip purified
Asx	1.0	4.6	14.1
Glx	2.9	5.7	6.5
Ser	3.7	6.2	5.9
Gly	11.7	8.6	13.3
His	2.0	2.0	6.9
Arg	1.0	3.1	2.5
Thr	6.1	6.9	3.7
Ala	8.1	8.0	8.5
Pro	24.7	13.8	9.4
Tyr	3.5	3.8	3.1
Val	4.2	5.7	4.4
Met	3.4	7.6	1.0
Ile	2.7	4.2	3.7
Leu	8.3	8.5	7.1
Phe	4.8	4.6	4.3
Trp	5.6	1.5	0.5
Lys	5.3	3.2	3.7
Cya	0.8	2.2	1.4

type of protein, which may be present in a greater or lesser extent in a species, could alter the amino acid compositions, when it is frequent enough.

Nevertheless, amino acid analysis of the nacre matrix yields very valuable information about matrix constituents, many of which are still unknown. Furthermore, it undelins the strong dependency of the composition of the soluble matrix. It must be clarified that the *in vivo* composition of the soluble matrix is unknown and the obtained solutions may partially contain components of the interlamellar matrix.

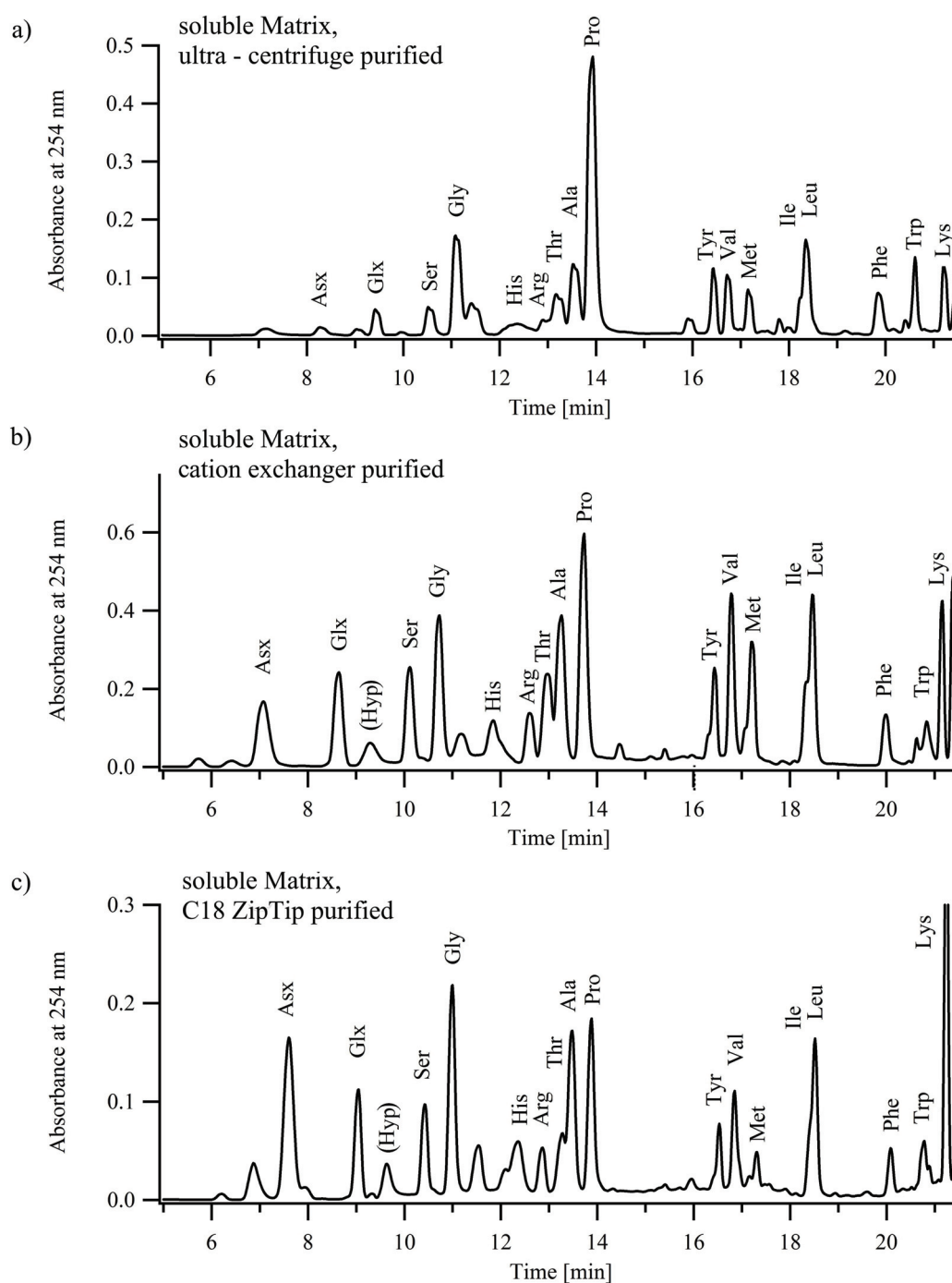


Figure 4.21.: Representative chromatograms of the PTC - amino acids obtained by hydrolysis of the soluble organic matrix extracted by demineralization of nacre with 6% acetic acid, 0.22 μm filtration and one of the following further purification steps: (a) Soluble matrix purified by ultra - centrifugation at 44000 rpm for 2 h. Proline and glycine contents were very high. (b) Soluble matrix purified by a cation exchanger. Fractions of Asx and Glx are only of average height. Proline and glycine fractions are high. (c) Soluble matrix purified using C18 ZipTips. Fractions of Asx and Glx are higher than with cation exchange purification. Again, proline and glycine levels are high, but proline is less pronounced. Hyp stands for a possible hydroxyproline peak.

5

Conclusion and Perspectives

Four main projects formed the basis of this thesis, an investigation of the growth and structure of nacre. Each project delivered highly interesting pieces of information and point out important directions for future research.

The most important result of this thesis was obtained through crystallization experiments on the interlamellar matrix. Following the development of a new and suitable crystallization method, it was clearly shown for the first time that the interlamellar matrix has a strong influence on several aspects of crystal growth. The obtained highly unusual crystals revealed, that morphology, polymorph and orientation of the obtained crystals were strongly influenced by the interlamellar matrix. Comparison with the crystallization on the matrix after protein digestion showed that proteins associated with the interlamellar matrix are responsible for laterally extended and flat crystal growth. However, even after proteinase-K digestion, the matrix was still capable of nucleating small mineral platelets, indicating the presence of nucleating centers of a different chemical nature.

It must be pointed out that the detailed mechanisms behind this ability are still not understood and warrant further investigation. As a first step in this direction, a future project might selectively remove or block components of the interlamellar matrix surface, for example, by using different proteinases or suitable antibodies. These organic matrices should then be investigated by using the double-diffusion crystallization method developed here. Last, but not least, a detailed analysis of the orientation of the flat crystal sheets should be performed, e.g., by TEM or X-ray diffraction.

A first step into a deeper understanding of the mechanisms behind favored nucleation and

flat crystal growth was performed by measuring the surface free energy of the interlamellar matrix by contact angle measurements. The determination of the surface free energy of the interlamellar matrix showed its slightly hydrophobic properties. Protein digestion revealed that these hydrophobic properties are caused by proteins of the interlamellar matrix. Furthermore, the idea was developed, that the flat crystal growth and favored nucleation on the interlamellar matrix is a result of suitable surface free energy components of the interlamellar matrix.

A new project targeting high precision measurements of the surface free energy has already begun. In this project, the surface free energy of the aragonite (001) surface and calcite surfaces will also be determined. This is a difficult task, since these high energy surfaces need special cleaning and a different contact angle setup. After determination of these values, an evaluation of the here developed hypothesis of a flat crystal growth, induced by suitable surface free energy components of the interlamellar matrix, will be possible.

For an integrated view on the mechanisms of nacre growth, it is necessary to include the influence of the soluble organic matrix on CaCO_3 crystallization. The challenging calculation of the precipitation rates from precipitation experiments allowed the first quantification of the influence of the soluble matrix proteins on CaCO_3 precipitation. By using this method at varying matrix protein concentrations and in comparison with unspecific proteins, the enormous specificity of nacre proteins on CaCO_3 could be shown.

Considering the crystallization experiments on the interlamellar matrix, the possible role of the soluble matrix may be the prevention of uncontrolled precipitation (possibly polymorph specific) as well as fine tuning crystal growth by inhibiting or enhancing specific faces of aragonite. However, the exact discrimination between the soluble matrix and the interlamellar matrix is not trivial, as they were obtained by dissolution of the mineral-organic composite nacre.

Further research should apply the presented assay, using purified or recombinant nacre proteins. The influence of each protein on crystallization may then be classified with more certainty. It would be very interesting to observe whether or not the contrastive behavior (enhancement at low concentrations and strong inhibition at high concentrations) reappears. If not, this effect was caused by the use of protein mixtures. Otherwise, the role of the proteins depends strongly on their concentration in the extrapallial fluid.

In order to improve the assay, the precipitation could be performed with starter crystals with defined surface area. Presumably, the deviations of the results would drop greatly, since the metastable crystal growth induction period is omitted and the nucleation surface is constant. For a deeper understanding of the detailed mechanisms of protein - crystal interaction, molecular dynamics simulations with nacre proteins and calcium carbonate crystals should be performed.

For a better characterization of soluble matrix proteins, an analysis of the amino acid

composition was performed. The initial motivation behind this project was the desire to investigate the discrepancy between published results indicating high contents of acidic amino acids in the soluble matrix and the low or average content of these residues in the purified proteins. It was surprising to see how dependent the results of the amino acid analysis were upon the method of matrix purification. The presence of high amounts of acidic residues could not be verified. It is unclear whether this is a special feature of the soluble matrix of *Haliotis laevigata*, which was with this study investigated for the first time. This should be further investigated. However, the importance of acidic residues may have been previously overemphasized.

It was interesting that indicators for a collagen-like protein were found: high contents of proline, glycine and possibly hydroxyproline, which occurs almost exclusively in collagen. The amino acid composition also supported a silk fibroin-like component. Both components were previously suggested constituents of the interlamellar matrix.

Again, it was shown, that the differentiation between soluble and interlamellar matrix is somewhat artificial and academic, since the components seem to overlap to some degree, due to the demineralization process. However, amino acid analysis is a tool which is useful for obtaining first information about a complex sample as a whole. A further application of the method might help to analyze the composition of the interlamellar matrix by investigating products of protein digests from the interlamellar matrix. This points out that more information about the organic matrix is necessary, and that special attention should be paid to the structure and composition *in vivo* during nacre growth, as demineralization might alter the constituent components.

Finally, it can be concluded that the advances in the understanding of biomineralization justify the dream that it will be possible to create new materials with superior properties in the near future.

Bibliography

- Adamson, A. W. (1990). *Physical Chemistry of Surfaces*. John Wiley and Sons Ltd., Hoboken, USA, 5. edition.
- Addadi, L., Joester, D., Nudelman, F., and Weiner, S. (2006). Mollusk shell formation: A source of new concepts for understanding biomineralization processes. *Chemistry. Eur. J.*, 12(4):980–987.
- Addadi, L. and Weiner, S. (1985). Interactions between Acidic Proteins and Crystals: Stereochemical Requirements in Biomineralization. *Proceedings of the National Academy of Sciences*, 82(12):4110–4114.
- Aimoli, C. G., Torres, M. A., and Beppu, M. M. (2006). Investigations into the early stages of *in vitro* calcification on chitosan films. *Materials Science & Engineering C*, 26(1):78–86.
- Akagi, T. and Kono, Y. (1995). Inhibiting effects of lanthanum ion on calcite formation from $\text{CaCl}_2\text{-NaHCO}_3$ solutions at 25° C. *Aquatic Geochemistry*, 1(2):231–239.
- Allwood, A. C., Walter, M. R., Burch, I. W., and Kamber, B. S. (2007). 3.43 billion-year-old stromatolite reef from the Pilbara Craton of Western Australia: Ecosystem-scale insights to early life on Earth. *Precambrian Research*, 158(3-4):198–227.
- Anthony, J. W., Bideaux, R. A., W., B. K., , and C., N. M. (1990). *Handbook of Mineralogy, Mineral Data Publishing*. the Mineralogical Society of America, Tucson Arizona, USA.
- Arnoldi, M. (2001). *Kraftmikroskopische Untersuchungen an biologischen Materialien*. PhD thesis, TU Munich, Biophysics Institute.
- Atkins, P. W. and De Paula, J. (2002). *Physical Chemistry*. Oxford University Press, New York, USA, 7. edition.
- Bajorath, J., Hinrichs, W., and Saenger, W. (1988). The enzymatic activity of proteinase K is controlled by calcium. *European Journal of Biochemistry*, 176(2):441–447.
- Barthelat, F., Tang, H., Zavattieri, P. D., Li, C. M., and Espinosa, H. D. (2007). On the mechanics of mother-of-pearl: A key feature in the material hierarchical structure. *Journal of the Mechanics and Physics of Solids*, 55(2):306–337.

- Becker, A., Becker, W., Marxen, J. C., and Epple, M. (2003). *In-vitro* Crystallization of Calcium Carbonate in the Presence of Biological Additives Comparison of the Ammonium Carbonate Method with Double-Diffusion Techniques. *Zeitschrift fuer anorganische und allgemeine Chemie*, 629(1213):2305–2311.
- Becker, A. and Epple, M. (2005). A high-throughput crystallization device to study biomineralization *in vitro*. In *Materials research society symposium proceedings*, volume 873, page 190. Warrendale, Pa.; Materials Research Society; 1999.
- Bédouet, L., José Schuller, M., Marin, F., Milet, C., Lopez, E., and Giraud, M. (2001). Soluble proteins of the nacre of the giant oyster *Pinctada maxima* and of the abalone *Haliotis tuberculata*: extraction and partial analysis of nacre proteins. *Comparative Biochemistry and Physiology, Part B*, 128(3):389–400.
- Bédouet, L., Rusconi, F., Rousseau, M., Duplat, D., Marie, A., Dubost, L., Le Ny, K., Berland, S., Péduzzi, J., and Lopez, E. (2006). Identification of low molecular weight molecules as new components of the nacre organic matrix. *Comparative Biochemistry and Physiology, Part B*, 144(4):532–543.
- Bjellqvist, B., Hughes, G. J., Pasquali, C., Paquet, N., Ravier, F., Sanchez, J. C., Frutiger, S., and Hochstrasser, D. (1993). The focusing positions of polypeptides in immobilized pH gradients can be predicted from their amino acid sequences. *Electrophoresis*, 14:1023–31.
- Blank, S., Arnoldi, M., Khoshnavaz, S., Treccani, L., Kuntz, M., Mann, K., Grathwohl, G., and Fritz, M. (2003). The nacre protein perlucin nucleates growth of calcium carbonate crystals. *Journal of Microscopy*, 212(3):280–291.
- Bradford, M. M. (1976). A rapid and sensitive method for the quantitation of microgram quantities of protein utilizing the principle of protein-dye binding. *Analytical Biochemistry*, 72(1-2):248–254.
- Brown, J. R. (1975). Structure of bovine serum albumin. *Fed. Proc.*, 34:2105.
- Canfield, R. E. (1963). The Amino Acid Sequence of Egg White Lysozyme. *Journal of Biological Chemistry*, 238(8):2698–2707.
- Chen, J. S., Lau, S. P., Tay, B. K., Chen, G. Y., Sun, Z., Tan, Y. Y., Tan, G., and Chai, J. W. (2001). Surface energy of amorphous carbon films containig iron. *Journal of Applied Physics*, 89(12):7814–7819.
- Cohen, S. A. and Strydom, D. J. (1988). Review: Amino acid analysis utilizing phenylisothiocyanate derivatives. *Analytical biochemistry*, 174(1):1–16.
- Compton, S. J. and Jones, C. G. (1985). Mechanism of dye response and interference in the Bradford protein assay. *Analytical Biochemistry*, 151(2):369–374.

- Crenshaw, M. A. (1972). The Inorganic Composition of Molluscan Extrapallial Fluid. *Biological Bulletin*, 143(3):506–512.
- Dong, M. W. (2006). *Modern HPLC for Practicing Scientists*. Wiley-Interscience, Hoboken, USA.
- Downs, R. T. (2006). The RRUFF Project: an integrated study of the chemistry, crystallography, Raman and infrared spectroscopy of minerals. Program and Abstracts of the 19th General Meeting of the International Mineralogical Association in Kobe, Japan. O03-13.
- du Noüy, P. L. (1919). A New Apparatus for Measuring Surface Tension. *The Journal of General Physiology*, 1(5):521–524.
- Ebeling, W., Henrich, N., Klockow, M., Metz, H., Orth, H., and Lang, H. (1974). Proteinase K from *Tritirachium album* Limber. *European Journal of Biochemistry*, 47(1):91–97.
- Ebert, R. F. (1986). Amino acid analysis by HPLC: Optimized conditions for chromatography of phenylthiocarbamyl derivatives. *Analytical Biochemistry*, 154(2):431–435.
- Edman, P. (1950). Method for determination of the amino acid sequence in peptides. *Acta Chem. Scand*, 4(283):34.
- Elhadj, S., de Yoreo, J. J., Hoyer, J. R., and Dove, P. M. (2006). Role of molecular charge and hydrophilicity in regulating the kinetics of crystal growth. *Proceedings of the National Academy of Sciences*, 103(51):19237.
- Falini, G., Fermani, S., and Ripamonti, A. (2002). Crystallization of calcium carbonate salts into beta-chitin scaffold. *Journal of Inorganic Biochemistry*, 91(3):475–480.
- Falini, G., Weiner, S., and Addadi, L. (2003). Chitin-Silk Fibroin Interactions: Relevance to Calcium Carbonate Formation in Invertebrates. *Calcified Tissue International*, 72(5):548–554.
- Feigl, F., Anger, V., and Koslow, R. H. (1973). Spot Tests in Inorganic Analysis. *Journal of The Electrochemical Society*, 120:261C.
- Fountoulakis, M. and Lahm, H. W. (1998). Hydrolysis and amino acid composition analysis of proteins. *Journal of Chromatography A*, 826(2):109–134.
- Fowkes, F. M. (1964). Attractive forces at interfaces. *Industrial and Engineering Chemistry*, 56(12):40–52.
- Fox, H. W. and Zisman, W. A. (1950). The Spreading of Liquids on Low-Energy Surfaces; I. Polytetrafluoroethylene. Technical report, NRL-3651, Naval Research Laboratory.

- Franke, J. and Mersmann, A. (1995). The influence of the operational conditions on the precipitation process. *Chemical Engineering Science*, 50(11):1737–1753.
- Fritz, M., Belcher, A. M., Radmacher, M., Walters, D. A., Hansma, P. K., Stucky, G. D., Morse, D. E., and Mann, S. (1994). Flat pearls from biofabrication of organized composites on inorganic substrates. *Nature*, 371(6492):49–51.
- Fu, G., Valiyaveetil, S., Wopenka, B., and Morse, D. E. (2005). CaCO₃ biomineralization: acidic 8-kDa proteins isolated from aragonitic abalone shell nacre can specifically modify calcite crystal morphology. *Biomacromolecules*, 6(3):1289–1298.
- Gatesy, J., Hayashi, C., Motriuk, D., Woods, J., and Lewis, R. (2001). Extreme Diversity, Conservation, and Convergence of Spider Silk Fibroin Sequences. *Science*, 291(5513):2603–2605.
- Gehrke, C. W., Sr. Wall, L. L., Absheer, J. S., Kaiser, F. E., and Zumwalt, R. W. (1985). Sample preparation for chromatography of amino acids: acid hydrolysis of proteins. *Journal of the Association of Official Analytical Chemists (USA)*, 68(5):811–821.
- Gehrke, N. (2006). *Retrosynthese von Perlmutter*. PhD thesis, University of Potsdam.
- Giles, R. (1995). Inorganic Overgrowth of Aragonite on Molluscan Nacre Examined by Atomic Force Microscopy. *The Biological Bulletin*, 188(1):8–15.
- Gindl, M., Sinn, G., Gindl, W., Reiterer, A., and Tschegg, S. (2001). A comparison of different methods to calculate the surface free energy of wood using contact angle measurements. *Colloids and Surfaces A: Physicochemical and Engineering Aspects*, 181(1-3):279–287.
- Goldberg, H. A. and Warner, K. J. (1997). The Staining of Acidic Proteins on Polyacrylamide Gels: Enhanced Sensitivity and Stability of Stains-All Staining in Combination with Silver Nitrate. *Analytical Biochemistry*, 251(2):227–233.
- Gotliv, B.-A., Addadi, L., and Weiner, S. (2003). Mollusk Shell Acidic Proteins: In Search of Individual Functions. *ChemBioChem*, 4:522–529.
- Gower, L. B. and Odom, D. J. (2000). Deposition of calcium carbonate films by a polymer-induced liquid-precursor (PILP) process. *Journal of Crystal Growth*, 210(719):734.
- Gries, K., Kröger, R., Kübel, C., Schowalter, M., Fritz, M., and Rosenauer, A. (2008). Correlation of the orientation of stacked aragonite platelets in nacre and their connection via mineral bridges. Accepted by Ultramicroscopy.
- Heinrikson, R. L. and Meredith, S. C. (1984). Amino acid analysis by reverse-phase high-performance liquid chromatography: Precolumn derivatization with phenylisothiocyanate. *Analytical Biochemistry*, 136(1):65–74.

- Hirayama, K., Akashi, S., Furuya, M., and Fukuhara, K. (1990). Rapid confirmation and revision of the primary structure of bovine serum albumin by ESIMS and Frit-FAB LC/MS. *Biochem Biophys Res Commun*, 173(2):639–46.
- Isogai, A. and Kato, Y. (1998). Preparation of Polyuronic Acid from Cellulose by TEMPO-mediated Oxidation. *Cellulose*, 5(3):153–164.
- Janssen, S. S. L., van Nispen, J. W., Melgers, P. A. T. A., van den Bogaart, H. W. M., and Hamelinck, R. L. A. E. (1986). HPLC analysis of phenylthiocarbamyl (PTC) amino acids. I. evaluation and optimization of the procedure. *Chromatographia*, 22(7):345–350.
- Kaelble, D. H. (1970). Dispersion-Polar Surface Tension Properties of Organic Solids. *The Journal of Adhesion*, 2(2):66–81.
- Kashchiev, D. and van Rosmalen, G. M. (2003). Review: Nucleation in solutions revisited. *Crystal Research and Technology*, 38(78):555–574.
- Kesava Reddy, G. and Enwemeka, C. S. (1996). A simplified method for the analysis of hydroxyproline in biological tissues. *Clinical Biochemistry*, 29(3):225–229.
- Khor, E., Wan, A. C., Tee, C. F., and Hastings, G. W. (1997). Reversible Water-Swellable Chitin Gel. *Journal of Polymer Science Part A: Polymer Chemistry*, 35(10):2049–2053.
- Kido, T. (1996). Identification of Calcitic and Aragonitic Otoconia by Selective Staining Methods. *Acta histochemica et cytochemica*, 29(2):121–127.
- Kitano, Y., Kanamori, N., and Yoshioka, S. (1976). Influence of chemical species on the crystal type of calcium carbonate. *The Mechanisms of Mineralization in the Invertebrates and Plants*.
- Krüss GmbH (2008). Selected literature values for surface free energy of solids. www.kruss.info/service/lit/surface_energy_solids_e.html.
- Levi-Kalisman, Y., Falini, G., Addadi, L., and Weiner, S. (2001). Structure of the Nacreous Organic Matrix of a Bivalve Mollusk Shell Examined in the Hydrated State Using Cryo-TEM. *Journal of Structural Biology*, 135(1):8–17.
- Lindsay, S. (1987). *High Performance Liquid Chromatography*. John Wiley and Sons Ltd., Hoboken, USA.
- Lottspeich, F. and Engels, J. W., editors (2006). *Bioanalytik*. Spektrum Akademischer Verlag, Heidelberg, Germany, 2. edition.
- Lowenstam, H. A. (1981). Minerals formed by organisms. *Science*, 211(4487):1126–1131.

- Mann, K., Siedler, F., Treccani, L., Heinemann, F., and Fritz, M. (2007). Perlinhibin, a Cysteine-, Histidine-, and Arginine-Rich Miniprotein from Abalone (*Haliotis laevigata*) Nacre, Inhibits In Vitro Calcium Carbonate Crystallization. *Biophysical Journal*, 93(4):1246.
- Mann, S. (1983). Mineralization in biological systems. *Struct. Bonding*, 54:125–174.
- Mann, S. (1988). Molecular recognition in biomineralization. *Nature*, 332(6160):119–124.
- Manneberg, M., Lahm, H. W., and Fountoulakis, M. (1995). Quantification of cysteine residues following oxidation to cysteic acid in the presence of sodium azide. *Analytical Biochemistry*, 231(2):349–353.
- Marin, F. and Luquet, G. (2004). Molluscan shell proteins. *Comptes rendus-Palevol*, 3(6-7):469–492.
- Markov, I. V. (2003). *Crystal Growth for Beginners: Fundamentals of Nucleation, Crystal Growth and Epitaxy*. World Scientific Publishing Company, River Edge, USA.
- Meigen, W. (1902). Beiträge zur Kenntniss des kohlensauren Kalkes. *Berichte der Naturforschenden Gesellschaft zu Freiburg im Breisgau*.
- Metzler, R. A., Abrecht, M., Olabisi, R. M., Ariosa, D., Johnson, C. J., Frazer, B. H., Coppersmith, S. N., and Gilbert, P. (2007). Architecture of Columnar Nacre, and Implications for Its Formation Mechanism. *Physical Review Letters*, 98(26):268102.
- Meyers, M. A., Lin, A. Y. M., Chen, P. Y., and Muyco, J. (2008). Mechanical strength of abalone nacre: Role of the soft organic layer. *Journal of the Mechanical Behavior of Biomedical Materials*, 1(1):76–85.
- Michenfelder, M., Fu, G., Lawrence, C., Weaver, J. C., Wustman, B. A., Taranto, L., Evans, J. S., and Morse, D. E. (2003). Characterization of two molluscan crystal-modulating biomineralization proteins and identification of putative mineral binding domains. *Biopolymers*, 70(4):522–533.
- Nakahara, H. (1979). An electron microscope study of the growing surface of nacre in two gastropode species *Turbo cornutus* and *Tegula pfeifferi*. *Venus*, 38:205–211.
- Nakahara, H., Bevelander, G., and Kakei, M. (1982). Electron microscopic and amino acid studies on the outer and inner shell layers of *Haliotis rufescens*. *Venus*, 41(1):33–46.
- Nudelman, F., Gotliv, B. A., Addadi, L., and Weiner, S. (2006). Mollusk shell formation: Mapping the distribution of organic matrix components underlying a single aragonitic tablet in nacre. *Journal of Structural Biology*, 153(2):176–187.
- Ogino, T., Suzuki, T., and Sawada, K. (1987). The formation and transformation mechanism of calcium carbonate in water. *Geochimica et Cosmochimica Acta*, 51(10):2757–2767.

- Owens, D. K. and Wendt, R. C. (1969). Estimation of the surface free energy of polymers. *Journal of Applied Polymer Science*, 13:1741–1747.
- Parkhurst, D. L. and Appelo, C. A. J. (1999). User's guide to PHREEQC (version 2)—A computer program for speciation, batch-reaction, one-dimensional transport, and inverse geochemical calculations. *U.S. Geological Survey Water-Resources Investigations Report*, (4259).
- Plummer, L. N. and Busenberg, E. (1982). The solubilities of calcite, aragonite and vaterite in CO₂-H₂O solutions between 0° and 90° C, and an evaluation of the aqueous model for the system CaCO₃-CO₂-H₂O. *Geochimica et Cosmochimica Acta*, 46(6):1011–1040.
- Schaeffer, T. E., Ionescu-Zanetti, C., Proksch, R., Fritz, M., Walters, D. A., Almqvist, N., Zaremba, C. M., Belcher, A. M., Smith, B. L., Stucky, G., Morse, D., and P., H. (1997). Does Abalone Nacre Form by Heteroepitaxial Nucleation or by Growth through Mineral Bridges? *Chemistry of Materials*, 9:1731–1740.
- Shen, X., Belcher, A. M., Hansma, P. K., Stucky, G. D., and Morse, D. E. (1997). Molecular Cloning and Characterization of Lustrin A, a Matrix Protein from Shell and Pearl Nacre of *Haliotis rufescens*. *Journal of Biological Chemistry*, 272(51):32472–32481.
- Smith, R. and Pitrola, R. (2000). Influence of casting substrate on the acid-base interaction energies of various polyesters. *Polymer*, 41(26):9111–9122.
- Soby, L. M. and P., J. (1981). Determination of asparagine and glutamine in polypeptides using bis(1,1-trifluoroacetoxy)iodobenzene. *Analytical biochemistry*, 113:149–153.
- Söhnel, O. and Mullin, J. W. (1982). Precipitation of calcium carbonate. *Journal of Crystal Growth*, 60(2):239–250.
- Sudo, S., Fujikawa, T., Nagakura, T., Ohkubo, T., Sakaguchi, K., Tanaka, M., Nakashima, K., and Takahashi, T. (1997). Structures of mollusc shell framework proteins. *Nature*, 387(6633):563–4.
- Treccani, L. (2006). *Protein-Mineral Interaction of Purified Nacre Proteins with Calcium Carbonate Crystals*. PhD thesis, University of Bremen.
- Treccani, L., Mann, K., Heinemann, F., and Fritz, M. (2006). Perlwapin, an Abalone Nacre Protein with Three Four-Disulfide Core (Whey Acidic Protein) Domains, Inhibits the Growth of Calcium Carbonate Crystals. *Biophysical Journal*, 91(7):2601.
- Truesdell, A. H. and Jones, B. F. (1974). WATEQ, A computer program for calculating chemical equilibria of natural waters. *U.S. Geological Survey Water-Resources, J. Res.*, 2:233–248.

- van Cappellen, P. (2003). Biomineralization and Global Biogeochemical Cycles. *Reviews in Mineralogy and Geochemistry*, 54(1):357–381.
- van Oss, C. J., Good, R. J., and Chaudhury, M. K. (1988). Additive and nonadditive surface tension components and the interpretation of contact angles. *Langmuir*, 4(4):884–891.
- Volkmer, D., Harms, M., Gower, L., and Ziegler, A. (2005). Morphosynthese lamellierter perlmuttartiger CaCO_3 -Duennfilme und-Beschichtungen. *Angewandte Chemie*, 117(4):645–650.
- Wang, L., Sondi, I., and Matijević, E. (1999). Preparation of Uniform Needle-Like Aragonite Particles by Homogeneous Precipitation. *Journal of Colloid and Interface Science*, 218(2):545–553.
- Weiner, S. and Traub, W. (1980). X-ray diffraction study of the insoluble organic matrix of mollusk shells. *FEBS Lett*, 111:311–316.
- Weiner, S., Traub, W., and Parker, S. B. (1984). Macromolecules in Mollusc Shells and Their Functions in Biomineralization. *Philosophical Transactions of the Royal Society of London. Series B, Biological Sciences (1934-1990)*, 304(1121):425–434.
- Weiss, I. M., Göhring, W., Fritz, M., and Mann, K. (2001). Perlustrin, a *Haliotis laevigata* (Abalone) Nacre Protein, Is Homologous to the Insulin-like Growth Factor Binding Protein N-Terminal Module of Vertebrates. *Biochemical and Biophysical Research Communications*, 285(2):244–249.
- Weiss, I. M., Kaufmann, S., Mann, K., and Fritz, M. (2000). Purification and Characterization of Perlucin and Perlustrin, Two New Proteins from the Shell of the Mollusc *Haliotis laevigata*. *Biochemical and Biophysical Research Communications*, 267(1):17–21.
- Weiss, I. M., Renner, C., Strigl, M. G., and Fritz, M. (2002). A Simple and Reliable Method for the Determination and Localization of Chitin in Abalone Nacre. *Chemistry of Materials*, 14(8):3252–3259.
- Wheeler, A. P., George, J. W., and Evans, C. A. (1981). Control of Calcium Carbonate Nucleation and Crystal Growth by Soluble Matrix of Oyster Shell. *Science*, 212(4501):1397–1398.
- Wilhelmy, L. (1863). Ueber die Abhängigkeit der Capillaritäts-Constanten des Alkohols von Substanz und Gestalt des benetzten festen Körpers. *Annalen der Physik*, 195(6):177–217.
- Wu, S. (1973). Polar and Nonpolar Interactions in Adhesion. *The Journal of Adhesion*, 5(1):39–55.
- Zaremba, C. M., Belcher, A. M., Fritz, M., Li, Y., Mann, S., Hansma, P. K., Morse, D. E., Speck, J. S., and Stucky, G. D. (1996). Critical Transitions in the Biofabrication of Abalone Shells and Flat Pearls. *Chemistry of Materials*, 8:679–690.

-
- Żenkiewicz, M. (2007). Comparative study on the surface free energy of a solid calculated by different methods. *Polymer Testing*, 26(1):14–19.
- Zhang, F., Wolf, G. K., Wang, X., and Liu, X. (2001). Surface properties of silver doped titanium oxide films. *Surface and Coatings Technology*, 148(1):65–70.



Appendix

A.1. Determination of the Organic Fraction

Introduction

Many articles about nacre contain an introductory statement about the fraction of organic matter in nacre, and how dramatically this small fraction influences the growth of the material as well as its mechanical properties. The fraction of organic matter included in abalone nacre is usually given as approximately 2-5% (e.g. [Levi-Kalisman et al., 2001], [Weiss et al., 2000]), but without description of the determination. Furthermore, the interesting distinction between the fractions of soluble and insoluble matrix components is not made. In order to verify the data and to obtain distinct values for the soluble and insoluble fractions, a determination of both matrix fractions in nacre of *Haliotis laevis* was performed.

Materials and Methods

Preparation of Nacre Pieces

Shells of *Haliotis laevis* (obtained from Abalone Exports, Laverton North, Australia) were precleaned with a brush. Calcitic outer parts of the shells were removed by blasting with corundum slurry (Al_2O_3 , diameter 0.12-0.25 mm; slurry blaster WA70, Sigg, Jestetten, Germany). Surface contaminations were cleaned from the nacreous shells by oxidation in a solution of 50% sodiumhypochlorite (NaOCl) for 2 min. Hypochlorite and dissolved organic compounds were removed by extensive washing with ultrapure water. After drying, the nacre pieces were crushed with a jaw crusher (Pulverisette, equipped with ZrO_2 crushing jaws, Fritsch, Idar-Oberstein, Germany), resulting in pieces of up to 5 mm edge length. Finally, the nacre pieces were weighed.

Demineralization of Nacre

The weighed nacre pieces were demineralized by dialysis (MWCO 3500) against 6% acetic acid containing 0.02% NaN_3 . The dialysis solution contained typically 3 l and was changed daily for a week until complete demineralization was achieved. After demineralization, the organic material in the dialysis tubes was dialyzed three times against 10 mM NaHCO_3 containing 0.02% NaN_3 . Beakers containing the dialysis tubes were stirred and kept at 4° C during the whole process.

Fractionation of Organic Matrix

In a first step, soluble and insoluble matrix compounds were roughly separated by sieving. The solution which passed through the sieve was centrifuged at 4000 rpm for 10 min at 4° C. The resulting pellet was added to the insoluble fraction.

Mass determination

Insoluble organic compounds were dried at 50° C on a weighed bowl over night. Afterwards, the mass of the dried insoluble organic matrix could be determined by weighing the filled bowl. The concentration of the protein component in the soluble organic matrix was determined with the Bradford method (see section 3.2.1). By accurately measuring the final volume of the demineralization dialysis solution, it was possible to obtain the protein fraction of the soluble matrix.

Results and Discussion

The determined organic fractions of the nacreous layer from *Haliotis laevis* after demineralization by acetic acid were as follows¹:

- **Interlamellar (insoluble) matrix:** 3.5% (1.6%)
- **Protein fraction of the soluble matrix:** 0.022% (0.023%)

The values in brackets correspond to a determination in a follow-up project performed by Stella Kocanis at the Biophysics Institute, University of Bremen. The most likely reason for the difference in the insoluble fraction is that Ms. Kocanis used only thin parts of the shell, whereas for the present study, the whole shell was used. The determined total fraction of 1.6% - 3.5% is in tolerable agreement with the values of 2-5% given in the literature (e.g. [Levi-Kalisman et al., 2001], [Weiss et al., 2000]).

For a typical shell, containing 150 g nacre, above values correspond to 5.25 g interlamellar matrix (2.4 g for the lower value) and about 33 mg of soluble matrix protein.

It must be noted, that the distinction in soluble and insoluble matrix is somewhat artificial, and the obtained fractions may depend on the size of nacre pieces during demineralization. Smaller pieces, e.g., a powder, may yield higher values for the soluble fraction, as it is likely that not all matrix constituents are strongly linked to the interlamellar matrix layers.

¹Average of two independent determinations, which resulted in almost identical fractions.

A.2. Work for Heterogeneous and Homogeneous Nucleation

In this section, a brief description of a simple model to express the nucleation work and the critical nucleus size in solutions, or on surfaces, is given. For a more detailed description, please see [Kashchiev and van Rosmalen, 2003]. The main target of this section is to introduce the expression for the critical nucleus size for the nucleation on a substrate.

The driving force for nucleation (e.g. a CaCO_3 crystal) from solution is supersaturation. This can be expressed as a difference in the chemical potentials of the dissolved (μ_s) and the nucleated phase (μ_c):

$$\Delta\mu = \mu_s - \mu_c \quad (\text{A.1})$$

The difference in chemical potential can be described using supersaturation S^2 :

$$\Delta\mu = k_B T \ln S \quad (\text{A.2})$$

When the solution is supersaturated, nuclei will form. However, the newly formed nuclei will create a new interface, containing a specific interfacial free energy. In general, the work W , to form a nucleus of n particles from a solution with saturation S , can be written as:

$$W(n) = -nk_B T \ln S + \Phi(n) \quad (\text{A.3})$$

The term $\Phi(n)$ denotes the work to create the new interface and must be treated differently for *homogeneous* nucleation and *heterogeneous* nucleation (see figure A.1 (a), (b)). In the classical nucleation theory, the homogeneous nucleation of a spherical particle is considered. Hence, the work to create the surface can be expressed by $\Phi(n) = A\gamma$, given by the area of the sphere A and the surface free energy γ . After defining ν_0 , the average volume occupied by one molecule, this can be used to express the work to form a nuclei of size n in the following manner:

$$W(n) = -nk_B T \ln S + (36\pi\nu_0^2)^{1/3}\gamma n^{2/3} \quad (\text{A.4})$$

For the first few particles, the work is positive, since the surface “cost” is larger than the “win” due to the formation of crystal volume. But since the number of particles in the volume increases faster ($\propto n$) than the number exposed at the surface ($\propto n^{2/3}$), the work will decrease (compare figure A.1 (c)), after reaching a critical size n^* . The critical size n^* explains the occurrence of so called metastable solutions with $S > 1$, which do not form precipitate for a long time. At low supersaturations, it is very unlikely for nuclei to cross the energy barrier W^* , required to create a nucleus of size n^* .

By finding the extremum of $W(n)$, $0 = (dW/dn)_{n=n^*}$, the expression for the critical size

² $S = [Ca^{2+}][CO_3^{2-}]/[Ca^{2+}]_{eq}[CO_3^{2-}]_{eq}$, where the denominator denotes the product of maximal soluble concentrations.

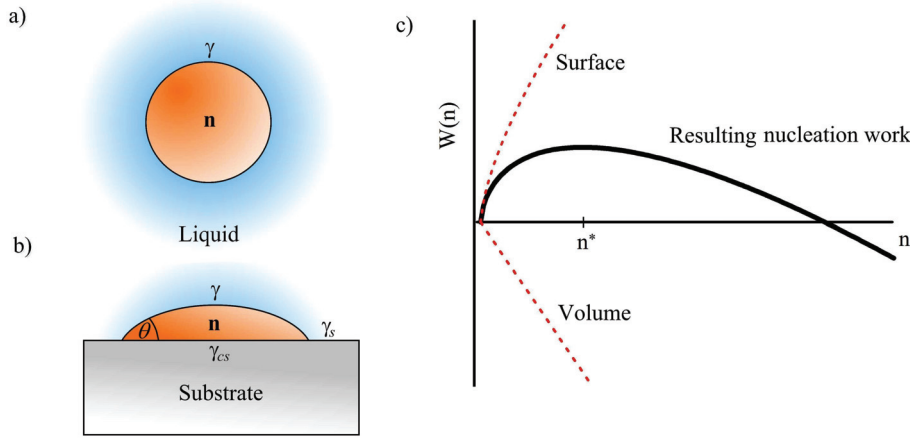


Figure A.1.: (a) Homogeneous nucleation of a spherical particle in a solution. (b) Heterogeneous nucleation of a spherical, cap shaped nuclei on a substrate with contact angle θ . (c) Illustrative plot of the nucleation work $W(n)$ to form a nucleus of n particles. $W(n)$ is the sum of a surface term $\propto n^{2/3}$ and a volume term $\propto -n$. The critical size n^* , corresponds to an energy barrier to form stable nuclei. The work for nucleating on surface is always lower or equal to the homogeneous case. Adapted from [Kashchiev and van Rosmalen, 2003].

n^* in homogeneous nucleation is obtained:

$$n^* = 32\pi\nu_0^2\gamma^3/3(k_B T)^3 \ln^3 S \quad (\text{A.5})$$

As for the homogeneous case, the expression for heterogeneous nucleation of a spherical cap on a substrate is obtained by starting from equation A.3 and with the use of the expression for the supersaturation (equation A.2). Then, the work to create the newly formed surface $\Phi(n)$ can be expressed almost identically to equation A.4 for the homogeneous nucleation, with the difference that an effective surface free energy γ_{eff} is used. This effective surface free energy considers the facts that the exposed surface in heterogeneous nucleation is smaller and that a new interface with the substrate is formed. γ_{eff} can be calculated from the surface free energy of the nuclei γ and the contact angle θ :

$$\gamma_{eff} = \Psi^{1/3}(\theta)\gamma \quad (\text{A.6})$$

The function $\Psi(\theta)$ increases monotonously³ from $\Psi = 0$ for $\theta = 0$ to $\Psi = 1$ for $\theta = 180^\circ$. By using γ_{eff} , an expression for the critical size in heterogeneous nucleation can be obtained:

$$n^* = 32\pi\nu_0^2\gamma_{eff}^3/3(k_B T)^3 \ln^3 S \quad (\text{A.7})$$

This is identical to the expression for n^* in the case of homogeneous nucleation, with the only difference that $\gamma_{eff} \leq \gamma$. Therefore, in almost all cases, nucleation on a surface is energetically favored.

³ $\Psi(\theta) = \frac{1}{4}(2 + \cos\theta)(1 - \cos\theta)^2$, for a derivation see [Markov, 2003]

A.3. Double-Diffusion Box

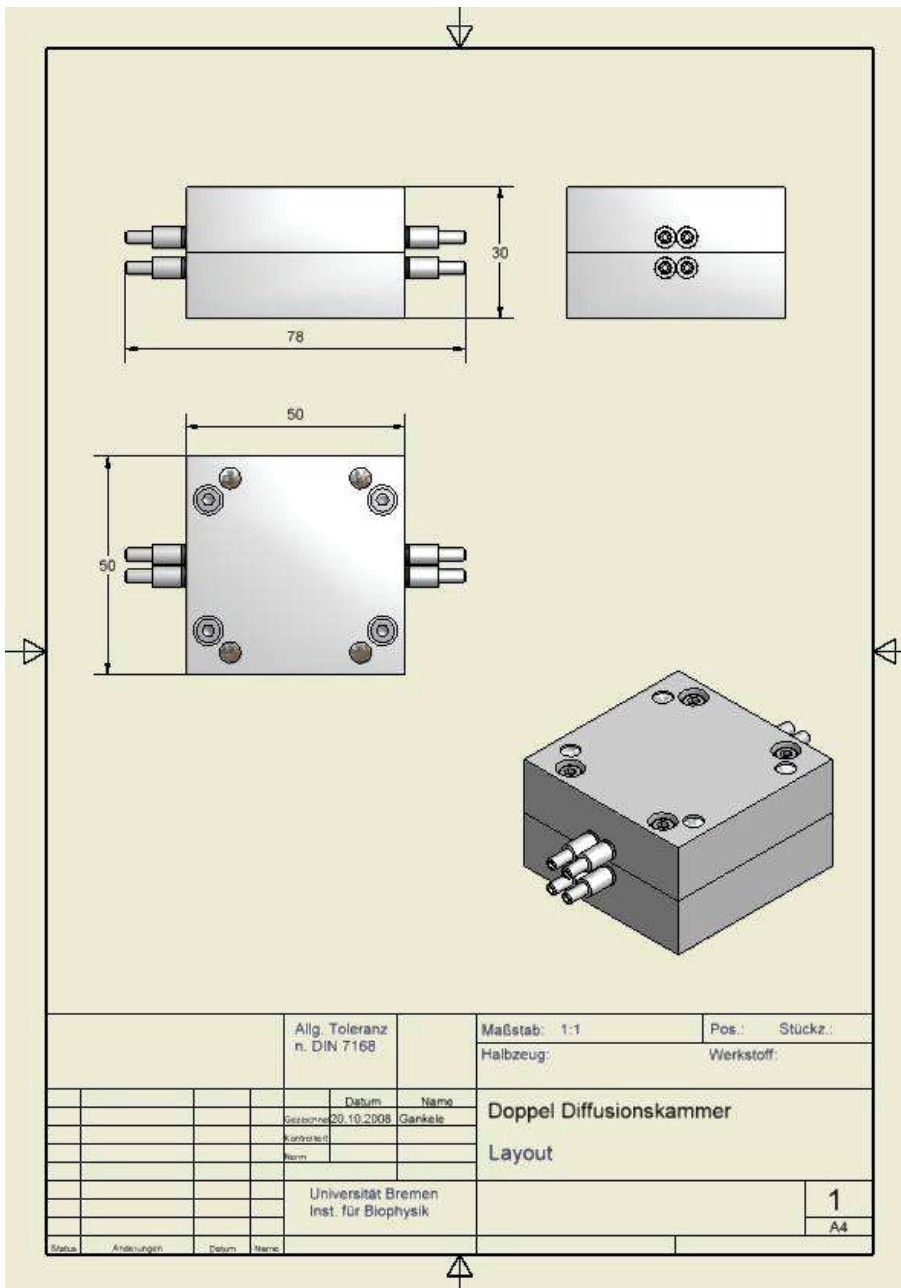


Figure A.2.: Double-diffusion box: Overview. Drawing by Gerd Ankele, University of Bremen.

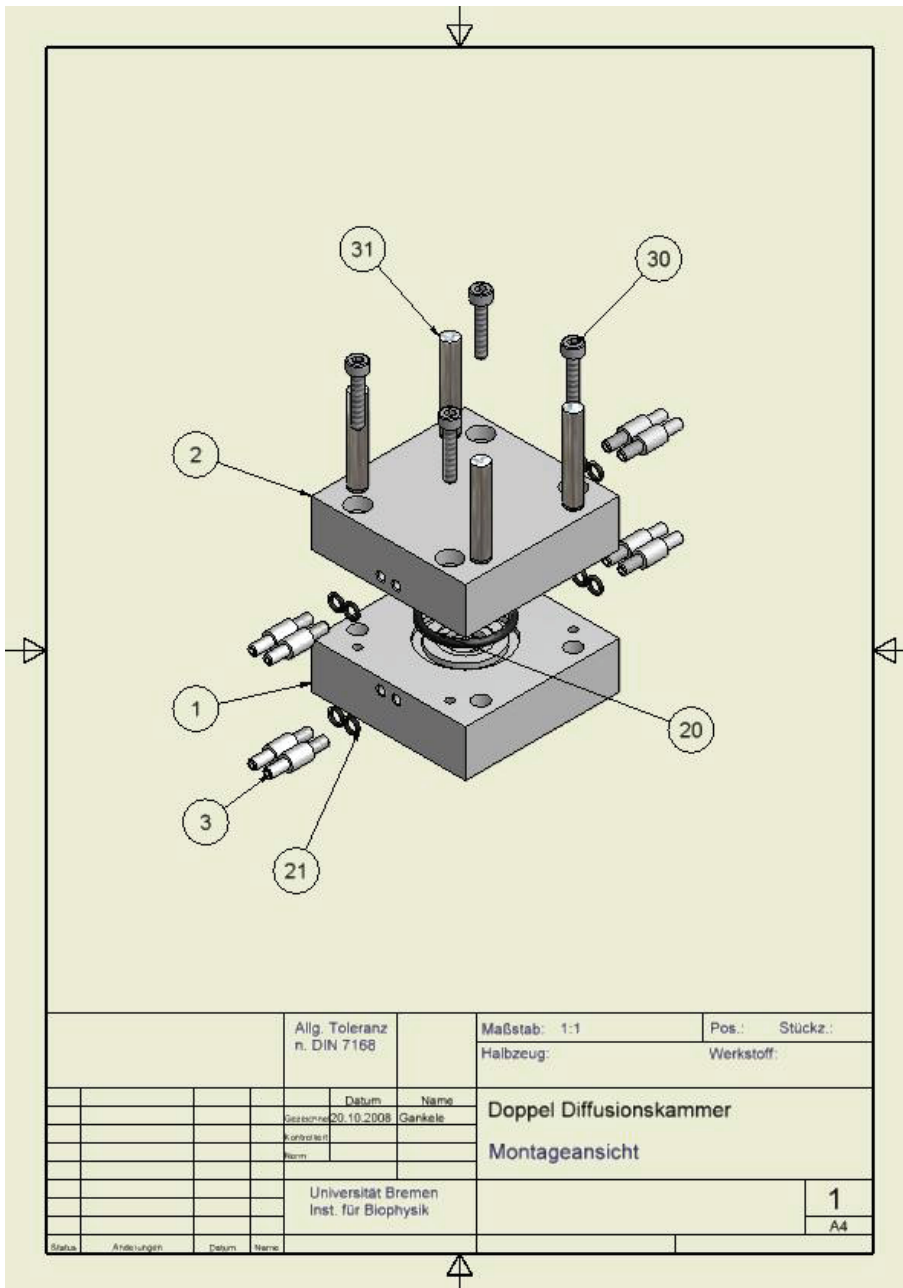


Figure A.3.: Double-diffusion box: Assembly. Drawing by Gerd Ankele, University of Bremen.

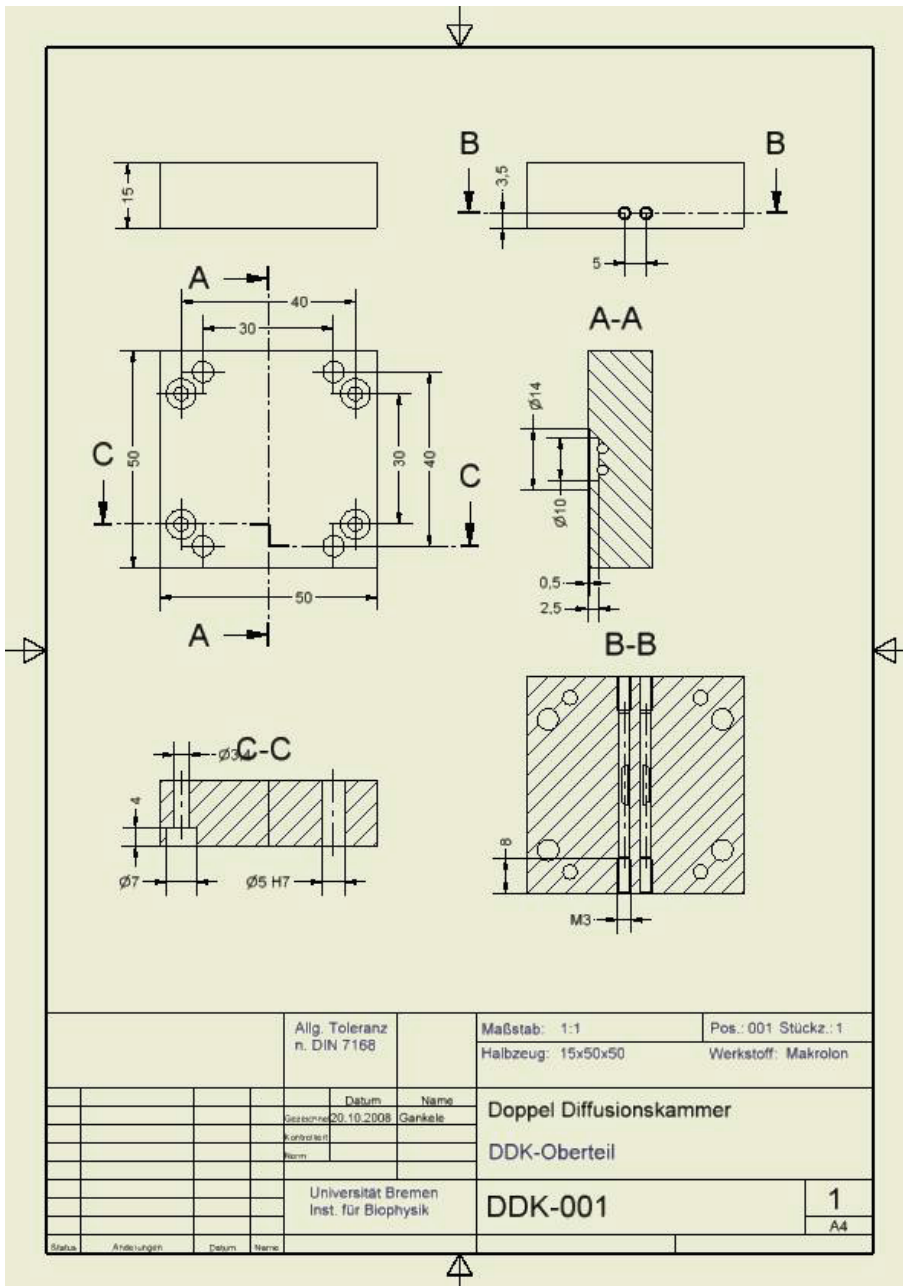


Figure A.4.: Double-diffusion box: Top side. Drawing by Gerd Ankele, University of Bremen.

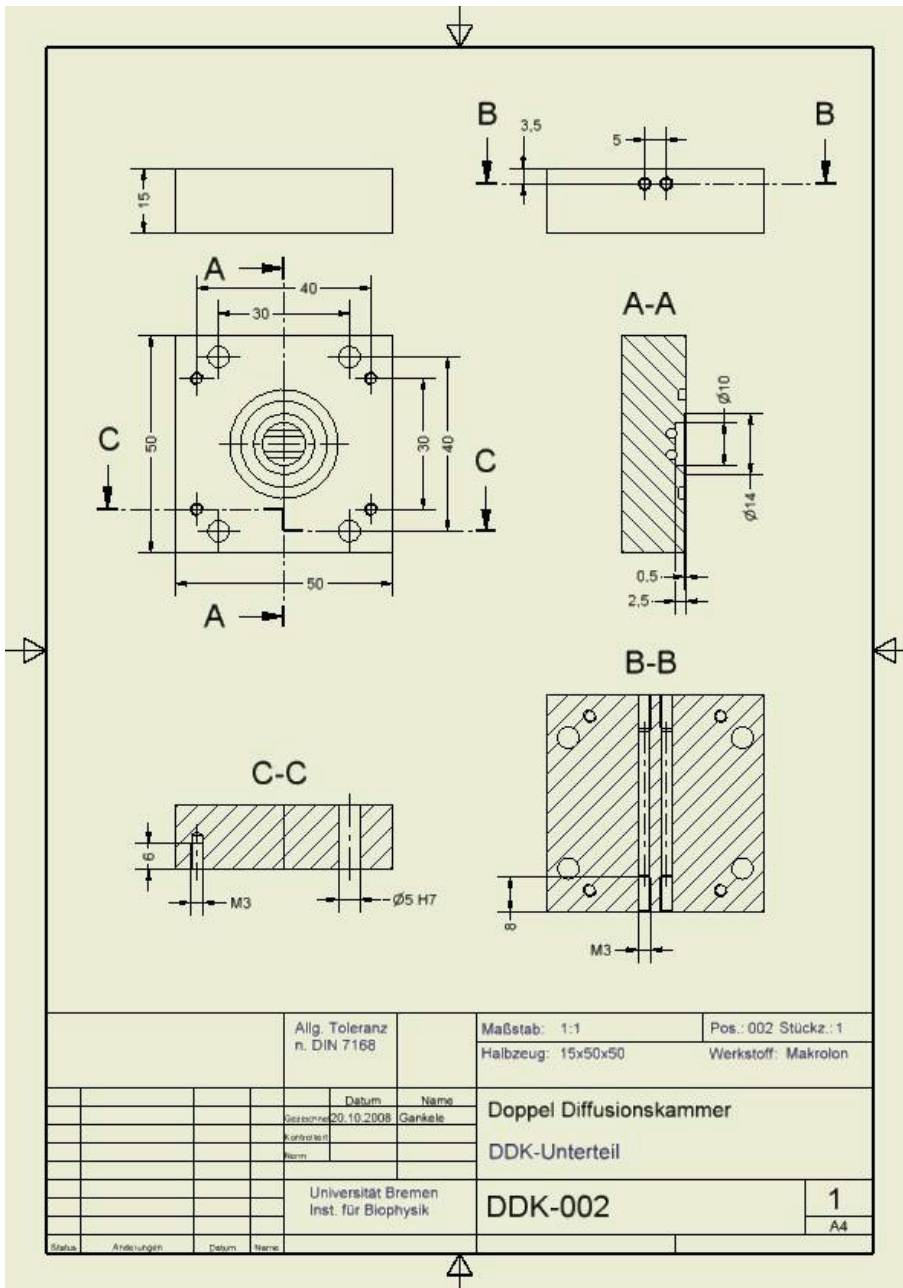


Figure A.5.: Double-diffusion box: Bottom side. Drawing by Gerd Ankele, University of Bremen.

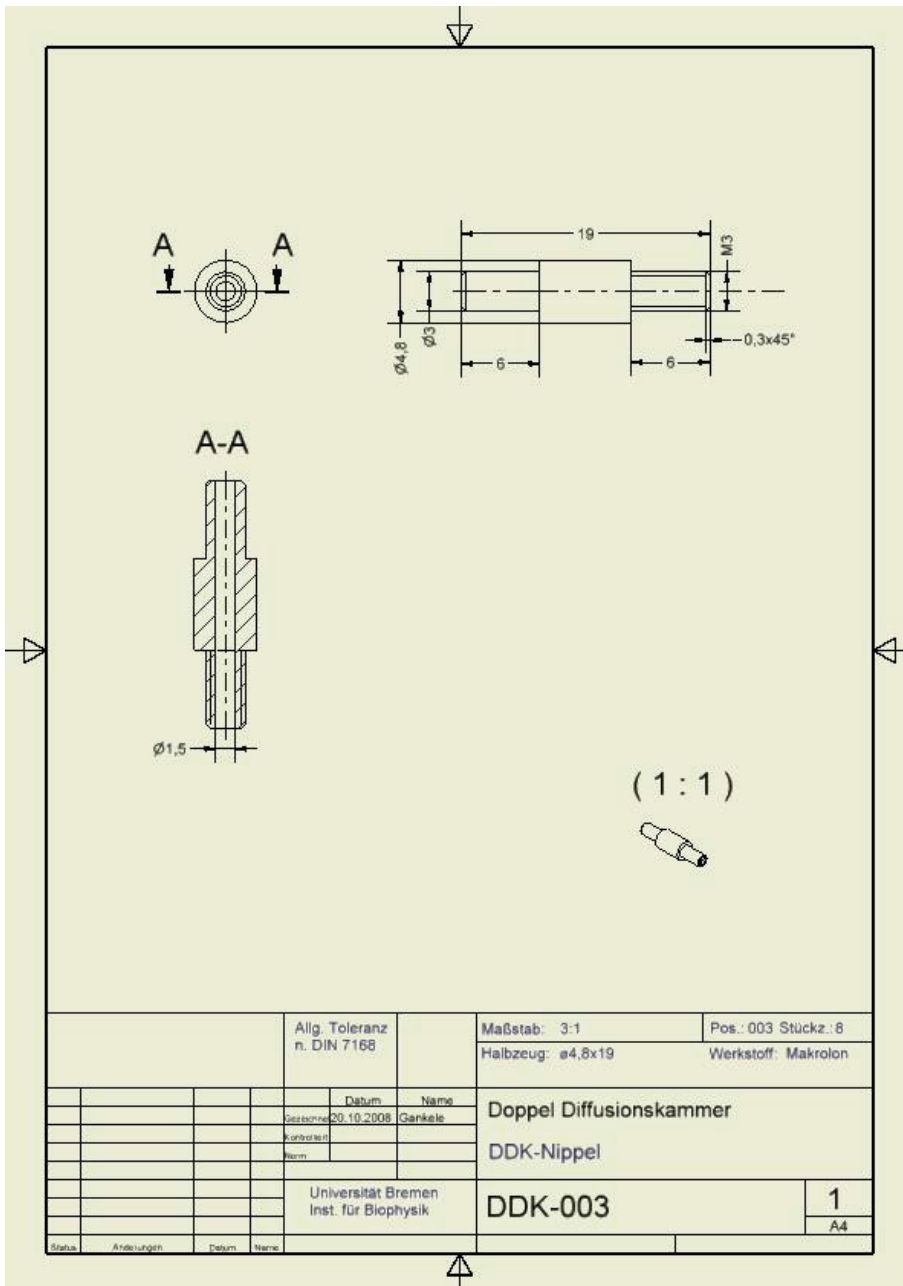
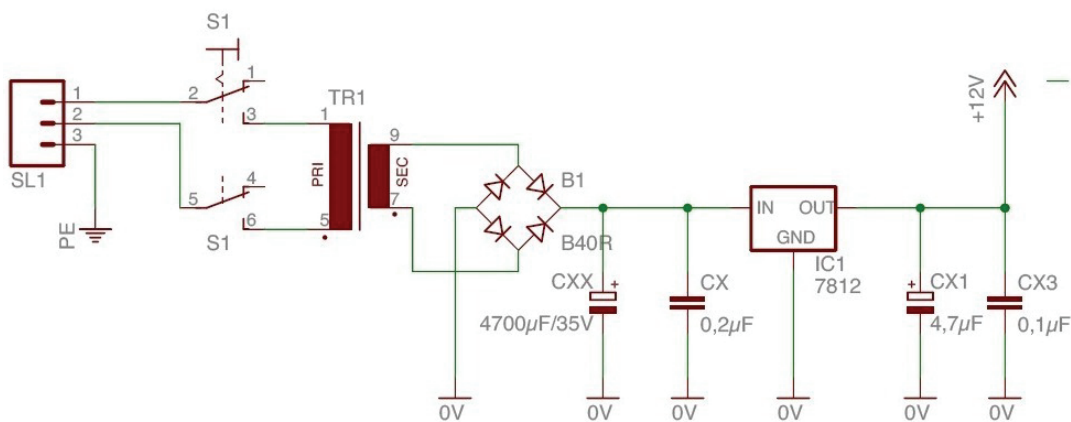


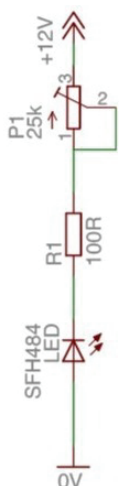
Figure A.6.: Double-diffusion box: Tube fitting. Drawing by Gerd Ankele, University of Bremen.

A.4. Self-Made Turbidity Sensor

Power supply



IR - sender



IR - receiver

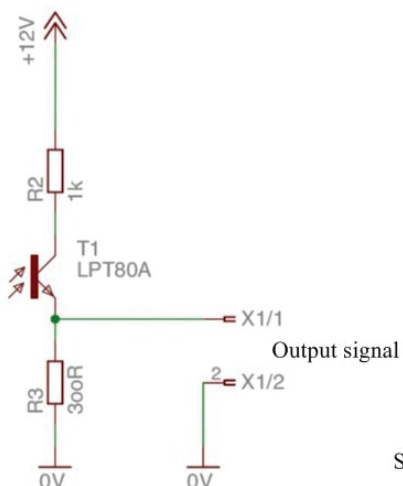


Figure A.7.: Circuit diagram of the components for the self - made IR - sensor and a photograph of the sensor unit. Circuit diagram drawings were kindly provided by Holger Doschke, Biophysics Institute, University of Bremen.

A.5. Bradford Assay Calibration

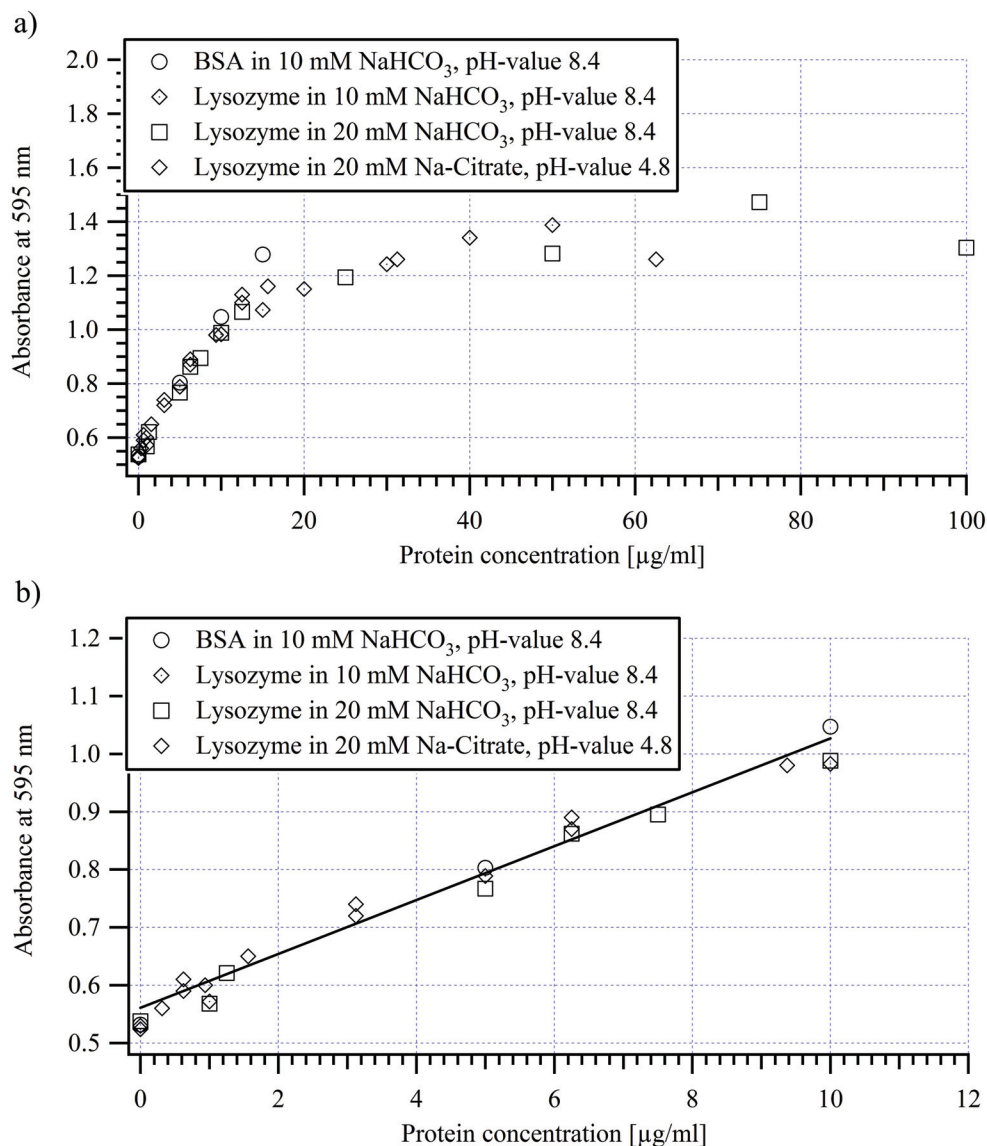


Figure A.8.: Calibration plots using the Bradford microassay for protein concentration determination [Bradford, 1976]. Not corrected for blank. Each data point represents the average of at least two measurements. The overview plot (a) shows, that the response of the assay is nonlinear, when using concentrations over $\approx 15 \mu\text{g/ml}$. (b) Calibration plot in the secure interval 0-10 $\mu\text{g/ml}$. Equation of the linear calibration fit: $A = 0.047\text{ml}/(\mu\text{g})c + 0.5611$.

A.6. Abbreviations

AFM	Atomic force microscope
BSA	Bovine serum albumin
BTI	[bis(trifluoroacetoxy)iodo]benzene
C4	Butyl functionalized silica for RP-HPLC
C18	Octadecyl
DMF	Dimethylformamide
DMSO	Dimethylsulfoxide
HPLC	High performance liquid chromatography
LC	Liquid chromatography
MWCO	Molecular weight cut-off
ODS - 2	Octadecylsilane
pI	Isoelectric point
PITC	Phenylisothiocyanate
PTC	Phenylthiocarbonyl
RP - HPLC	Reversed phase HPLC
rpm	rounds per minute
SDS - PAGE	sodium dodecyl sulfate polyacrylamide gel electrophoresis
SEM	Scanning electron microscopy
TEA	Triethylamine
TEM	Transmission electron microscope
TFA	Trifluoroacetic acid
UV	Ultra violet light spectrum
VIS	Visible light spectrum
XRD	X - ray diffraction

A.7. List of Manufacturers

A.7.1. Equipment

Analog to digital board	National Instruments, Austin, USA
Cation exchanger column	HiTrap-CM sepharose fast flow, Amersham Biosciences, Piscataway, USA
Centrifuge	Sorvall SS 34, Thermo Fisher, Waltham, USA
HPLC Column	4.6 x 150 mm Spherisorb ODS-2 C-18 3 μm particle diameter, 150 Å pore width, MZ-Analysentechnik, Mainz, Germany
HPLC Column inlet filter	Rheodyne 7335, IDEX HS, Oak Harbor, USA
HPLC - Main unit	Model 600, Waters, Eschborn, Germany
HPLC - UV VIS Detector	Model 2487, Waters, Eschborn, Germany
IGORPro (scientific software)	WaveMetrics, Portland, USA
Jaw crusher	Pulverisette, equipped with ZrO ₂ crushing jaws, Fritsch, Idar-Oberstein, Germany
LC System	Gradifrac, Amersham Biosciences, Piscataway, USA
Ultracentrifuge	LE-80K, Beckman Coulter, Fullerton, USA
pH - Electrode	WTW SenTix Mic, Weilheim, Germany
pH - Meter	PP-20, Sartorius, Göttingen, Germany
Rotary evaporator	Savant Speed Vac SPD121 P, Thermo Fisher, Waltham, USA
Scanning electron microscope	Camscan Series 2, Cambridge Instruments, Cranberry Township, USA
Slurry blaster	WA70, Sigg, Jestetten, Germany
Sputter coater	K550, Emitech, Montigny, France
UV-VIS spectrometer	Perkin-Elmer, Waltham, USA
Water purification	Milli - Q Academic, Millipore, Billerica, USA
XRD System	Seifert, General electrics inspection technologies, Lewistown, USA

A.7.2. Chemicals and Consumables

Amino acid standard A 2908	Sigma Aldrich, Saint Louis, USA
Protein Assay	Bio-Rad, Hercules, USA
BSA	A9418, Sigma Aldrich, Saint Louis, USA
C18 ZipTip	Millipore, Billerica, USA
One way PMMA cuvettes	Plastibrand, Brand, Wertheim, Germany
Dialysis Tubes	MWCO 3500 and 6-8000, SpectraPor3, Spectrum Laboratorys, Rancho Dominguez, USA
Lysozyme	L 6876, Sigma Aldrich, Saint Louis, USA
Proteinase - K	Molecular Probes, Carlsbad, USA
Paraffin wax	Melting point 51-53 °C, Merck, Darmstadt Germany

Other chemicals were purchased in the purity p.a. or higher.

A.8. Own publications

1. Treccani, L., Mann, K., **Heinemann, F.**, Fritz, M. 2006. Perlwapin, an Abalone Nacre Protein with Three Four-Disulfide Core (Whey Acidic Protein) Domains, Inhibits the Growth of Calcium Carbonate Crystals. *Biophysical Journal*, 91(7), 2601.
2. **Heinemann, F.**, Treccani, L., Fritz, M. 2006. Abalone nacre insoluble matrix induces growth of flat and oriented aragonite crystals. *BBRC*, 344, 45-49.
3. Mann, K., Siedler, F., Treccani, L., **Heinemann, F.**, Fritz, M. 2007. Perlinhibin, a Cysteine-, Histidine-, and Arginine-Rich Miniprotein from Abalone (*Haliotis laevigata*) Nacre, Inhibits *in vitro* Calcium Carbonate Crystallization. *Biophysical Journal*, 93(4), 1246.
4. **Heinemann, F.**, Gummich, M., Radmacher, M., Fritz, M. 2008/2009. Classification method for biomineralizing proteins according to their influence on CaCO₃ precipitation rates. *In preparation*.
5. **Heinemann, F.**, Fritz, M. 2008/2009. Amino acid analysis of the soluble organic matrix from the nacre of *Haliotis laevigata*. *In preparation*

A.9. Acknowledgements / Danksagungen

Den folgenden Personen möchte ich einen Dank aussprechen, da sie mir auf die eine oder andere Art geholfen haben diese Arbeit in den vergangenen dreieinhalb Jahren anzufertigen.

Meiner Familie, dafür mir immer alle Freiheit gelassen zu haben, dafür mir das Studium ermöglicht zu haben und für sonst alles, was man einer lieben Familie so verdankt.

Monika Fritz, dafür mir den Einstieg in die Forschung und dieses interessante, interdisziplinäre Gebiet ermöglicht zu haben und ihre einzigartige, motivierende und energetische Art.

Anna Kaufmann, die ich sehr liebe. Für unermüdliches Korrekturlesen, gutes Zureden und Aufmuntern durch ihre unglaublich fröhliche Art.

Meike Gummich, für Gele, viel Hilfe und nette Gesellschaft in Büro und Labor.

Ilona Bär, der gute Geist des Labors. **Edda Toma**, die mir zeigte wie man Kaffee nicht kochen soll.

Holger Doschke, ... dem Inschenör ist nichts zu schwör.

Laura Treccani, für gemeinsame Zeit und den Einstieg ins Thema.

Horst Diehl, für die unkomplizierte Übernahme des Zweitgutachtens.

Dieter Wolf-Gladrow, **Wolfgang Dreybrodt**, für die Verifizierung meiner Rechnungen, für Tipps und Anregungen zu den Präzipitationsversuchen.

Dietmar Blohm, für Tipps und Anregungen zu den Präzipitationsversuchen.

Malte Launspach, für Tipps und Anregungen sowie die Fortführung der Kontaktwinkelmessungen.

Auf keinen Fall vergessen möchte ich, folgenden Leuten zu danken...:

Stephan von Cölln, **Steffi Prauße**, **Marcus Prass**, **Tanja Dodenhof**, **Annika Schirmer** und **Stella Kocanis** allen für viel nette Gesellschaft und z.T. gemeinsame Arbeit, **Barbara Stoess** für Hilfe bei dem Carboanhydrase Assay, auch wenn leider - noch - nichts herauskam, **Christian Gutsche** für Hilfe bei den Strömungspotenzialmessungen, auch wenn es am Ende nicht funktionierte, **Manfred Radmacher** der immer gute Ideen hat, **Marcus Rauch** für die TEMPO oxidierten Polymerfolien, **Nancy Allison** for proofreading the document, **Anja Glisović** für XRD Messungen in Göttingen, **den Mitarbeitern der mechanischen Werkstatt** für die Anfertigung der Doppel-diffusionskammern, **Georg Grathwohl**, dafür dass ich die SEM und XRD Geräte im Institut für Keramische Werkstoffe und Bauteile benutzen durfte. **Allen anderen**, die sich vergessen fühlen (es tut mir leid, ich war wirr).